Theoretical Studies of Chiral Self-Assembly

by

Tatiana Popa

B.Sc., Universitatea Alexandru Ioan Cuza, Romania, 2006

A Dissertation Submitted in Partial Fulfillment of the

Requirements for the Degree of

DOCTOR OF PHILOSOPHY

in the Department of Chemistry

Theoretical Studies of Chiral Self-Assembly

by

Tatiana Popa

B.Sc., Universitatea Alexandru Ioan Cuza, Romania, 2006

Supervisory Committee

Dr. Irina Paci, Supervisor

(Department of Chemistry)

Dr. Alexandre Brolo, Departmental Member

(Department of Chemistry)

Dr. Dennis Hore, Departmental Member

(Department of Chemistry)

Dr. Rustom Bhiladvala, Outside Member

(Department of Mechanical Engineering)

Supervisory Committee

Dr. Irina Paci, Supervisor

(Department of Chemistry)

Dr. Alexandre Brolo, Departmental Member

(Department of Chemistry)

Dr. Dennis Hore, Departmental Member

(Department of Chemistry)

Dr. Rustom Bhiladvala, Outside Member

(Department of Mechanical Engineering)

ABSTRACT

Chiral structure formation is ubiquitous in surface self-assembly. Molecules that do not undergo chiral recognition in solution or fluid phases can do so when their configurational freedom is restricted in the two-dimensional field of a substrate. The process holds promise in the manufacture of functional materials for chiral catalysis, sensing or nonlinear optics. In this thesis, we investigate the influence of surface

attraction and geometry on adsorption-induced chiral separation in several model molecules, as well as the relationships between molecular features, specifically molecular geometry and charge distribution, and chiral recognition at surface self-assembly. Simple model molecules embody the fundamental interactions involved in supramolecular structure formation in experimental systems, and allow the in-depth investigation of key parameters.

Chiral pattern formation at the surface self-assembly is a complex problem, even in cases where very small organic molecules are considered. Even though the adsorption behaviour of small organic molecules on gold surfaces has been investigated extensively so far experimentally and theoretically, much of their chiral behaviour is yet to be understood at a molecular level. Theoretical investigations of chiral self-assembly of sulfur containing amino acids onto achiral and chiral gold surfaces is also presented in this thesis. By understanding chiral self-assembly on solid surfaces, one may control and direct it towards creating materials with desired functionality.

Contents

List of Tables

List of Figures

ACKNOWLEDGMENTS

I would like to thank:

Dr. Irina Paci, for mentoring, support, inspiration, encouragement, and patience.

Dr. Aurel Pui and Dr. Lucia Odochian, for presenting me the opportunity to come to Canada, and for their help and support towards it.

Dr. Jeffrey Paci, for help and insightful advice along the grad school years.

My family and friends, for always supporting me and believing in my abilities. Many thanks to my partner William, who shared with me the good and tough moments of the grad school and made my life always better.

University of Victoria, for funding.

The universe is asymmetric and I am persuaded that life, as it is known to us, is a direct result of the asymmetry of the universe or of its indirect consequences. The universe is asymmetric.

Louis Pasteur

DEDICATION

Dedic aceasta teza de doctorat si mai ales aceste randuri parintilor mei, care m-au sprijinit si mi-au fost mereu alaturi. Va multumesc pentru ca ati crezut in mine si pentru ca sunteti cei mai buni parinti. Mi-ati oferit tot ce ati putut pentru ca sa merg la scoala si fara ajutorul vostru nu as fi ajuns niciodata sa fiu doctor.

Multumesc, mamica si taticu!

Chapter 1

Introduction

1.1 Chirality and chiral recognition

Chirality is a molecular property of consequence in nature and life and it has held a deep fascination for scientists since its discovery in 1850s.[1] Two mirror images of a chiral molecule, frequently have identical physical and chemical properties but behave differently in interactions with other chiral molecules. Most biological molecules such as amino acids, sugars, proteins, and nucleic acids are chiral in the sense they can, in principle, exist as two enantiomers. However, nature has evolved in such a way that for common classes of compounds only one enantiomeric form exists in living organisms. Natural chiral amino acids are all found in their levo form, while most natural sugars are dextro. As a result, two enantiomers of a chiral pharmaceutical may present different biological responses within human body. While one enantiomer can have a desired effect (e.g. therapeutic), the other can be inactive, counteractive or sometimes even toxic.[2–7] An example of the latter is the tragic case of the racemic drug Thalidomide that was prescribed in the 1960's. The drug was used by pregnant

women against nausea and morning sickness. It was not known until after several thousand births of infants with malformations, that the therapeutic activity of the drug was exclusively presented by the R-thalidomide, whereas S-thalidomide was found to be teratogenic.[8, 9] Enantiomeric purity is therefore crucial in the field of pharmaceuticals and food industries.[10, 11] However, as products of synthetic chemistry, a large number of chiral drugs are still manufactured and used as racemates. To avoid the unwanted effects of a chiral drug and consequently decrease the ingested drug doses, it is very important to prepare enantiopure compounds that are the therapeutically active forms of the chiral drug. As the demand for single-enantiomer chiral compounds grows each year, so does the interest in finding and developing new enantioselective processes.

Enantioselective chemical production very often involves synthesis of a racemic mixture, followed by separation. High-performance liquid chromatography and gas chromatography, with chiral stationary phases, has been used for many years now in obtaining enantiopure compounds.[12–15] Chiral stationary phases are generally single enantiomers of a chiral compound that present different affinity for the two enantiomers of the racemic mixture to be separated. However, various stationary phases are devised for a specific class of molecules, and are rarely transferable to very different chemical compounds.[16–22]

In some cases, enantiomeric excess is achieved industrially through asymmetric synthesis. Such chemical processes require a chiral medium that drives chemical reactions to selectively produce one of the two enantiomers. Chiral surfaces may be involved in many of the enantioselective processes. For example, in enantioselective catalysis, chiral surfaces are used as catalysts to promote the production of enantioupure compounds.[23] However, there are many types of reactions that cannot yet

be catalyzed enantioselectively. In recent years, stereospecific self-assembly of chiral or prochiral molecules on achiral solid surfaces is emerging as a new twist on chiral separation, with new possible applications.

1.2 Surface self-sssembly

Molecular self-assembly on solid surfaces has been attracting increasing interest recently, both experimentally and theoretically due to the growing number of its applications in nanotechnology. Novel materials and devices with useful properties may be created using molecular self-assembly. Self-assembly is a "bottom-up" manufacturing technique, where the final nanostructure is created by starting from smaller structures (e.g. molecules) and is in contrast to a "top-down" technique, where the final structure is obtained by removing material from a larger block of matter. Molecular self-assembly is a process in which organized patterns are formed spontaneously, through non-covalent interactions. It is generally present in nature and increasingly used in chemical synthesis and nanotechnology because it involves the lowest energy consumption.

Chirality is ubiquitous on surfaces, as many molecules that are achiral in solution become chiral when bound to a surface, by participating in chiral adsorbed supramolecular structures.[24–26] Moreover, chiral molecules that do not undergo enantiospecific crystallization may form extended homochiral structures when self-assembled at a solid surface.[27–43] An underlying surface breaks the symmetry of interacting pairs of molecules, and may also alter their preferred positions and orientations. This configurational restriction often facilitates chiral recognition. Besides the more obvious implications for direct separation of enantiomers, this behavior

has applications in the molecular design of surfaces for chromatography, chiral catalysis, chiral sensing, the synthesis of nonlinear optical materials and organic chiral nanotubes.[12–14, 23–25, 31, 34, 35, 44–49] The identity of the solid surface may also influence the recognition process, through changes in molecular conformation, binding to relevant sites, changes in diffusional patterns, or simply by providing a complex periodic potential for the self-assembly process. A telling example is the formation of chiral macroscopic arrays at the adsorption of homochiral tartaric acid on Ni(111) but not on Ni(110) surfaces, where racemic arrays are formed.[29, 50] In order to gain experimental control over chiral self-assembly outcomes, a clearer understanding of the complex effects governing the formation of chiral patterns is necessary. Of particular interest is the interplay between intermolecular and molecule-substrate interactions and associated kinetic and thermodynamic effects.

Generally speaking, two types of surface-adsorbed chiral patterns have been observed experimentally. Small homochiral clusters may form at low surface coverage. In this case, molecular alignment within the cluster confers chirality and a helical direction to the self-assembled structure.[31, 33, 35, 51] Clusters comprising molecules of opposite chirality are often in mirror-image relationships themselves. At higher surface coverage, clusters pack together, or rearrange into larger domains, which often retain their enantiospecificity.[29, 32, 39, 48, 52–60] The entire surface may be homochiral if a pure enantiomer is adsorbed. When adsorption occurs from racemic mixtures, or when prochiral molecules are used, extended mirror-image domains may be observed, but the monolayer is overall racemic.

The intermolecular interactions responsible for chiral recognition in adsorbed systems are varied: hydrogen bonds and steric interactions are most prominent, but strong stereospecific effects can be engendered or aided by dipole-dipole, quadrupole-

quadrupole, as well as dispersive interactions.[27] Simple mismatches between monolayer packing geometry and the underlying lattice lead to the formation of chiral domains in monolayers of pentane on HOPG.[61] π-stacking interactions in rubrene, a molecule with planar chirality, result in a hierarchy of interdigitated structures culminating in homochiral chains and rings.[31, 62] Several types of hydrogen bonds may contribute to the formation of chiral supramolecular structures in surface-supported amino acids.[27, 29, 43] These interactions are reshaped by the mode of surface attachment, particularly when this attachment occurs through chemical or strongly dispersive physical bonds.

Significant progress has been made in recent years in understanding the fundamental aspects of self-assembly[52, 63] in bulk supramolecular and block copolymer systems [64], as well as surface-bound molecules [65], yet much work is still to be done. By understanding the complex effects governing chiral pattern formation and the interplay between molecule-molecule and molecule-substrate interactions, one may learn to predict and control chiral self-assembly on solid surfaces and direct it towards achieving chiral segregation and towards creating materials with desired functionality.

1.3 Adsorption of cysteine on gold

Cysteine is a natural proteinogenic amino acid with a mercapto group and its adsorption on gold surfaces has been studied extensively. Besides its strong binding with gold through thiol group, the cysteine molecule is a good model for chiral adsorption. Despite several thorough experimental and theoretical investigations of the chiral self-assembly of cysteine on gold surfaces, pattern formation at the adsorption of cysteine on gold is still not well understood.

It is generally unclear if upon adsorption of various mercaptans on different gold facets, the thiol group is preserved or the S-H bond is broken with the hydrogen either adsorbing on gold or desorbing as molecular hydrogen. [38, 66] In order to break the strong S-H bond, the second thiol molecule in the vicinity of the same adsorption site on gold surface is likely needed. [67] Coverage and substrate temperature were found to play an important role in binding mechanism. [35, 43, 68, 69] In many cases, thiolates and/or thyils were seen to coexist on the surface with intact thiols. At intermediate coverage, it was found that cysteine adsorbs on gold surfaces (Au(111) [69], Au(17 11 9) [70], Au(110) [38, 71, 72]) through both thiol and amino functional groups, with S-Au bonding being few times stronger than N-Au bonding.

The adsorption modes of cysteine on the surface depend on its molecular state. Cysteine can adsorb either neutral, in zwitterionic form or in a mixture of both. Neutral cysteine is believed to form adsorption patterns with hydrogen-bonded carboxylic groups and adsorb to the surface through sulfur and nitrogen. Electrostatic interactions between NH_3^+ and COO^- predominate in adsorbed zwitterionic species, and thus the binding of cysteine to the substrate through amino group may or may not be replaced by $COO^- - Au$ interactions. On gold nanoparticles, zwitterionic cysteine preferentially adsorbed in a double layer conformation.[73, 74] The inner layer bound covalently to the gold through sulfur atom as thiolate, whereas the outer thiol layer interacted with the chemisorbed layer through hydrogen bonding. Furthermore, in a double layer adsorption model the interaction between inner layer and Au_{55} nanoparticle was found to be stronger than in the monolayer case.[73]

X-ray photoelectron spectroscopy studies show that at 300K L-cysteine adsorbs on chiral Cu(531) with a four-point footprint : through sulfur, nitrogen and two oxygen atoms. The fact that both oxygen atoms within the carboxylate group bind

very similarly to the surface is explained by the authors as a result of -OH group losing the hydrogen atom, which is presumed to stay on the surface at 300K. Upon adsorption onto reconstructed Au(110)-(1x2), molecules of cysteine physisorb at low temperatures and form unordered structures that self-assemble upon annealing to 270K into monodisperse clusters. The transition from physisorption to chemisorption is believed to happen at room temperature, and upon further annealing to 340-380K, ordered chemisorbed cysteine clusters are formed. Thermal activation was needed for cysteine to become covalently bound to Au(111), which indicates a distinct difference from alkanethiols, that readily form covalent thiolate-gold bond.[43]

Methionine is a sulfur-containing amino acid related to cysteine, which has a methyl thiol group replacing the thiol (-SH) group, and a second methylene group in its chain. A rather weak S-Au interaction was found upon adsorption of methionine on Au(111) at room temperature, allowing the molecules to easily rearrange and then completely desorb around 365K.[36] Adsorption studies of L -methionine on Cu(531) suggest that sulfur atom within the L-methionine is not bound to the surface and the molecules adsorb through only two oxygen and a nitrogen atom.[75]

We also considered in some of our studies, the non-proteinogenic amino acids, homocysteine, that is biosynthesized from methionine by elimination of the terminal methyl group of the latter. Homocysteine is associated with a variety of diseases, including cardiovascular disease and blood vessel blockage and is involved in metabolism of proteins containing cysteine and methionine.[76] In contrast with copious research on adsorption of cysteine on gold surfaces , homocysteine and methionine adsorption has received a limited experimental and theoretical attention.

The surface binding modes of these amino acids depend on many factors including the identity of the facet on which adsorption occurs, molecular state of the adsor-

bate, coverage density and temperature of the system. Several Density Functional Theory studies exist about adsorption of single or at the most a couple of thiol and thyil molecules, including cysteine, on gold surfaces.[67, 69, 77-81] Only few studies, however, have been performed on extended systems. Classical methods as Molecular Dynamics (MD) or Monte Carlo simulations are more suitable for investigation of larger systems. Adsorption of few single amino acids, peptides and proteins on gold surfaces was investigated using MD simulations. It was concluded that adsorption of peptides on gold is enhanced by the high conformational flexibility of the peptide, as well as by enriching the peptide in amino acids that present high affinity for gold. [82–84] Understanding the adsorption and behaviour of individual amino acids may help in designing peptides with higher affinity for the substrate as well as in creating stable self-assembled monolayers.

1.4 Naturally chiral surfaces

Broadly speaking, there are two types of chiral surfaces: those that are modified by chiral templating and those that are naturally chiral. Chiral templated surfaces are formed upon adsorption of chiral or prochiral organic ligands on achiral solid surfaces. The chirality of these substrates is transmitted from the chirality of the template and is gone when the template is removed. Naturally chiral surfaces, on the other hand, are crystalline materials that exhibit intrinsic chirality. Such surfaces present chiral atomic structures and are obtained by truncation of the bulk material at a particular facet.

The face-centered cubic bulk structure of many metals is highly symmetric. The achiral bulk structures, however, exhibit planes whose normals do not lie in one of the

bulk symmetry planes. By truncating the bulk structure along these planes, surfaces with no mirror symmetry may be created. Furthermore, all Miller index surfaces of face-centered cubic (fcc) structures with Miller indices satisfying the criteria $h \neq k \neq l$ and $h \times k \times l \neq 0$ are chiral.[85, 86] Naturally chiral surfaces are characterized by atomically flat terraces separated by kinked steps.[87, 88] An example of a chiral surface is shown in Figure1.1.

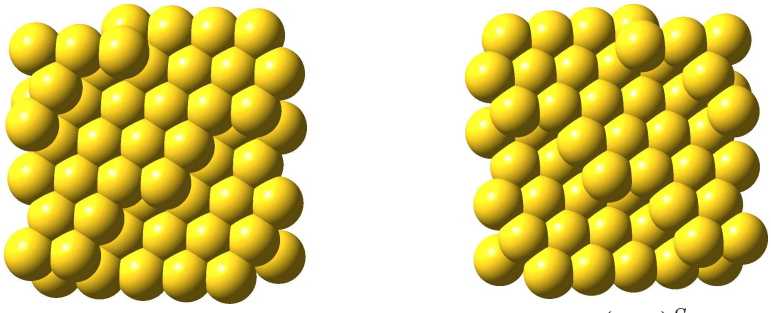

Figure 1.1: The ideal structure of chiral fcc (643) surface. These two surfaces are mirror images of one another and cannot be superimposed.

The origin of chirality on the surface comes from the structural feature of the kink site. The kinks are formed by intersection of low Miller index (100), (110) and (111) microfacets, and their handedness is dictated by the sense of rotation among these three microfacets. Depending on whether the atomic density of facets is decreasing in clockwise sense of rotation around the kink from (111)→ (100)→(110) or counterclockwise, the surface is labeled R or S, respectively. [86, 89–91]

The real structures of chiral surfaces typically deviates from those of ideal Miller index surfaces (as is the (643) surface shown in Figure 1.1) due to thermally induced surface roughening.[92] Experimental studies show that in real structures the atoms diffuse along the steps with rising the temperature, inducing the conjoint of the kinks, which lose their periodicity and are rather randomly distributed. However,

simulations and STM images show that naturally chiral surfaces that have undergone thermal roughening overall maintain their net chirality.[85, 93–95]

Naturally chiral surfaces may be also formed by chiral imprinting of achiral surfaces. Unlike chiral templating, chiral imprinting leads to formation of chiral surfaces and the chirality will persist even when the imprinting agent is eliminated. A telling example is the adsorption of l-lysine on Cu(100), which induced the restructure of the surface with formation of homochiral $(3\ 1\ 17)^R$ facets with kink sites, the structures that have never been seen on clean Cu (100).[96]

Based on a number of different experimental and theoretical methods, there are evidences that naturally chiral metal surfaces exhibit enantiospecific surface chemistry.[89–91, 94, 97–102] To understand the enantioselectivity, however, is challenging and requires besides the chiral surface and a chiral adsorbate, some measurements that are sensitive to the enantiospecificity of their interaction.[44]

Several experiments have been performed on adsorption of chiral molecules on a naturally chiral surfaces. The desorption of R- and S- propylene oxide (a simple chiral molecule with one chiral center) from the chiral Cu(643) surface was investigated by Horvath et al. using Temperature-Programmed Desorption (TPD).[90, 103] For this particular molecule and for many others adsorbed on chiral surfaces it was observed that the molecules are first desorbed from terraces, then from steps and lastly from the kinks. The molecules adsorbed on the kink site gained binding energy from the surface atoms forming the step in addition to the binding energy due to terrace atoms, making the kinks the most attractive sites on the surface. Furthermore, kink sites were preferred for binding because of the presence of low coordinated surface atoms. It was observed that the two enantiomers desorb from the chiral surface at different temperatures. S-propylene oxide (S-PO) desorbs from $\mathrm{Cu}(643)^R$ at a

temperature approximately 1 K lower than R-propylene oxide and 1 K higher when adsorbed on Cu(643)^S than its enantiomer. These results were the first to show enantiospecificity upon desorption of chiral molecules. Similar experiments pointed out an enantiospecific desorption energy difference for chiral (R)-3-methylcyclohexanone (R-3MCHO) which was adsorbed on various chiral surfaces such as Cu(531)$^{R\&S}$, [104] and Cu(643)$^{R\&S}$.[90]

A theoretical study of adsorption of chiral molecules on Cu(874)^S surface was done by Bhatia et al. using Density Functional Theory (DFT) calculations.[105] Propylene oxide presented weak enantiospecificity (roughly 0.02 eV enantiomeric shift) upon adsorption on Cu(874)^S, whereas amino-(fluoro)methoxy species showed a relatively stronger enantiospecific interaction with the chiral surface (0.13 eV enantiomeric shift). It is, however, unclear without experimental data whether these energy differences are meaningful in the context of DFT errors. Binding energies and configuration of chiral hydrocarbons adsorbed on chiral Pt(532), Pt(643) and Pt(754) surfaces were calculated by Sholl et al. using Monte Carlo simulations.[106] Except for 1,3-dimethylallene, the enantiomeric shift exceed the shifts detectable in experiments. [107]

An interesting example is the adsorption of (R)-3-methylcyclohexanone (R-3-MCHO) on the achiral Cu(221) and Cu(533) which resulted in the formation of the kinks in the naturally straight step edges. Exposure of the two stepped Cu surfaces to R-3-MCHO at two different temperatures (90 K and 330 K) was followed by desorption at two different temperatures. Comparing with TPD spectra of R-3-MCHO from Cu(643), the lower desorption temperature corresponds to desorption from straight step edges and the higher one being in the range of desorption from kink sites observed on chiral Cu surface.[91] The adsorption temperature is thus an important

factor in chiral adsorption and may induce the formation of the kinks on initially flat surfaces.

1.5 Force field

Molecular self-assembly is governed by inter- and intra-molecular forces that drive the molecules into a stable, lowest energy state. These forces include hydrogen bonding, electrostatic interactions, hydrophobic interactions, and van der Waals forces. Theoretical methods have an important role in describing non-covalent interaction and their influence on particular chemical systems. Experimentally, it is often challenging to separate the interaction of interest from unexpected secondary interactions or solvent effects. Using computational studies, highly adjustable prototype systems featuring a particular interaction can be directly investigated, excluding some or all of the competing interactions or solvation effects. However, finding a suitable theoretical method to describe a system of interest may be quite challenging. Quantum-level theoretical approaches are generally desired, although they are limited to small-sized systems. As the size of the chemical system of interest increases, quantum mechanical first principle methods, as well as semi empirical methods become computationally expensive. As a result, numerous molecular mechanic force fields have been developed and widely used in computational simulation of extended systems.

A force field (FF) is a mathematical function plus associated parameters used to describe the potential energy of a system of particles. It includes a bonded term that refers to the atoms or groups that are linked by covalent bonds, and a nonbonded term that describes a long range intermolecular van der Waals and Coulomb interactions. In a FF approach a molecule is a collection of spherical atoms connected by springs.

Bonded energy arises from changes in molecular structures that is reflected in bond length, angles and torsions.

The basic functional form of a force field is given as follows:

$$E_{total} = E_{bond} + E_{angle} + E_{torsion} + E_{electrostatic} + E_{van\ der\ Waals} \tag{1.1}$$

Force fields parameters are derived by fitting to experimental data or are computed from ab initio methods.[108–116] The bonded energy, as mentioned above, arises from the deviations from the ideal structure of a molecule. The equilibrium values for bonds and angles are usually taken from X-ray data. Their corresponding force constants are derived by fitting to experimental vibrational frequency data. Dihedral parameters are computed from ab initio methods, by scanning over a range of angles, optimizing the geometry at each step and calculate the change in potential energy. Non bonded interaction parameters are usually derived by combining experimental data (whenever available) with calculations.

Atomistic potentials become computationally expensive with increasing the size of the system investigated. A simplification of a molecular description with fewer interaction sites can be done using a coarse graining process, in which several atoms are mapped together and can be treated as a single "grain". The coarse grained (or united atom) force fields that were developed so far are shown to perform well, expanding the utility of existing computational resources. Nevertheless, the resolution and accuracy of these models are reduced comparing to all-atom approaches.

The adsorption of molecules on metallic surface has not yet been widely approached in literature. Only a few force fields are available to describe the interaction between a metallic substrate and an organic adsorbate. GolP (Gold-Protein)

is an atomistic force field used to describe interaction of proteins with Au(111) surfaces in water.[114] It was derived by Iori et al. by combining experimental data with calculations. A unique feature of GolP is the presence of virtual sites (VS) on the Au(111) surface to direct the adsorption on the top of a Au atom, rather than above a hollow or bridge surface site. Accordingly, for each real gold atom on the Au(111) surface two virtual sites (VS) that occupy the hollow site were introduced. The Lenard-Jones parameters for VS and bulk Au atoms were considered to be similar, and calculated from experimental adsorption energy data of linear alkanes and ab initio MP2 calculations of model systems.

Another force field that was recently designed to describe the interaction of proteins with Au(111) and Au(100) surfaces is GolP-CHARMM.[83] The force field was parametrized using a combination of experimental and first- principles data. The same virtual site geometry used previously in GolP, with virtual sites located in the hollow sites of the surface, has been adopted here for both Au(111) and Au(100) surfaces. The FF parameters were not transferable between the two interfaces due to differences in their surface structure and thus different density of virtual sites.

Both GolP and GolP-CHARMM force fields describe the adsorption of proteins onto gold under aqueous conditions and are not transferable to non-aqueous interfaces. If the interaction for each original gold atom at the Au(111) surface was replaced with two virtual sites, then the surfaces has more atoms that have to be considered in the simulation. An atomistic description of the solid is generally considered with the potential obtained as a sum of atomistic potential. As a result, using such FFs involves an additional computational cost. Atomistic (and coarse grained) force fields are based on numerous approximations, and their use has to be treated with consideration. To determine the transferability of the force fields mentioned

above, a limited set of molecules different from that used for parametrization was tested. A larger number of tested molecules is however desired, and thus many of the force fields are subjected to continuing testing, reparametrization and refinement.

1.6 What this thesis sets out to do

A complex set of factors cooperate to yield the final adsorption pattern in chiral self-assembly. An understanding of the individual effects of these factors could enable us to learn and control the self-assembly process and direct it towards obtaining desired patterns and/or chiral separation on a solid surface. In this thesis, chiral self-assembly of several chiral and prochiral systems was investigated. A number of simple model molecules were initially used to understand relationships among molecular structure, intermolecular interactions, geometric and energetic makeup of the underlying substrate, and the extent of two-dimensional chiral separation. Although not directly related to any real life molecules, the models incorporated in an elementary fashion the fundamental interactions that lead to chiral self-assembly in experimental systems.

Furthermore, we explored the pattern formation and chiral discrimination in relevant experimental systems like adsorption of cysteine on gold surfaces. Chiral amino acids are relatively simple prototypes of chiral self-assembly that have been studied considerably, both theoretically and experimentally. Sulfur containing amino acids are in particular interesting because of their strong binding to the gold surfaces, that promotes the formation of stable self-assembled monolayers which could be used in surface binding of peptides and proteins.

Cysteine is the only proteinogenic amino acid with a mercapto group and its

adsorption behaviour and pattern formation on achiral flat Au(111) and on stepped chiral Au(643) surfaces was computationally investigated in this thesis. Homocysteine and methionine amino acids were also considered. Homocysteine is a homologue of cysteine that has an additional methylene group and its behaviour upon adsorption on Au(111) surface was investigated. Methionine is the second sulfur containing proteinogenic amino acid that is, however, missing the thiol group. Its structure is similar to homocysteine, with the difference that there is additional methyl terminal group attached to the sulfur. Amino acids have both a basic amino group and a carboxylic acid group. A proton can be internally transferred from $COOH$ to NH_2 leading to the formation of the zwitterionic structure that has negative COO^- and positive NH_3^+ parts with no overall electric charge. Zwitterions of cysteine, homocysteine and methionine and their adsorption behaviour on gold surfaces were also considered in our studies.

Chapter 2

Methodology

2.1 Parallel Tempering Monte Carlo methodology

Several modern methods in computer simulations overcome trapping in metastable configurations. Parallel Tempering Monte Carlo (PTMC) [117–121] is one such method, in which configurational exchanges between copies of the system that evolve at different temperatures are used to overcome quasiergodicity on complex potential energy surfaces (PESs).[122–128] Replicas of the system are simultaneously equilibrated at different temperatures, using canonical (constant number of particles, volume and temperature) Monte Carlo moves. Ergodicity is sought by periodically performing configurational swaps between replicas with neighboring temperatures.

Simulations consist of a Markov chain of the following types of moves:

(i) Standard MC translational moves, based on the standard Metropolis acceptance criterion [122, 129, 130]: for the canonical ensemble,

$$acc(o \rightarrow n) = \min\{1, \exp[-\beta(U(n) - U(o))]\} \ , \tag{2.1}$$

where $acc(o \rightarrow n)$ indicates the acceptance probability of a move from o to n, U is the total potential energy, n and o denote the "new" and "old" configurations, respectively, and $\beta = 1/k_B T$ is the inverse temperature.

At equilibrium, the average number of accepted moves that leave the old configuration must be equal to the average number of moves returning the system into the "old" configuration. Thus, the probability of going from the "old" state to the "new" state must be such that it does not destroy an equilibrium once it is reached. In this manner, the MC scheme obeys the condition of detailed balance. Another important property of acceptance probabilities is ergodicity, which indicates that any point in configurational space can be reached in a finite number of MC steps from any other points.[122]

A MC displacement move (e.g. translational step) is generally selected by trial and error. The maximum allowed displacement affects the acceptance rate: small MC move steps provide better acceptance rate but a smaller region of the phase space is being sampled, whereas large steps lead to low acceptance rates and increase effort in sampling the configurational space. Thus the steps must be chosen as large as possible while maintaining a reasonable acceptance rate. An acceptance rate of approximately 50% is often desirable for a Monte Carlo simulation, there is, however, no theoretical basis for using this or any other particular acceptance rate.

(ii) Swap moves: two differing-temperature replicas of the system, i and $j = i+1$, are randomly selected, and their configurations are swapped, with the acceptance probability given by:

$$acc(o \rightarrow n) = \min\{1, \exp[\Delta\beta\Delta U]\} \ , \tag{2.2}$$

where $\Delta\beta = \beta_i - \beta_j$ is the difference between the two neighboring inverse temperatures for which configurations are being swapped, and $\Delta U = U(x_i) - U(x_j)$ is the difference in energy between the two configurations.

Using this methodology, replicas evolving at high temperatures are able to sample regions of the potential energy surface that cannot be easily achieved directly at low temperatures. Through configurational exchanges, these regions are made available to lower temperature replicas, as well. As a result, a replica that may have been trapped in a local minimum can be brought out via a configurational exchange. In addition, successive configurations sampled by one replica may become less correlated, and thus each replica may achieve its equilibrium configuration much faster than without configuration swaps.[125] This convergence speed-up usually offsets the overhead due to the necessity of simulating multiple copies.

The temperature range for parallel tempering is selected so that the minimum temperature corresponds to a compact assembly of the molecules (solid phase), while the highest temperature allows overcoming most energy barriers. To determine the temperature spacing between neighboring replicas and the number of replicas, trial runs are performed initially for each new system being investigated. Energy histograms are calculated for each temperature. A sketch of an energy histogram is shown in Figure 2.1. The acceptance probability of replica swaps is predicted by the amount of overlap between two neighboring histograms. The larger the overlap, the more exchange attempts will be accepted. However, if the temperatures are very close to each other, higher temperatures might not be very different from the lower temperatures, and as a result besides inefficient use of computational resourses, the low temperature of interest might not gain much from the attempted exchanges. The interval between neighbouring temperatures is generally different along the range of

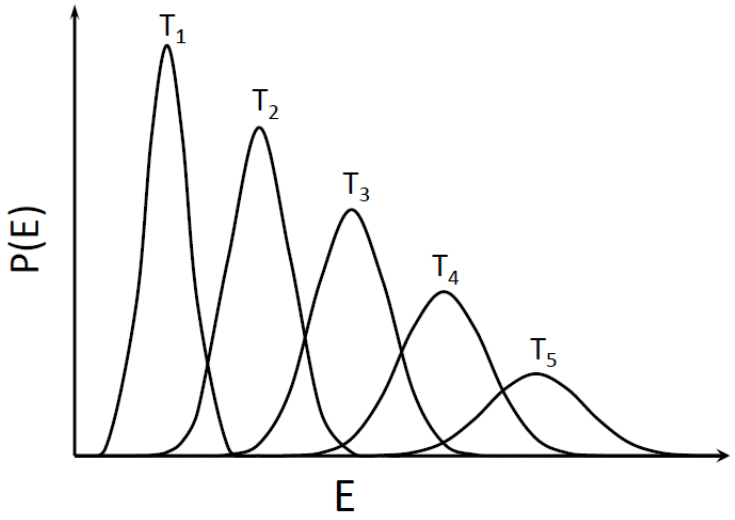

Figure 2.1: A sketch of an energy histogram considering a range of temperatures ($T_1 < T_2 < \cdots < T_5$). P(E) represents the probability of the system to be described by a particular energy E at the temperature of interest.

temperatures. Kofke showed that a geometric progression of temperatures (T_i/T_{i+1} = constant) results in equal acceptance ratios across the temperature range.[131, 132] As a rule, high temperatures are spaced more widely than are the low temperatures.

Several studies have been done on finding the optimal number of replicas and the acceptance probability, respectively, for an efficient Parallel Tempering sampling. The general belief is that high acceptance probabilities imply a high mixing efficiency.[133, 134] Rathore et al. [135], however, found that once the high and low temperatures are decided, an uniform swap acceptance ratio of 20% yielded the best performance of parallel tempering simulations. For the case of their system, adding more replicas failed to increase the performance of the simulation. A quite similar optimal value of 23% acceptance rate was found by Kone and Kofke. [132] Predescu et al. [133, 134] indicated that for an efficient parallel tempering sampling the acceptance probabilities could lie anywhere between 7% and 82%, though there is always an

associated computational cost. The authors found that optimal acceptance probability that ensures the highest efficiency, which involves the highest number of effective swaps per unit of computational cost was 38.74%. In our simulations a minimum 10% acceptance of exchange attempts was enforced.

In two dimensional calculations of rigid toy model molecules a third type of move was added to the Markov chain:

(iii) Swaps between the positions of pairs of non-identical molecules (enantiomers). These molecular swaps were attempted, overall, in about $(100/N)\%$ of the moves (where N is the number of molecules in the sample), and accepted according to their Boltzmann factors.

In the case of flexible molecules besides translational moves, the molecules were allowed to rotate around all three axis. Moves that determined changes in molecular structure, and consequently deformed the molecule were also considered.

2.2 Interaction potentials

Total potential energy of the system is described in the equation 2.3 as a sum of intramolecular and intermolecular potentials. The energy associated with changes in molecular structure is given by the changes of bond lengths, angles and torsions. The nonbonded energy term relates to the atoms that are not linked by covalent bonds and describes the overall interaction between particles of the system.

$$U_{total} = \sum_{bonds} U_{stretch} + \sum_{angles} U_{bend} + \sum_{dihedrals} U_{torsion} + \sum_{pairs} U_{nonbonded} \,, \tag{2.3}$$

The bond stretching term between two covalently bonded atoms i and j is described by a harmonic potential :

$$U_{stretch} = k_{ij}^{r} \left(r_{ij} - r_0\right)^2 \tag{2.4}$$

where k_{ij}^{r} and r_0 are harmonic force constant and equilibrium bond length, respectively. In our study, however, bond length were held fixed.

Similarly, the bond angle vibration between three atoms i, j and k within a molecule is described by a harmonic potential on the angle θ_{ijk} :

$$U_{bend} = k_{ijk}^{\theta} \left(\theta_{ijk} - \theta_{ijk}^{0}\right)^2 \tag{2.5}$$

where atom i and k are both bound to atom j, θ is the angle between the two bonds (see Figure 2.2), k_{ijk}^{θ} is the harmonic force constant and θ_{ijk}^{0} is the equilibrium bond angle.

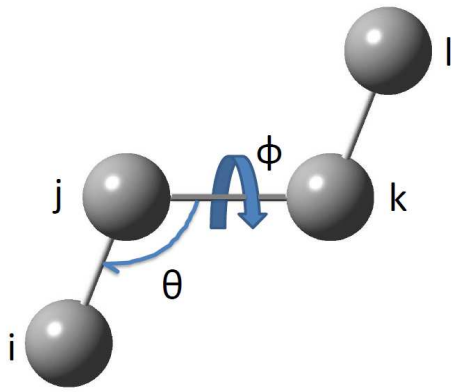

Figure 2.2: Changes in molecular structure (described by any atom i, j, k and l) associated with changes in bending (θ) and dihedral (ϕ) angles.

The torsional potential was expanded as a fifth-order power series of $\cos\phi_{ijkl}$:

$$U_{tors} = \sum_{n=0}^{5} C_n(\cos\phi_{ijkl})^n \ , \tag{2.6}$$

where ϕ_{ijkl} is the dihedral angle between the planes ijk and jkl and C_n are expansion coefficients for the power series.

Intermolecular nonbonded interactions were described with pairwise atom-based Lennard-Jones and Coulombic potentials:

$$U^{ab}_{nonbonded} = \sum_{i,j=1}^{n_{at}} \left[4\epsilon_{ij} \left(\left(\frac{\sigma_{ij}}{r_{ij}} \right)^{12} - \left(\frac{\sigma_{ij}}{r_{ij}} \right)^{6} \right) + \frac{q_i q_j e^2}{4\pi\epsilon_0 r_{ij}} \right] \ , \tag{2.7}$$

where a and b denote two interacting molecules, n_{at} is the number of atoms in a molecule, ϵ_{ij} and σ_{ij} are the Lennard-Jones depth and distance parameters for atoms i and j, r_{ij} is the distance between the centers of the two atoms, q_i is the partial charge on atom i, e is the electronic charge and ϵ_0 is the dielectric constant of vacuum. Mixed Lennard-Jones parameters were obtained using the Lorentz-Berthelot mixing rules: $\sigma_{ij} = (\sigma_{ii} + \sigma_{jj})/2$, $\epsilon_{ij} = \sqrt{\epsilon_{ii}\epsilon_{jj}}$.

The OPLS (Optimized Potentials for Liquid Simulations) force field was used to describe the intermolecular and intramolecular interaction of the amino acids. This was a valid choice in our gas phase calculations because it was found that there are insignificant differences between the internal energies in the gas and liquid phases calculated using OPLS parameters.[109, 136] Partial charges not available in the force fields were calculated using a B3LYP/6-311++G(d,p) methodology in Gaussian09,[137] with the CHELPG (CHarges from ELectrostatic Potentials using a Grid based method) flag.[138]

Lennard-Jones parameters for the interaction of cysteine and gold were derived by Chapman et al. and are shown in Table 2.1.[139]

Table 2.1: Lennard-Jones parameters for cysteine-gold interaction.

Pair	σ(Å)	ϵ(kJ/mol)
S−Au [1]	2.38	38.286
N−Au	3.09	4.760
C−Au	3.17	0.270
O−Au	3.02	0.202
H−Au	2.74	0.173

[1] An energy parameter of ϵ_{S-Au}=19.1 was used to describe the interaction of uncleaved SH groups to gold atoms

2.3 Reduced units

Dimensionless variables, or reduced units, are generally used in computer simulations. The reason behind using reduced units is that an infinite number of combinations of temperature, particle diameter, energy, charge, etc. corresponds to the same state in reduced units. In other words, the results obtained for a set of reduced units are valid for infinitely many systems due to the law of corresponding states.

Another practical reason is that typically in a simulation run of a relatively large system, quantities like the total energy associated with interaction of many particles are computed. Using absolute numerical values may result in a very large or very small computed numbers which can create an arithmetic overflow or underflow, respectively. Also, calculation errors could be found much easier when working with reduced units. [122]

Throughout this thesis, the units are reduced with respect to Lennard Jones parameters of the first atom in the molecule, σ_{11} and ϵ_{11} as follows:

$$
\begin{aligned}
\epsilon^*_{ab} &= \frac{\epsilon_{ab}}{\epsilon_{11}} \; ; \\
\sigma^*_{ab} &= \frac{\sigma_{ab}}{\sigma_{11}} \; ; \\
U^*_{ab} &= \frac{U_{ab}}{\epsilon_{11}} \; ; \\
q^* &= q\sqrt{\frac{1}{(4\pi\epsilon_0\epsilon_{11}\sigma_{11})}} \; ; \\
T^* &= \frac{k_B T}{\epsilon_{11}} \; ,
\end{aligned}
\tag{2.8}
$$

where q is a fraction of electronic charge and ϵ_0 is the dielectric constant of vacuum.

Simulation results obtained in reduced units can always be converted back to real units.

2.4 Designing Naturally Chiral Surfaces

Chiral surfaces have attracted a growing interest because of their enantioselective surface chemistry. Chiral surfaces may be created by adsorbing chiral or prochiral organic molecules on a solid surface, as well as by exposing surfaces of metallic materials that have chiral atomic structure. In the latter case, the surfaces are called naturally chiral, since they exhibit intrinsic chirality. Such surfaces generally retain their chirality at temperatures higher than 1000 K and consequently may be preferred for enantioselective chemical processes over organically templated chiral surfaces.[88] Several studies have been performed on adsorption of chiral molecules on naturally chiral surfaces. Not every chiral compound, however, showed a significant enantiomeric energy shift. In this thesis, we are trying to gain some insight into enantioselective

adsorption mechanism on naturally chiral surfaces at a molecular level.

Experimentally, naturally chiral surfaces are produced by cutting off the face-centered cubic (fcc) bulk structure along distinct Miller indices. We constructed our surfaces in the same manner. First step was to design a relatively large cube, where the atoms are arranged in face-centered cubic (fcc) geometry both on the faces and in bulk, Figure 2.3 (a).

To obtain a surface with (h k l) projection, the cube was then cut along h, k and l Miller indices resulting the structure shown in Figure 2.3 (b).

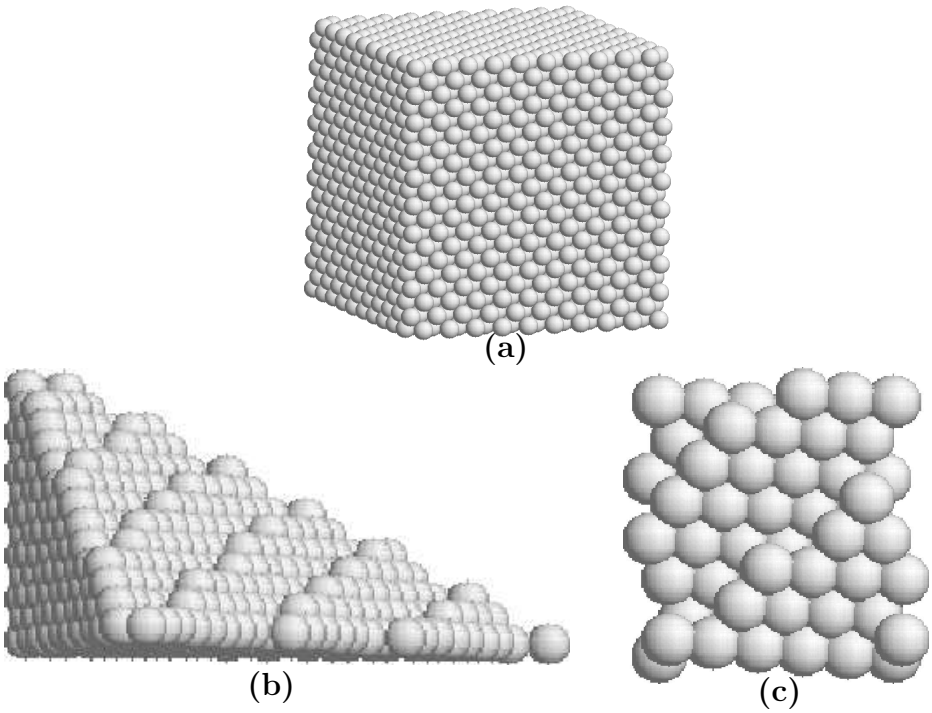

Figure 2.3: The initial cube with the face-centered cubic geometry (a), which was cut along the Miller indices (b) and then edged to obtain the final surface (c) that can be used in a simulation box. The images are scaled up from (a) to (c).

A plane can be defined through three non-colinear points. Given three points N_1 (x_1, y_1, z_1), N_2 (x_2, y_2, z_2) and N_3 (x_3, y_3, z_3) the equation of the plane through these

points is:

$$Ax + By + Cz + D = 0, \tag{2.9}$$

where

$$A = \begin{vmatrix} 1 & y_1 & z_1 \\ 1 & y_2 & z_2 \\ 1 & y_3 & z_3 \end{vmatrix} \quad B = \begin{vmatrix} x_1 & 1 & z_1 \\ x_2 & 1 & z_2 \\ x_3 & 1 & z_3 \end{vmatrix} \quad C = \begin{vmatrix} x_1 & y_1 & 1 \\ x_2 & y_2 & 1 \\ x_3 & y_3 & 1 \end{vmatrix} \quad D = - \begin{vmatrix} x_1 & y_1 & z_1 \\ x_2 & y_2 & z_2 \\ x_3 & y_3 & z_3 \end{vmatrix} \tag{2.10}$$

Consider three non-colinear points in the (h k l) plane N_1 (a/h, 0, 0), N_2 (0, a/k, 0), and N_3 (0, 0, a/l), a being the edge length of the cube. After calculating and then replacing A, B, C and D determinants in the equation of the plane 2.9, we obtain :

$$hx + ky + lz = a, \tag{2.11}$$

Another way of defining the (h k l) plane is by specifying a point and a normal vector to that plane. If N_0 (x_0, y_0, z_0) is a point in the plane then any point N (x, y, z) will be in the same plane only if the vector from N_0 to N is perpendicular to the normal vector n. The equation of the plane that contains the two points appears as follows:

$$n_x(x - x_0) + n_y(y - y_0) + n_z(z - z_o) = 0, \tag{2.12}$$

The vector normal to the (h k l) plane in a cubic lattice has the [h k l] direction. Consequently, the normal vector projections on x, y, and z axis are h,k and l, respectively, and the equation of the (h k l) plane becomes:

$$h(x - x_0) + k(y - y_0) + l(z - z_o) = 0, \tag{2.13}$$

Considering N_0 to have the coordinates (a/h, 0, 0) with a the edge length of the cube, the plane equation becomes identical to equation 2.11. Therefore, any point that belongs to the (hkl) plane must satisfy the equation 2.11.

The cube was then cut along the plane described by the equation 2.11 and every atom that belongs to that plane and all underneath it, have been kept and all the above ones were removed. The remaining part of the cube in order to make it suitable for use in simulation by changing the sloping geometry to a relatively horizontal level, was rotated around z and x axes with angles θ and ϕ, respectively:

$$\theta = \arctan\left(\frac{h}{k}\right), \quad \phi = \arctan\left(\frac{h}{l \cdot \sin(\arctan\left(\frac{h}{k}\right))}\right), \tag{2.14}$$

The last steps was to cut the surface in a square shape (similar to the shape of the bottom of the simulation box) and remove all the layers underneath that were not to be used in the simulation.

Chapter 3

Surface effects in Chiral Self-Assembly

The work presented in this Chapter has been published in Chemical Physics Letters 507 (2011) 128.

In this chapter, Parallel Tempering Monte Carlo (PTMC) simulations are used to investigate the effects of the surface potential in chiral adsorption. The geometric make-up of the surface as well as the strength of the molecule-surface interactions, have a profound impact on the patterns resulting from the self-assembly process in simple Lennard-Jones atoms.[140] However, systematic studies of such effects in more complex molecular systems are yet to be performed, and are expected to be influenced by a broad array of variables, from surface complexity and reorganization, to molecular structure and interaction, or the physical or chemical nature of the adsorption process.[27, 141, 142] In a first attempt to a systematic investigation of surface effects, we focus here on two model chiral systems, with one and two chiral centers. These molecules have been shown [143] to form homochiral micelles at low temperatures

when restricted to evolve in two dimensions, even though three dimensional assembly of the same racemate led to heterochiral structures. Here, we evaluated the surface effects on physisorbed patterns and phase behavior by considering an atomistic, rigid, underlying surfaces of varying geometries, atom sizes and interaction parameters. An apolar substrate can impact structure formation in the self-assembled monolayer through: (i) The effect of the interaction field provided by the surface. This can change either through the strength of atom-based pairwise attractions or through the density (or number) of surface atoms considered in the simulation box; (ii) The geometric detail or roughness of the substrate. Surface atoms can act as "sites", locally, for cluster formation or impact the order in the monolayer through geometrical fit or commensuration, or lack thereof. These effects are considered independently and are discussed in Sections 3.2, 3.3 and 3.5. Section3.4 describes the phase behaviour of the systems that were investigated.

3.1 Computational details

3.1.1 Simulation details

We used a Parallel Tempering Monte Carlo (PTMC) methodology, described in Chapter 2. Depending on the complexity of the molecule, 24 or 32 replicas were used, evolving at different reduced temperatures, ranging from 0.7 to 6.5 or 8.0 (the definition of reduced temperatures is given in Section 2.3). In the production runs, a total of 3×10^9 single molecule or configurational MC steps were carried out for each system. Additional moves were performed as necessary, to ensure convergence of the total energy for each replica. 5% of attempted moves were temperature swaps. Molecular swaps were attempted, overall, in about $(100/N)\%$ of the moves (where N

is the number of molecules in the sample). Molecules were restrained to move within a plane. Specifically, molecules were allowed to translate within the plane and rotate fully around the normal to the plane (z) axis. Rotations around the x and y axes were restricted to a maximum of 30°, to prevent the molecules from flipping onto the opposite face (a move which would transform one enantiomer into another for molecules with two-dimensional chirality). This restriction would often occur naturally in an experimental setting, due to molecules having a preferential orientation on the surface, such as a strong physisorption group, a chemisorption group or a lone pair group.

The racemic mixtures considered here were composed of 200 rigid molecules, in a simulation box of size 54×54×8 in reduced units. No periodic boundary conditions (PBCs) were used in simulations reported in this chapter. PBCs were used in surface-free test runs, however, and found to have no effect on structure or chirality measures at the low densities considered here. Higher density configurations would certainly be impacted by the presence or absence of PBCs, through imposition of long-range structure inherent to PBC implementation in the first case, or through edge effects and differential binding at box edges, in the latter. Evaporative events (particles leaving the simulation box) were forbidden, by simply rejecting moves that lead to evaporation.

3.1.2 Models

Model molecules. We present in Figure 3.1(a) a sketch of one of the enantiomers for each of the two models considered here. Molecular geometries, indicated by Cartesian atomic coordinates, and the corresponding charges and Lennard-Jones parameters are presented in Table 3.1. With these parameters, a reduced temperature T^*=2

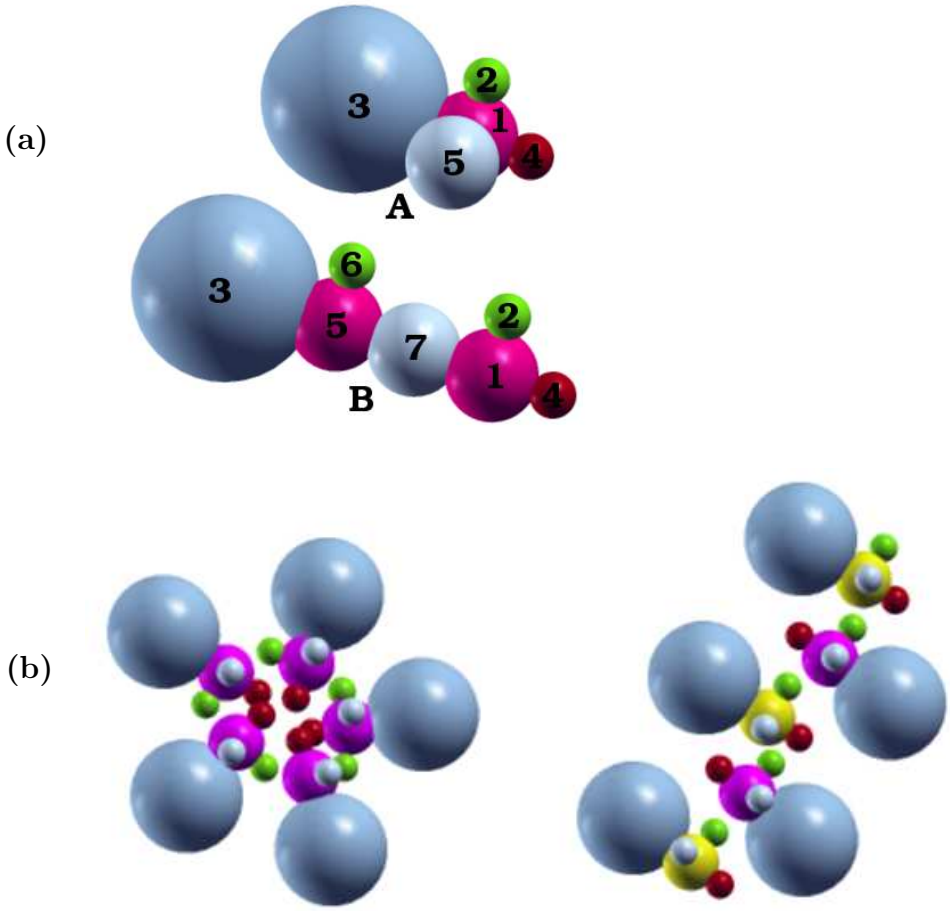

Figure 3.1: (a) Chiral molecules investigated. The numbering of atoms is the same as in Table 3.1. Each atom is not necessarily representative of a C, N, O, H, or another actual group, but rather of a particular Lennard-Jones interacting species. The chiral atoms are indicated in magenta, for consistency with the following figures. Atom 1 is chiral in molecule A. In molecule B, atoms 1 and 5 exhibit chirality when adsorbed on the surface. Atoms colored in magenta and green also carry partial charges. (b) Local homochiral and heterochiral structures for model A. Structures are local detail from snapshots of simulations of 200-molecule racemic mixtures on (111) surfaces. Central atoms in the two enantiomers are indicated in yellow and magenta, respectively. For the clarity of the image, the fifth atom is shown smaller than in reality and the surface atoms have been obscured.

corresponds to 241 K. In Table 3.1, the partial charges are given as fractions of a full electronic charge.

In molecule A, the chiral atom (atom 1) and spacer group (atom 2) have partial charges. Steric asymmetry is created by a large group (atom 3) which we will call "head", and a small strongly attractive group (atom 4) hereafter called "tail". The out-of-plane atom 5 ensures that the molecule is chiral in three dimensions, as well as in two dimensions. The planar part of the molecule somewhat resembles nitronaphthalene (NN) geometrically, although the intention in designing the molecule was to include elementary interactions generally responsible for discrimination (such as dipolar and steric interactions), rather than to simulate any particular real-life molecule. Interactions between molecules of type B are more complex. The molecule has four partially charged atoms, as well as a headgroup and a tailgroup. Atoms 1 and 5 are chiral when molecule B is adsorbed on a surface, and their chirality is maintained throughout the simulation due to the rotational restriction described above.

At low and intermediate temperatures in the intermediate coverage regime used here, self-assembled structures tended to be either homochiral rosettes or heterochiral double chains, as shown in Figure 3.1(b) for model A. Replicas at higher temperatures equilibrated to a gas phase, where monomers or dimers were dispersed throughout the simulation box. The rosette-type micellar structures formed on the surface resembled those obtained experimentally for NN [24] or rubrene [31].

Micellar assembly was driven by the asymmetry of the Lennard-Jones component of the intermolecular potential. The small attractive tailgroups gathered in the center of the cluster, while the bulky, less attractive headgroups were pushed to the exterior of the micelle. On the other hand, Lennard-Jones interactions alone did not lead to chiral separation. Alignment within the micelles, and thus chiral recognition,

Table 3.1: Physical characteristics of the racemic systems investigated here.

Molecule	n_{at}[1]	i	Position (x^*, y^*, z^*)	q_i	σ^*_{ii}	ϵ^*_{ii}
A	5	1	(0,0,0)	0.35	1.0	1.0
		2	(0.53,0,0)	-0.35	0.5	1.0
		3	(0,1.05,0)	0	2.0	1.5
		4	(0,-0.53,0)	0	0.5	3.0
		5	(0,0,0.7)	0	1.0	0.5
B	7	1	(0,0,0)	0.35	1.0	1.0
		2	(0.55,0,0)	-0.35	0.5	0.7
		3	(0,2.15,0)	0	2.0	0.25
		4	(0,-0.55,0)	0	0.5	3.0
		5	(0,1.4,0)	0.35	1.0	1.0
		6	(-0.55,1.4,0)	-0.35	0.5	0.7
		7	(0,0.7,0)	0	1.0	0.25

[1] n_{at} indicates the number of atoms in a molecule. For each atom, the positions in the molecular reference system (x^*, y^*, z^*), reduced with respect to σ_{11}, partial atomic charges q_i, and reduced Lennard-Jones distance σ_{ii} and strength ϵ_{ii} parameters are included.

was induced by the additional electrostatic component of the potential.[143] Alignment of dipoles within the micelles conferred helicity to the molecular cluster, and the resulting structures were themselves chiral. On the other hand, dipoles were not fully aligned in micellar structures, and this was particularly problematic in the B molecules, which have four partially charged groups to satisfy. In this case, the attractive interactions between tailgroups were often overcome by the necessity of dipole alignment, and double chain structures predominated in low temperature structures.

Surface models. Two projections of the face-centered cubic unit were used to build the underlying surface: the (100) projection (denoted in the following pages as the square projection) and the (111) (hexagonal) projection. Interactions between the atoms in the molecules and those of the surface were of the Lennard-Jones type. Surfaces with σ_s=1,2 and 4 and ϵ_s=0.5, 1 and 2 were considered, where σ_s and ϵ_s are

the surface parameters used in the LB formulas to determine mixed terms. As we were mainly interested in planar structures, the chiral atom was treated as a stronger-binding group: ϵ^*_{1s}=4. The surface was considered rigid, thus interactions between surface atoms were neglected in the calculations.

3.1.3 Chiral segregation measures

Chiral resolution can be estimated visually from the snapshots included below. To quantify the extent of chiral separation, we calculated average fractions of molecules that have exclusively like and exclusively unlike nearest-neighbors, denoted below by F_l and F_u, respectively, and defined in detail elsewhere [143]. Briefly, for each molecule in the mixture, two nearest neighbors are found, provided they are within a separation that corresponds to the first minimum in the pair distribution function of the molecular geometric centers. The geometric center of the molecule was defined as the point with coordinates $x = \sum_{atoms} x_i$, $y = \sum_{atoms} y_i$ and $z = \sum_{atoms} z_i$. F_l and F_u provide a measure of the proportion of molecules involved in homochiral clusters, without contamination from nearby clusters which may be formed of mirror-image molecules.

3.2 The effect of surface attraction field

The effect of the pairwise interaction strength was considered by varying ϵ_s. F_l and F_u for square surfaces with small atoms and different interaction strengths are shown in Figure 3.2. It can be seen from the figure that the effect of the pairwise surface attraction is minimal, with more attractive surfaces exhibiting a slightly poorer quality of resolution. This was confirmed by analysis of a large number of snapshots, in which

double chain structures were seen to occur rarely, but more often in the surfaces with larger ϵ_s.

One major difference brought by the surface attraction strength was the speed of convergence of the small temperature energies. Systems with large ϵ_s took much longer times to equilibrate than those with weakly attractive surfaces. This is due to trapping in very stable local minima on the highly attractive surface, and is certainly related to the experimental interplay between diffusion and adsorption strengths in self-assembled monolayers.[28] In that vein, one question that arises is whether the drive and ability of PTMC to search for global minima on complicated potential energy surfaces undermines its ability to predict experimental adsorbed structures, which are often metastable states of the respective system.

Decreasing σ_s or changing the surface geometry from square to hexagonal also had the effect of increasing the overall surface attraction, as the density of surface atoms increased in both cases. For example, in a simulation box with a lateral size of 54×54 reduced units, there were 2628 surface atoms with σ_s=1, or 162 atoms with σ_s=4 for square pattern surfaces, and 3348 atoms with σ_s=1 when the surface was hexagonal. Low temperature snapshots of adsorbed racemates of A on hexagonal surfaces with different interaction strength, are shown in Figure 3.3. The temperature dependence of the F_l and F_u on the surface attraction is also included. We found minimal changes in the quality of the separation when the surface geometry was changed from square to hexagonal. Given the small effects of varying ϵ_s, we propose that differences in F_l with surface atom size were due to geometry, rather than energetics.

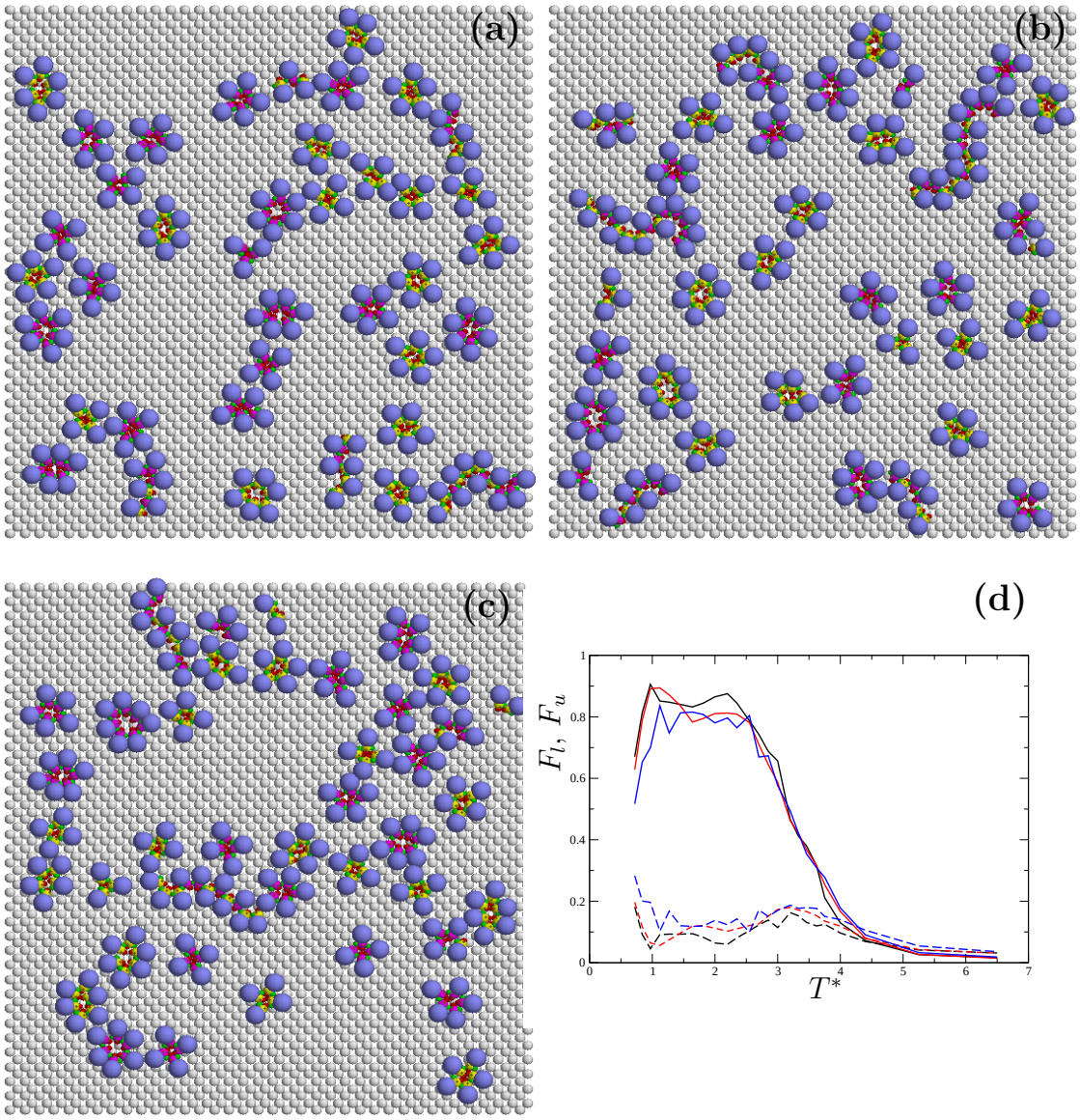

Figure 3.2: Effect of the surface attraction on condensed phase structures and chiral resolution. Simulation snapshots are shown for molecule A at T*=1.45, on a square surface with σ_s=1.0 and ϵ_s=0.5 (a), 1.0 (b), 2.0 (c). Panel (d) shows the temperature dependence of F_l (solid lines) and F_u (dashed lines). Black (dark), red and blue (light) lines represent ϵ=0.5, 1.0 and 2.0, respectively. The solid lines overlap each other as do the dashes - the impact of ϵ_s on F_l and F_u is negligible.

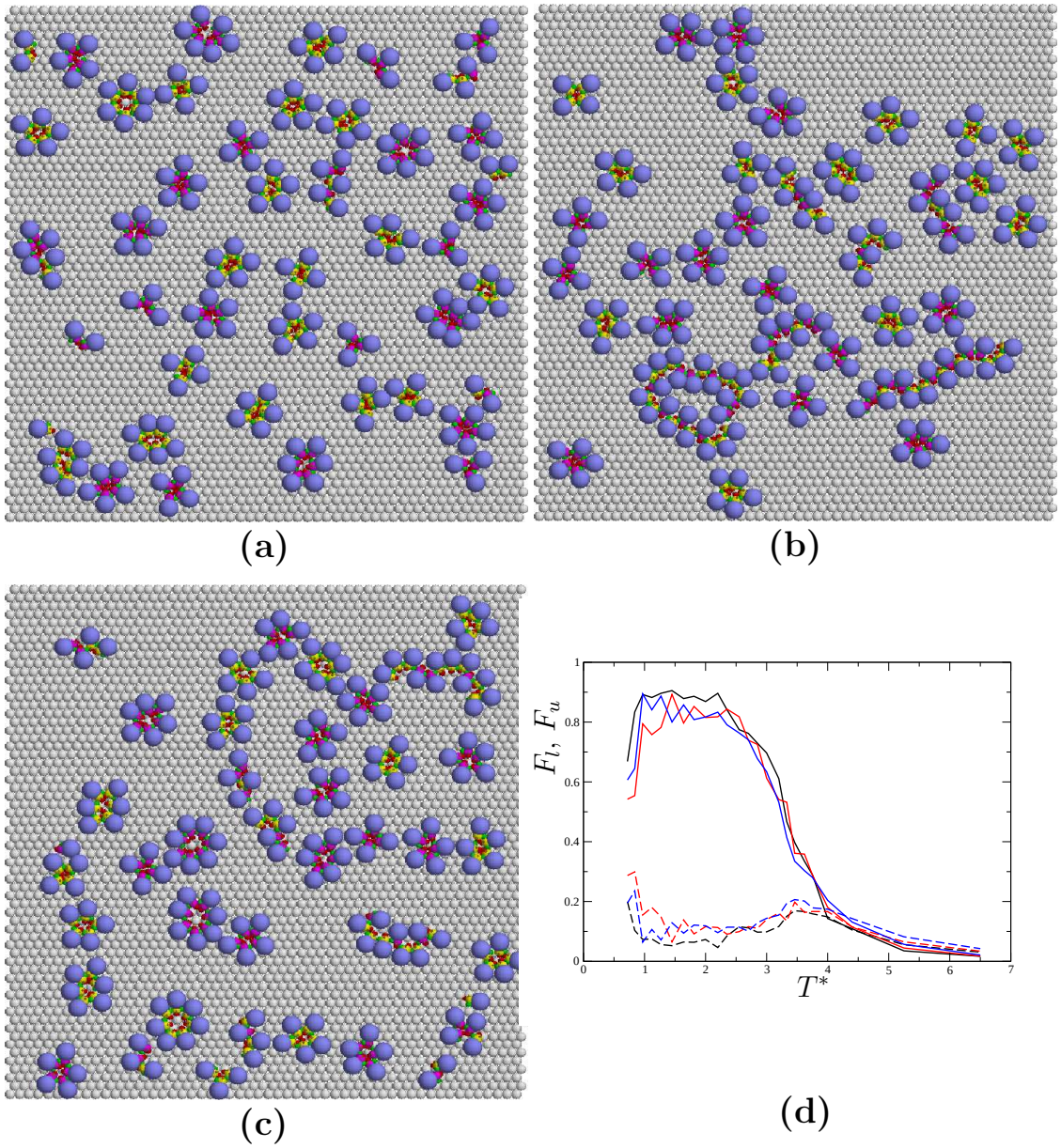

Figure 3.3: Effect of the surface attraction on condensed phase structures and chiral resolution. Simulation snapshots are shown for molecule A at T*=1.45, on a hexagonal surface with σ_s=1.0 and ϵ_s=0.5 (a), 1.0 (b), 2.0 (c). Panel (d) shows the temperature dependence of F_l (solid lines) and F_u (dashed lines). Black (dark), red and blue (light) lines represent ϵ=0.5, 1.0 and 2.0, respectively. The solid lines overlap each other as do the dashes - the impact of ϵ_s on F_l and F_u is negligible.

3.3 The effects of surface geometry

A few low-temperature snapshots of adsorbed racemates of A on square surfaces with different atomic sizes, are shown in Figure 3.4. The dependence of F_l on the surface atom size is also included in the figure. While the atomic size of the underlying surface did not significantly perturb the predominant formation of homochiral micelles at condensation, it impacted the symmetry and island size in the resulting pattern in several ways.

First, a more rugged surface (due to bulkier atoms) led to better separation in the monolayer. As shown in Figure 3.4(d), the fraction of molecules with exclusively like neighbors was over 95% at low temperatures, for systems with large and intermediate surface atoms. The separation achieved on small-atom surfaces was about 85%, which is in the range found in our surface-free calculations. This supports the argument that the enhancement on surfaces with large atoms is due to the surface geometry, and not its overall attraction. Examination of snapshots (see Figures 3.4(a)-(c) for example) revealed the presence of some chain structures and no obvious commensuration with the surface in the small-atom case.

Two particular effects can be observed in Figure 3.4 for intermediate and large surface atoms: When the size of the surface atoms was equal to that of the bulky headgroup of the adsorbate, there was a certain amount of commensuration of the latter with the substrate's fcc geometry. Finally, when the surface atoms were larger, the entire rosette structure appeared to commensurate with the substrate. A mixture of two adsorbed geometries is seen for the rosette clusters in Figure 3.4(c) and other snapshots not included here: In one geometry, the highly attractive tailgroups at the center of a rosette were all in contact with a single surface atom, the rosette formed

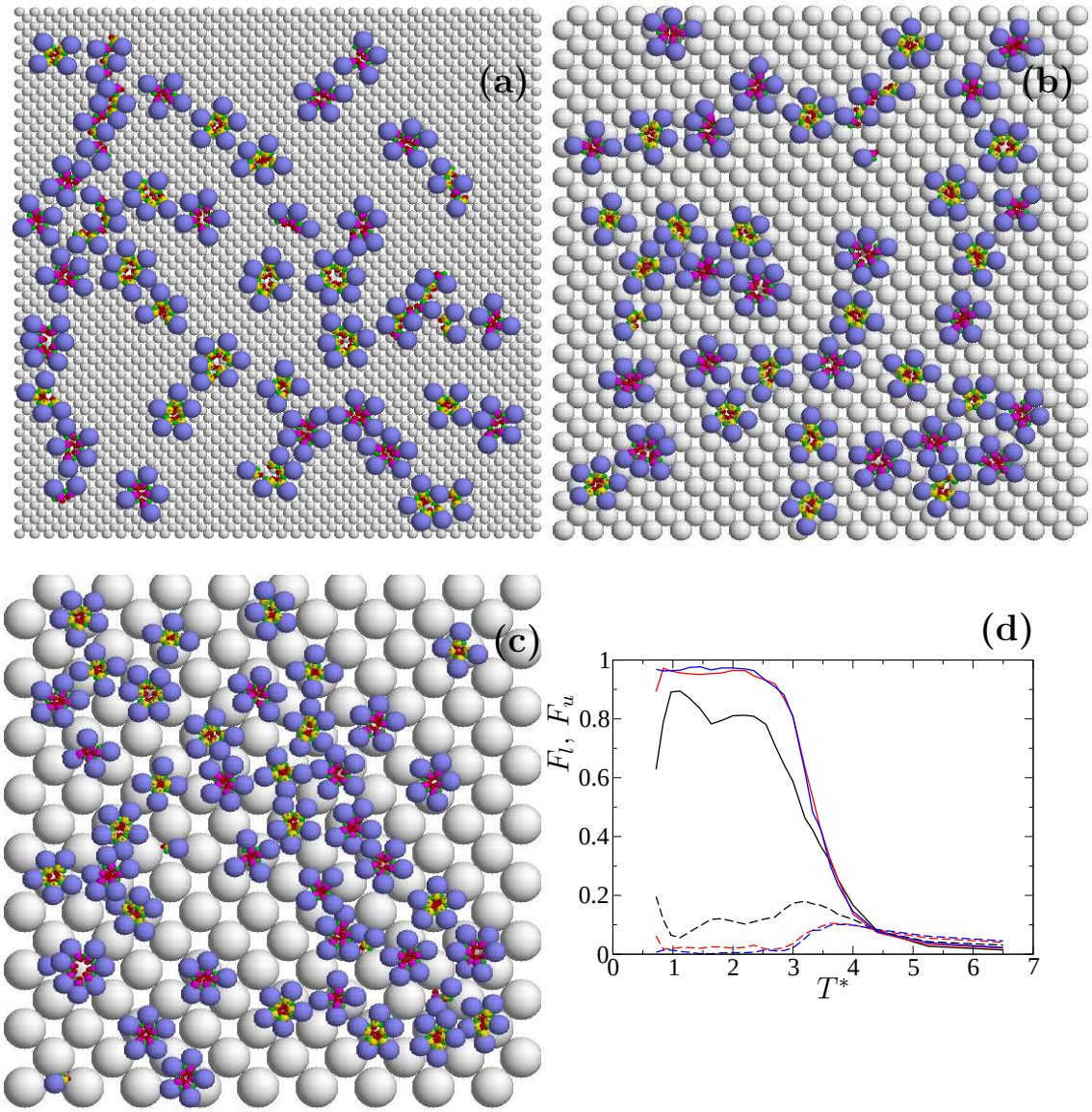

Figure 3.4: Effect of the surface atom size on condensed phase structures and chiral resolution. Simulation snapshots are shown for molecule A at T*=2.2, on a square surface with ϵ_s=1.0 and σ_s=1.0 (a), 2.0 (b), 4.0 (c). Panel (d) shows the temperature dependence of F_l (solid lines) and F_u (dashed lines). Black (dark), red and blue (light) lines represent σ=1.0, 2.0 and 4.0, respectively. The light (red and blue) lines coincide.

directly atop the respective atom and had a circular structure. In the other geometry, the highly attractive tailgroups were found grouped together in bridge or off-bridge positions. In this case, the rosette was slightly distorted towards an elliptical geometry by the necessity of fitting in the grooves between surface atoms.

These geometric effects impacted the size distribution of the rosette clusters. We calculated average numbers of k-molecule clusters, where k was considered between 3 and 10. We report these averages for k=3 to 6 in Table 3.2. It can be seen from

Table 3.2: The size of clusters formed on surface with square and hexagonal geometry at T^*=1.64 and 2.35.

Surface geometry	ϵ_s	σ_s	T^*	N_{tot}	N_3	N_4	N_5	N_6
square	0.5	1.0	1.64	37.4	5.4	9.3	15.4	6.5
		2.0		38.9	0.8	6.9	24.3	6.4
		4.0		39.9	1.2	5.1	27.2	5.3
square	1.0	1.0	1.64	37.9	7.9	10.0	15.2	3.6
		2.0		39.6	1.5	7.6	25.0	5.5
		4.0		38.7	2.1	2.5	25.8	8.0
square	2.0	1.0	1.64	36.8	5.5	8.3	15.4	5.8
		2.0		39.1	3.4	10.0	20.4	5.1
		4.0		38.8	1.7	6.1	22.2	8.4
square	1.0	1.0	2.35	37.4	5.9	8.7	16.2	5.5
		2.0		39.9	1.7	8.1	24.6	5.3
		4.0		39.8	2.2	5.9	22.6	8.4
hexagonal	1.0	1.0	1.64	37.1	6.2	7.8	16.8	4.5
		2.0		39.5	2.8	8.0	22.2	5.4
		4.0		39.6	1.5	7.4	25.4	5.1

the table that the low-temperature increase in separation quality (as measured by F_l) with surface roughness was accompanied by an increase of the prevalent size of the self-assembled rosettes. For an example, about 47% of clusters were small (3 or 4 atoms) when σ_s=1 at T*=1.64 and ϵ_s=1, and only about 12% were small when σ_s changed to 4. There was also a small increase in the total number of homochiral

clusters formed as σ_s increased, as chain structures disappeared.

Calculations performed on hexagonal surfaces revealed similar effects of the surface geometry and attraction on the pattern formation in the monolayer as those discussed above for square surfaces. However, examination of snapshots revealed a decrease in the quality of the commensuration for intermediate surface atoms (see Figure 3.5(b), for example). The hexagonal surface was more compact than a square surface, and the rosette cluster did not fit well either with the commensuration of the headgroups at σ_s=2, or with the rosette commensuration at σ_s=4. This was reflected by a larger proportion of small clusters than in the square surface case, and in slightly lower values of F_l at low temperatures (see Figure 3.5 and Table 3.2). In other respects however, trends in resolution quality with hexagonal surface atom sizes, closely followed those discussed for square surfaces.

3.4 Phase behaviour

When cooling the system from a desorbed gas phase to the condensed, on-surface phase, two specific transitions are possible: the adsorption and the condensation transitions. For simple Lennard-Jones atoms, these have been either convoluted or clearly separable, as a function of the relative pair potentials acting in the system.[140]

The temperature dependence of the total potential energy for racemates equilibrating nearby several types of square surfaces is shown in Figure 3.6. The smooth change in energy across the phase transition temperature range is due to the limited size of the system. A single inflection point was found in each of the graphs, which indicates that the adsorption and condensation phase changes occurred concomitantly in these systems. We examined a large number of configuration snapshots in the

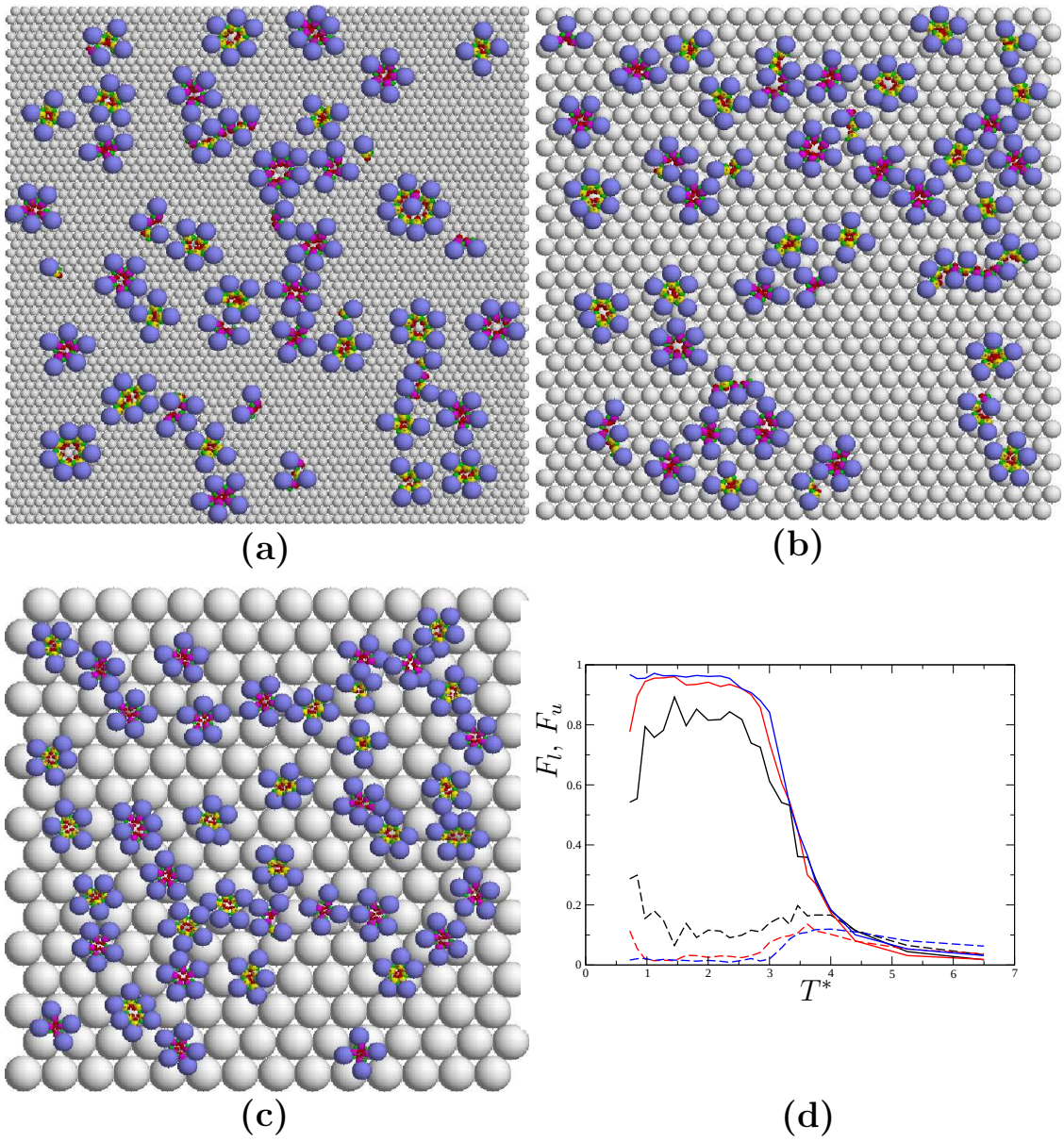

Figure 3.5: Effect of the surface atom size on condensed phase structures and chiral resolution. Simulation snapshots are shown for molecule A at T*=1.64, on a hexagonal surface with ϵ_s=1.0 and σ_s=1.0 (a), 2.0 (b), 4.0 (c). Panel (d) shows the temperature dependence of F_l (solid lines) and F_u (dashed lines). Black (dark), red and blue (light) lines represent σ=1.0, 2.0 and 4.0, respectively. The light (red and blue) lines coincide.

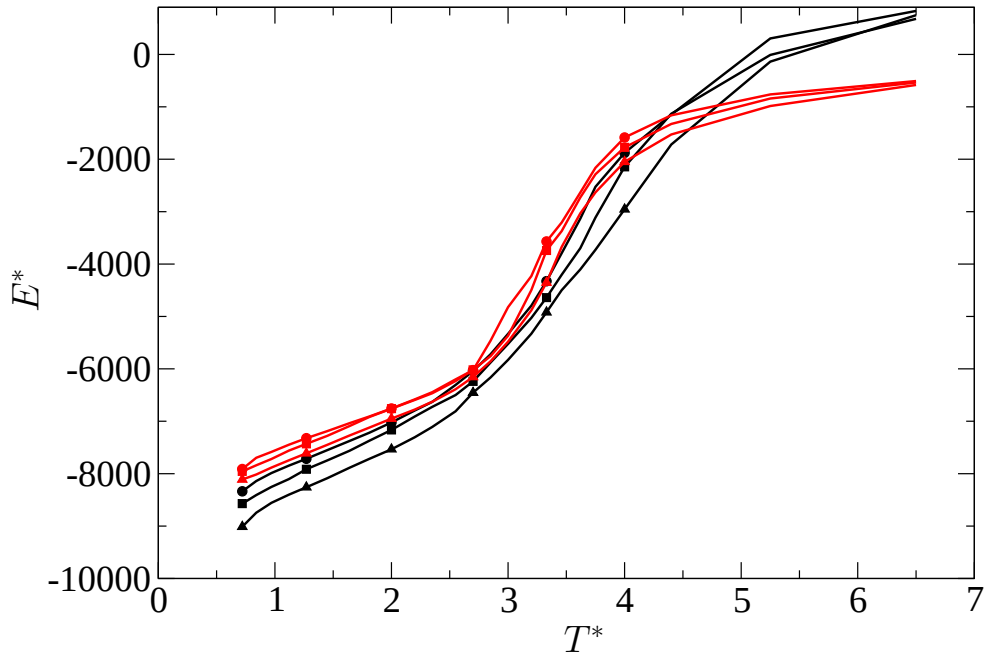

Figure 3.6: Temperature dependence of the total potential energy for racemic mixtures of A adsorbed on square surfaces. Curves are given for σ_s=1.0 (black/dark) and σ_s=4.0 (red/light) and ϵ_s=0.5 (circles), 1.0 (squares) and 2.0 (triangles).

transition region. A simulation snapshot of molecules A at T*=3.46 is presented in Figure 3.7. In all cases, including the example shown in the Figure, condensed phase homochiral clusters were seen to coexist at high temperatures with desorbed single molecules. Snapshots also indicated that chiral recognition occurred in the adsorbed state, as all gas phase molecules were found in monomer or (rarely) dimer structures. This is consistent with convergence to zero of the F_l and F_u plots in Figures 3.2-3.5(d) at high temperatures. Not unexpectedly, complete desorption/dissociation was facilitated by surfaces that were overall less attractive.

On the other hand, even in the condensed phase, an increase in temperature favored structures with higher entropy. As shown in Table 3.2 and Figures 3.2-3.5, at temperatures below the phase change interval, an increase in temperature led to

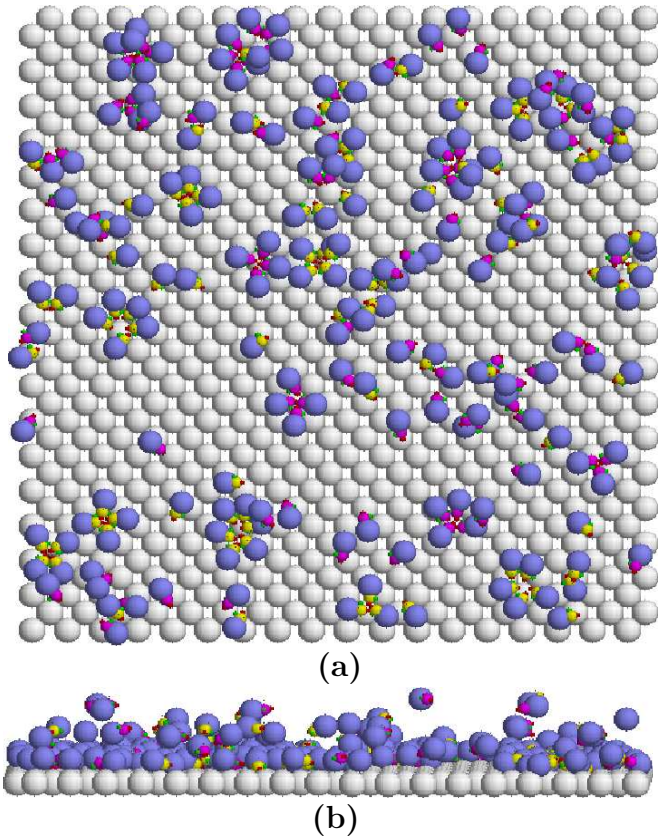

Figure 3.7: Phase transition region. Simulation snapshots are shown for molecule A at T*=3.46, on a square surface with σ_s=2.0 and ϵ_s=1.0. Top (a) and side (b) views are presented. The condensed phase homochiral clusters are seen to coexist with desorbed single molecules.

larger average numbers of clusters, and an increased ratio of small to large clusters.

3.5 Molecules with two chiral centers

In a surface-free study,[143] molecules of type B were seen to achieve mixed condensed phase structures with some enantiomeric excess, as a result of a complex interplay of intermolecular interactions, multi-body effects and configurational entropy. During the simulation, there was an alternation of configurations where structures were

largely heterochiral double chains, configurations where many of the molecules were involved in homochiral circular structures, and configurations where most molecules were involved in extended aggregates where locally homochiral structures of opposite chirality alternated within the same aggregate.

When a surface was included explicitly, the same types of structures were found (see for example Figure 3.8). However, as in the case of model A racemates, the fit between the geometry of the substrate and that of the condensed phase aggregates led to some differentiation between the different types of configurations mentioned above. A surface with small atoms had little impact on the quality of the resolution racemates of molecule B (Figure 3.8(a)). However, analysis of this and other snapshots does illustrate a strong degree of integration of the headgroup in the surface pit sites. This led to periodic structures, either in the usual extended double-chain configuration, or in somewhat distorted homochiral local structures. The substrate lattice modified the periodicity of the double-chain structures. In snapshots such as that presented in Figure 3.8(a), intermolecular distances in the double-chain structures decrease on average by 9% from the surface-free case. Regardless, F_l and F_u were relatively unchanged at low temperatures from the constrained two-dimensional values.

Similar monolayer behavior was observed on intermediate ($\sigma_s = 2$) surfaces for this model system, however the adlayer was more relaxed in this case. Throughout the temperature domain, monolayer structures resembled the surface-free case the most when $\sigma_s = 2$. When the surface atoms were larger again ($\sigma_s = 4$), commensuration of the condensed structures with the underlying surface was observed. Tail-groups clustered together in the pit sites of the square surface, leading to extended micellar structures. However, in this case the surface was more weakly attractive overall, and overlapping structures were observed (see Figure 3.8(b)). This led to

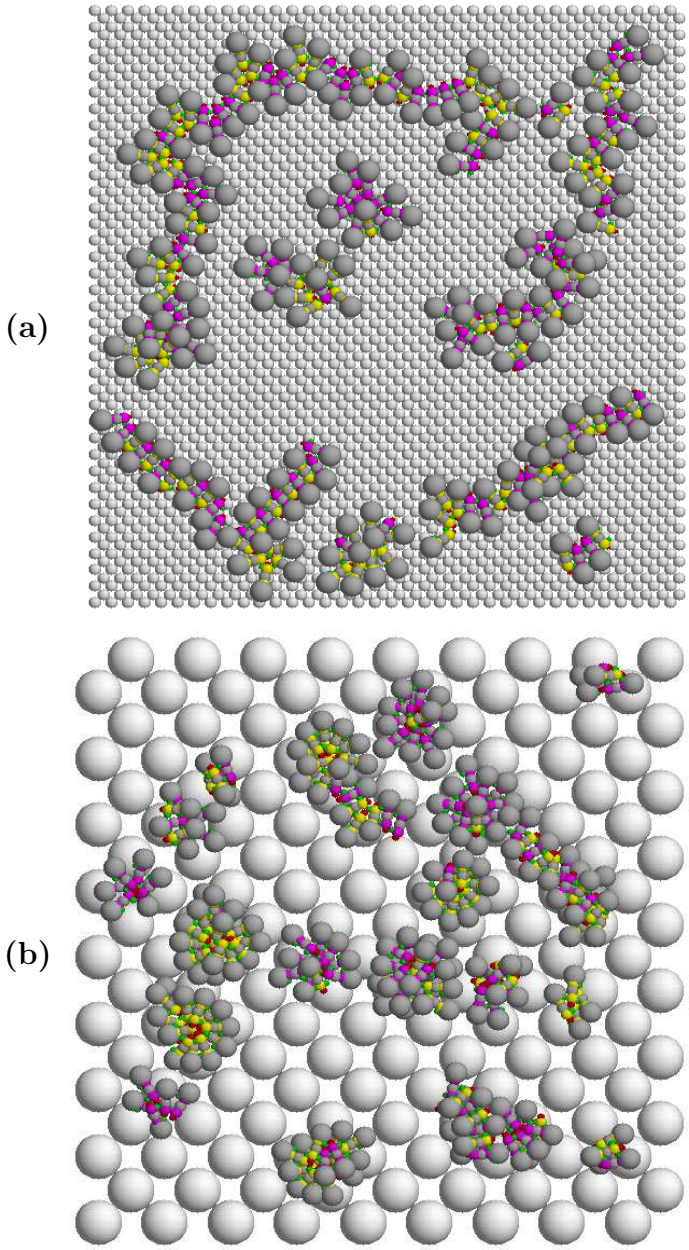

Figure 3.8: The impact of surface geometry on condensed phase structure in a 200 molecule racemate of molecule B. Structures are given for T*=2.6, ϵ_s=1 and σ_s=1 (panel (a)) and 4 (panel (b)).

some loss of specificity in the separation, as three-dimensional micelles are not necessarily homochiral.[143] The overall result of these competing effects was that the quality of resolution increased on these large-atom surfaces to F_l=0.5 at intermediate temperatures, from F_l=0.3 on surfaces with $\sigma_s \leq 2$.

3.6 Summary

We studied the effects of the potential and geometry of an underlying rigid surface on chiral structure formation at adsorption using Parallel Tempering Monte Carlo method. Two model molecules with distinct chiral self-assembly behavior in two-dimensional condensation were considered. For both models, the impact of the substrate attraction and symmetry on the extent of chiral resolution or micelle characteristics was small. On the other hand, the lattice constant (or atom size) of the underlying surface was found to influence significantly the outcome of the chiral self-assembly process, particularly for the more complex molecules considered here, which exhibited small local chiral excess in surface-free calculations. This geometric effect occurred through commensuration, either with the bulky molecular headgroup, or with the micellar rosettes that form in the self-assembly process.

The phase behavior of the systems we studied revealed a single, broad phase transition in which adsorption and two-dimensional condensation overlapped. The degree of overlap depended somewhat on the strength of the surface-substrate interactions, however, in all cases, condensation occurred in the adsorbed phase.

Chapter 4

Designing enantioselectivity in chiral self-assembly: a theoretical study of competing interactions

The work presented in this Chapter has been reproduced from Ref.[144] with permission from The Royal Society of Chemistry

In this Chapter, we investigate computationally how molecular structure and intermolecular interactions affect the surface self-assembly outcomes in model molecules. In previous investigations, the molecules exhibited limited chiral recognition, but emerged as a case study in the effects of molecular features, polymorphism and the complexity of interactions in extended systems, on chiral organization in condensed phases. By modifying the electrostatic and steric make-up of the molecules presented here, we altered the balance of various effects and interactions, to gain an understanding of how they can be leveraged to attain the desired assembly outcome. To restrict

the parameter space and focus specifically on the effect of substituents and the balance of intermolecular interactions, we ignore the atomistic makeup of the underlying surface and restrict the racemic mixtures to evolve in two dimensions. Despite the simplicity of the models employed here, the structural features obtained in condensed phases resemble closely those obtained experimentally in chiral self-assembly on solid surfaces.

In homochiral self-assembly, enantioselectivity is achieved through preferential interactions between molecules of the same chirality, compounded, in the case of surface self-assembly, by surface effects. The nonbonding interactions involved in the process can be of several types, but chiral recognition effects are always manifested at short range.[145] The reasons are twofold: on one hand, supramolecular interactions are often small and decay fast, and, on the other hand, there is almost always a requirement for intermolecular alignment, or orientational restriction, in order to achieve chiral recognition. However, using more substituents such that more interactions promote alignment does not necessarily lead to better enantioselectivity in the self-assembly process. This is because a more complex Potential Energy Surface (PES) is generally characterized by an increased number of competing minima with very different structures.

There is therefore a balance between providing appropriate molecular features to achieve alignment, preferably on an extended scale, in the condensed phase, and retaining specificity when intermolecular interactions become complex. A foray into the challenges of reaching such a balance is provided by Molecule A1 of the present work, which we have also studied in previous Chapter (model B). Molecule A1 is not only a case study in interactional balance, but also for more general effects in condensed phase structure formation: Pair interactions favored heterochiral structures, but com-

peted in this system with multibody and entropic effects, which favored homochiral structures.[30] As a result, surface-supported condensed phase structures oscillated during the simulations between three motifs: structures in which heterochiral double chains were predominant, configurations with several large homochiral rosette clusters, and configurations with heterochiral chains made from alternating homochiral sequences of a few molecules.

In the following pages, we examine the balance between different intermolecular interactions and their effect on chiral self-assembly. We first investigate the relative importance of lateral electrostatic interactions by scaling them down, then by removing some of the charges - Section 4.3. Then, in Section 4.4, we discuss the impact of modifying the steric layout of the molecule (by changing substituents and their positions) on the self-assembly process.

4.1 Models, parameters and simulation details

In previous studies, models incorporating two charge pairs exhibited polymorphic behavior.[143, 146, 147]. Here, we focus on the equilibria between (meta)stable states in such polymorphic systems. We control the balance between polymorphs by changing the specifics of intermolecular interactions, in an attempt to understand how molecular properties, and eventually substitution, can be leveraged to attain the desired self-assembly product.

The molecular models investigated in this Chapter had seven atoms, including two prochiral centers, which became chiral in the two-dimensional restriction (Figure 4.1). Chiral atoms (1 and 5) and spacer groups (2 and 6) carried partial charges in most models, though the effect of eliminating some of the charges was also examined.

In the following pages, atoms 1 and 5 will be referred to as the "inner" and "outer" chiral groups, respectively. The nomenclature refers to their respective positions when micellar structures are formed in condensed phase, with molecular tailgroups gathered in the centre of the micelle, and headgroups positioned on the outside. Specific geometries and partial charges are presented in Tables 4.1 and 4.2, respectively.

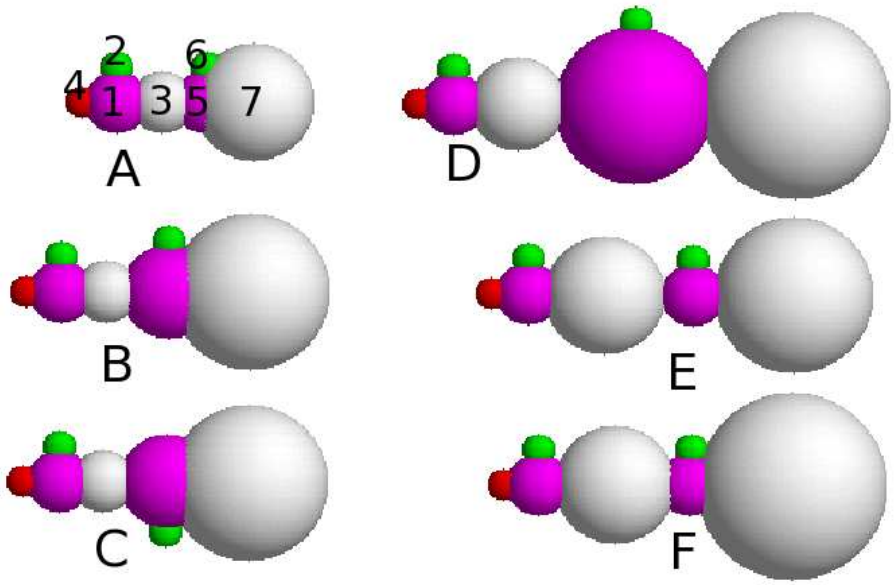

Figure 4.1: Chiral molecules investigated here. Molecules A1-A7 (Tables 4.1 and 4.2) have geometry A and different charges. Atom numbering for molecules B-F is identical to that presented for molecule A. Molecules B and C are diastereomers. As indicated by Table 4.1, each atom is not necessarily representative of a C, N, O, H or another actual atom, but rather of a particular Lennard-Jones interacting species. Chiral atoms are indicated in magenta. Atoms colored in green and magenta typically carried partial charges, as indicated in Table 4.2.

We evaluated the interplay of the electrostatic potential and steric interactions in driving two-dimensional chiral recognition in these molecules. To this end, partial charges of various distributions and magnitudes were considered for the chiral and

Table 4.1: Lennard-Jones parameters for all atoms in molecules A1-A7, and for atoms that were distinct from these, in molecules B-F

Molecule	Atom	σ^*_{ii}	ϵ^*_{ii}
A1–A7	1	1.0	1.0
	2	0.5	0.7
	3	1.0	0.25
	4	0.5	3.0
	5	1.0	1.0
	6	0.5	0.7
	7	2.0	0.25
B, C	5	1.5	1.0
	7	2.5	0.25
D	3	1.5	0.25
	5	2.5	1.0
	7	3.0	0.25
E	3	2.0	0.25
	7	2.5	0.25
F	3	2.0	0.25
	7	3.0	0.25

spacer groups of molecules A1-A7. The geometric asymmetry of the molecule was modulated by varying the sizes of headgroups, outer chiral groups and center groups in molecules A-F. Charges and atom sizes are modified independently, in a linear fashion, to obtain insight into their effects in chiral self-assembly.

Each simulation consisted of 100 molecules in racemic composition, and restricted to evolve in two dimensions. Out-of-plane rotations were previously found to have negligible impact on the overall results[143] and were ignored for computational efficiency in the present study. The study is aimed at understanding chirality upon surface assembly, and therefore bulk (three-dimensional) simulations were not performed. All of our models are prochiral in 3D, though chiral within the confines of the present 2D simulations. An extensive comparison of the 2D and 3D behaviors of

Table 4.2: Partial charges for charged atoms, in fractions of an electronic charge

Molecule	q_1	q_2	q_5	q_6
A1, B–F	0.40	-0.40	0.40	-0.40
A2	0.20	-0.20	0.20	-0.20
A3	0.10	-0.10	0.10	-0.10
A4	0.02	-0.02	0.02	-0.02
A5	0.40	-0.40	0.24	-0.24
A6	0.40	-0.40	0.12	-0.12
A7	0.40	-0.40	0.00	0.00

similar models was carried out in our previous work.[143] Box sizes were chosen such that a low density two-dimensional phase was created, and condensed patterns were not affected by variation of box size. Periodic boundary conditions were found to have no impact on simulation outcomes in these circumstances, and were not employed in any of the reported results. Evaporative events (particles leaving the simulation box) were forbidden, by rejecting moves that lead to evaporation. Simulations were at least 10^{10} steps long and continued until average energies in each replica converged to less than 0.5% - a threshold limited by the computational intensity of the calculations and thermal fluctuations. Simulations continued beyond the convergence criterion did not experience significant structural reorganization. Temperature swaps were attempted in 1% of steps. A step here denotes an attempted molecular move or temperature swaps.

4.2 PESs of dimers and trimers

At the most basic level, the process of self-assembly is driven by two-body intermolecular interactions. In condensed phases, these interactions are modulated by multibody effects and entropic factors. To gain insight into the importance of the

fundamental pair interactions in self-assembly outcomes, we evaluated PESs for like and unlike dimers and trimers. The dimer PES was built directly from the pair potential described in equation 2.7. Relative energies of like and unlike minima indicate whether pair potentials favor homochiral or heterochiral assembly. The persistence of a dimer minimum in the condensed phase structure indicates that pair interactions pay a major role in the self-assembly process. The configurational entropy of a dimer (and by extension of molecules in condensed phases) is related to the width of wells on the pair PES. Furthermore, studying the stability of a dimer minimum within a trimer structure is a first step towards understanding how pair interactions combine in determining the total potential of a condensed phase, and the importance of multibody effects in the overall self-assembly process.

The pair potential of rigid molecules constrained to evolve in two dimensions depends on three variables: their intermolecular separation and their relative orientation, described by two angles. Choosing to hold one molecule fixed at the origin and rotate and translate the other, the dimer PES can be built by considering the following degrees of freedom: the intermolecular separation r^*, calculated as the distance between the two geometric centers, the azimuthal angle for the position of the geometric center of the second molecule, θ_1, and the rotation of the second molecule around its own z axis, θ_2.[30]

To describe the layout of the dimer PES, two types of information were accumulated: Minimum dimer energies over all orientations for a given separation, summarized in graphs of minimum energy vs separation, and contour plots of angular dependence of the dimer energy for a given separation. The former provided global information about the relative stability of like and unlike dimers. The contour surfaces provided information about well depths and widths, for separations deemed relevant

from the analysis of r-dependent graphs or from condensed-phase simulations. Only minimum energy–separation graphs were explicitly included in the discussion below.

Trimer PESs were also examined. Because of the complexity of uniformly sampling a trimer configurational space with six degrees of freedom, we restricted the calculation to evaluating the strength of interactions between dimer minima and a neighboring third molecule. We consider here the interaction potentials between a third molecule and the most stable like and unlike dimers. The initial dimer was held fixed, with its center of mass at the origin, while the third molecule underwent translations and rotations as described above for the dimer case. In several cases, the initial dimers presented broad minima in energy–separation graphs. Where this was the case, the initial dimer structure for trimer PES calculations was chosen to correspond to condensed-phase average intermolecular separations.

4.3 Electrostatic effects

4.3.1 Reducing polarity

In Molecule A1, lateral electrostatic interactions break micellar organization to develop double chain structures. One way of limiting this effect is to directly scale down molecular polarity, thus reducing the importance of electrostatic interactions relative to steric effects. Condensed phase structure in molecules A1-A4, with progressively weaker partial charges ranging between 0.2 and 0.01 fractions of an electron is presented in Figure 4.2(a)-(d). Average fractions of molecules with exclusively like neighbors are shown as a function of temperature, in Figure 4.2(e).

While condensed phase structure in Molecule A1 [Figure 4.2(a)] was dominated by heterochiral structures, Molecules A2 and A3 presented well-separated homochiral

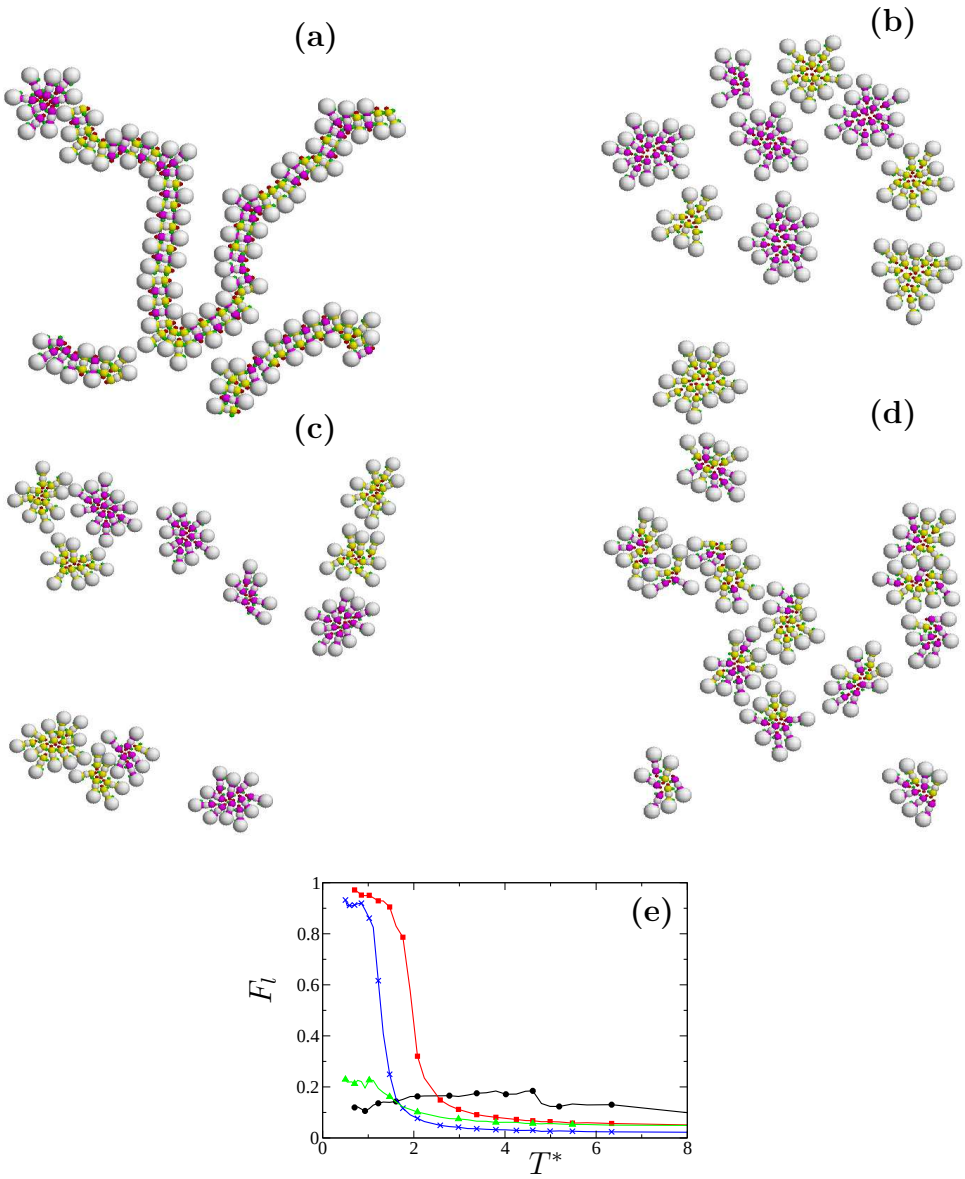

Figure 4.2: The impact of scaling down polarity on two-dimensional condensed phase structures. Simulation snapshots for racemates of molecules A1-A4 are presented in panels (a)-(d), respectively. Opposite enantiomers are presented with magenta and yellow chiral atoms, respectively, for visual clarity. Reduced temperatures corresponding to condensed phase were used in all panels, with T*=1.1, 1.0, 0.8 and 0.7 presented in panels (a)-(d), respectively. Different reduced temperatures are presented because the condensation transition temperatures changes with the intensity of the overall potential. Panel (e) depicts the temperature dependence of the fraction molecules involved in like local structures. Black circles, red squares, blue stars and green triangles correspond to models A1-A4, respectively.

micelles, with as many as 95% of molecules interacting with exclusively like neighbors [Figure 4.2(b) and (c)]. Clearly, weaker lateral interactions preserved micellar structure in condensed phase, and further provided alignment within the micelle, resulting in extended homochiral structures. When lateral interactions decreased below a certain threshold however, as for example in Molecule A4, steric interactions became the major driving force in condensed phase formation. This led to loss of alignment within the micelle, and the formation of heterochiral structures [see, for example, Figure 4.2(d)].

It is worth noting that rosette structures formed by molecules A2 and A3 were not entirely circular. Rather, a more compact structure was achieved by electrostatic alignment in a roughly two-tier fashion: one tier of molecules gathered their tailgroups together in the micelle interior and had their inner dipoles aligned. A second tier of molecules were interspersed through the first tier micelle, with their inner dipoles lined up with outer dipoles of the first tier molecules.

Configurational minima on the like and unlike dimer PES are presented as a function of intermolecular separation, in Figure 4.3(a). Unlike dimers were more stable for Molecules A1 and A2, like and unlike dimers presented similar stabilities for Molecule A3, and like dimers had lower minima for Molecule A4. Dimer minima did not correlate well with condensed phase structures and the quality of chiral recognition in any of the systems presented in this section.

In condensed phase structures, interactions between pairs of molecules are coupled in complex ways, particularly as any given molecule has multiple neighbors, and interactions often extend beyond nearest-neighbor range. One first step in understanding this extension of interactions from a single pair of molecules towards condensed phase structures is to examine how a given stable molecular pair interacts with one addi-

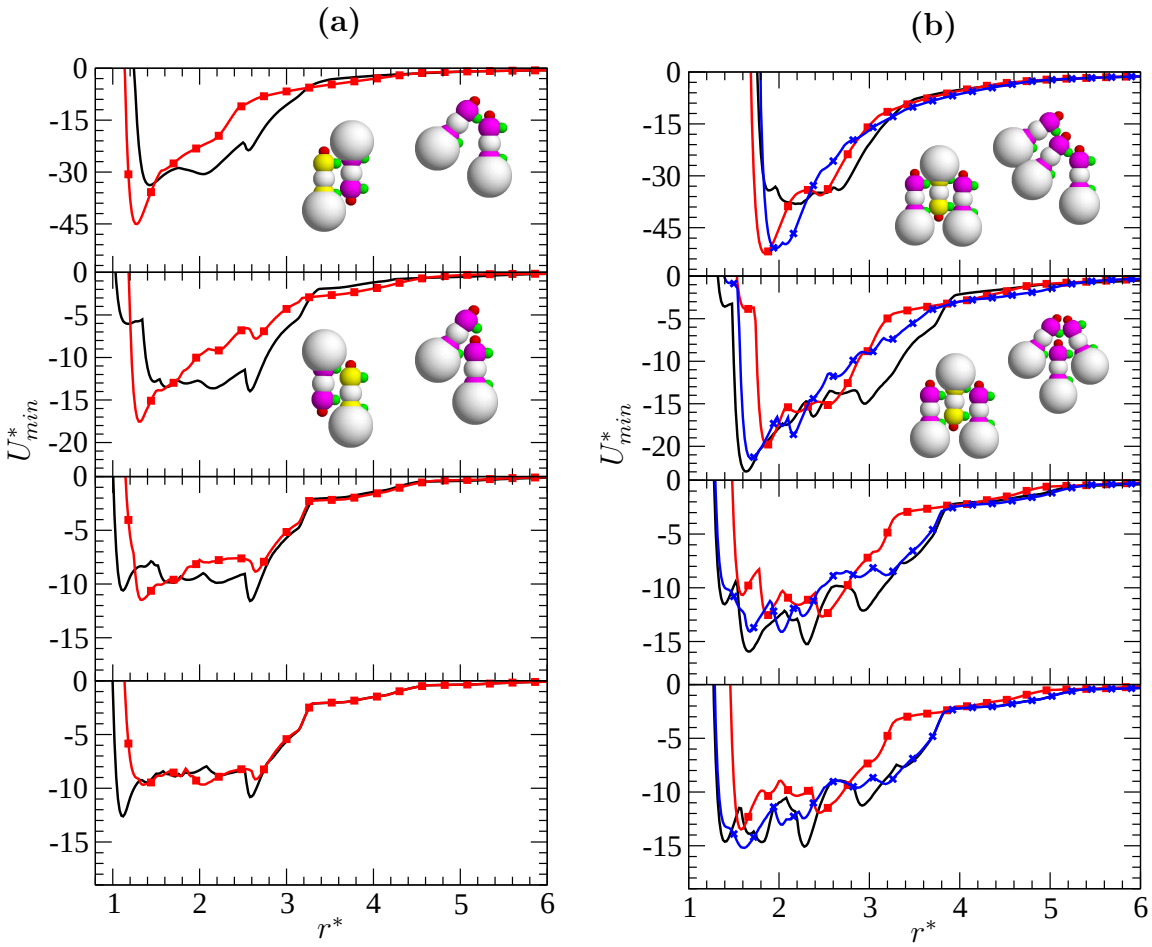

Figure 4.3: Minimum energies, $U^*_{min}(r^*)$, for dimers (a) and trimers (b) of molecules A1-A4 (in from top to bottom, respectively), as a function of intermolecular separation. In (a), like and unlike dimers are presented with black line and red squares, respectively. In (b), LLL (black line), LDL (red squares) and LLD (blue stars) trimers are presented, respectively. Trimer PES's were restricted as discussed in Section 4.2. Minimum energy dimer and trimer (LLL and LDL) structures are also included for molecules A1 and A2.

tional molecule. Binding energies for LLL, LLD and LDL trimers (where L and D are the two enantiomers of a given molecule) are presented in Figure 4.3(b). Specifically, the graphs represent the binding strength between the third molecule and the original minimum energy dimer (LL/like or LD/unlike), considered in its orientational minimum at the average condensed phase intermolecular separation.

Because configurations were restricted to a planar surface, the third molecule neighbored most closely one of the dimer participants. As a result, the trimer binding energies presented in Figure 4.3 reflect primarily the interactions between these new near neighbors, and were found to be in the same range as dimer energies. For molecule A1, unlike trimers were most stable, albeit over a limited configurational range. For molecules A2 and A3, like dimers interacted more effectively with a third molecule than unlike dimers could, and stronger binding was achieved within a homochiral trimer. This preference was reflected in the condensed phase through the formation of homochiral rosette structures. In fact, in these molecules, like trimers were stabilized particularly in a two-tier arrangement, in which the incoming third molecule had one of its charge pairs aligned with one of the dimer molecules, and the second charge pair aligned with the other dimer molecule. This arrangement led to approximately equal binding energies between the incoming molecule and the two molecules of the initial dimer, and overall more attractive trimer binding energies.

In molecule A4, like dimers also realized more effective binding to a third molecule than unlike dimers, but the dimer did not discriminate between enantiomers. LLL and LLD minima were just as stable, which was consistent with the condensed phase structure presented in Figure 4.2(d). In fact, for all models, minimum energy trimer structures in Figure 4.3(b) were building blocks for the condensed phase patterns presented in Figure 4.2. This suggests that the examination of dimer and trimer PESs may allow significant predictive insight into condensed phase structural outcomes.

4.3.2 Altering the distribution of charges

We further altered the balance of charges by scaling down only the outer charge pair of Molecule A1. This particular change allowed us to probe the role played by the

rigidity of the dimer structures in chiral recognition in these molecules. In terms of intermolecular interactions, the reduction led to preferential alignment of the inner charge pairs, which had higher charges than the outer pairs. As the magnitude of the outer pair charges decreased, unlike double-chain dimers became less stable than unlike dimers with aligned inner charge pairs [see Figure 4.4(a) - middle panel]. Like dimer configurations also changed, as the importance of outer charge pairs decreased relative to the strong steric tailgroup interactions. The resulting stable wedge-like dimer configurations were more broadly spaced than those seen for Molecules A1-A3, allowing for the contact of inner charge pairs as well as tailgroups.

The broadly-spaced like dimers did not by and large survive in condensed phases, where molecules tend to pack more efficiently. Our trimer calculations illustrated that effect: LLL trimers presented lower-separation structures in which the third molecule was packed in between the dimer molecules. This structure was particularly stable in Molecule A5 [Figure 4.4(b)]. Because of the decreasing importance of the outer charge pair, the low-separation trimer structure became progressively less stable from Molecule A5 to A7. Overall trimer minima were located at larger separations, and LLL, LDL and LLD structures reached comparable energies, suggesting the presence of mixed structures in condensed phases.

Snapshots of the condensed phase structure for Molecules A5-A7 are presented in Figure 4.5. Comparison to Molecule A1 [Figure 4.2(a)] indicates that the reduction of the outer charge pair was a viable avenue to promoting chiral resolution. Although fractions of molecules with exclusively like neighbors were over 70% in Molecules A5-A7, they were also generally lower than those achieved for Molecules A2 and A3. Figures 4.5(a)-(c) show the formation of enantiomeric excess structures rather than the enantiopure islands of Figure 4.2(b) and (c). High enantiomeric excess was due

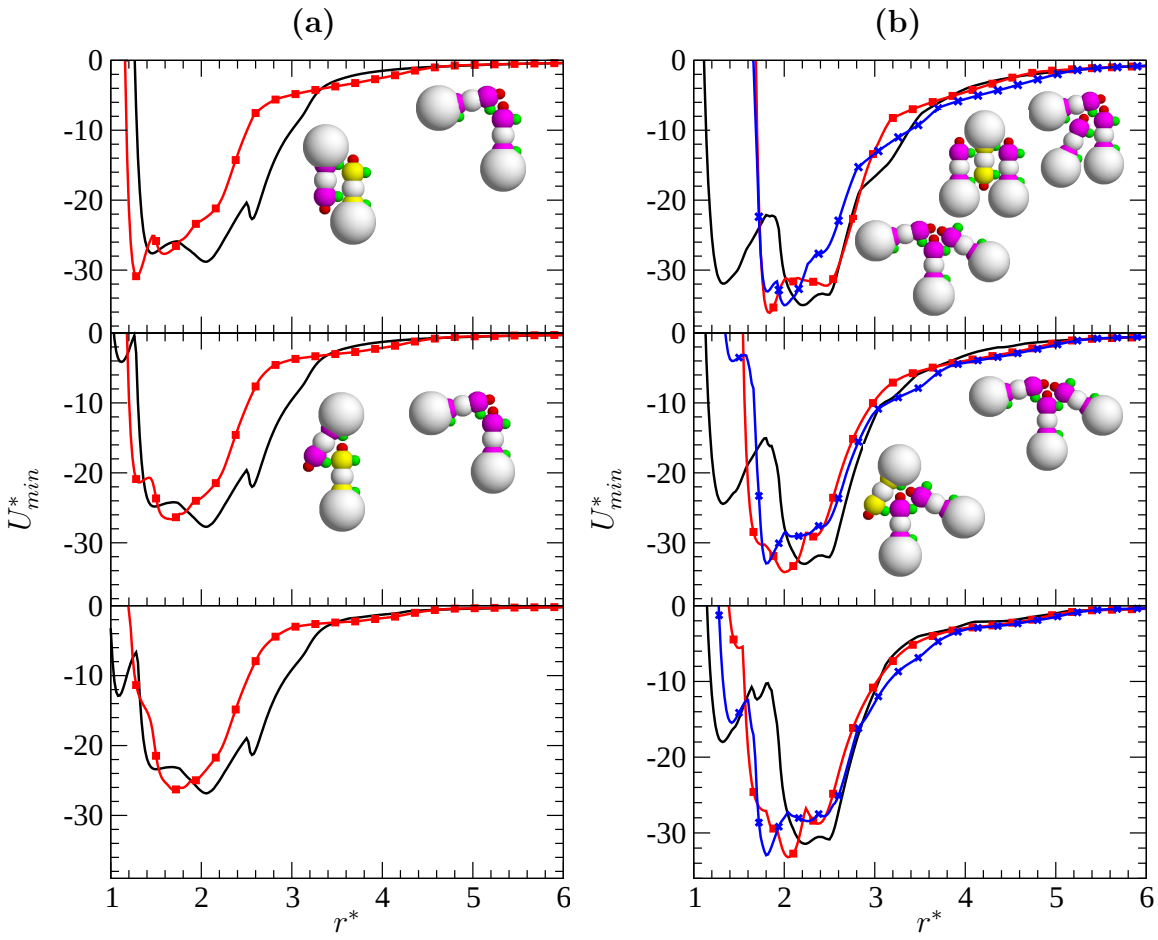

Figure 4.4: Pair potential minima for dimers and trimers with reduced charges in the outer charge pair. From top to bottom, Molecules A5 through A7 are represented. In (a), minimum energies for like (black) and unlike (red) dimers are shown as a function of intermolecular separation. In (b), LLL (black line), LDL (red squares) and LLD (blue stars) trimers are presented, respectively. Dimer structures corresponding to like and unlike minima are also included for molecules A5 and A6. There was no visible distinction between the structures of these minima for Molecule A7 and those presented for Molecule A6. Trimer minimum structures are also presented in (b). For A5, structures for the two LL minima are presented in (b), as both were encountered in condensed phase structure [Figure 4.5(a)].

in these cases to the destabilization of the unlike double chain structure, as well as multibody effects in micelles where many highly attractive tailgroups gathered together. On the other hand, as the two-tier like structures became less stable going

from A5 to A6, less compact micelles with aligned inner charge pairs were formed, allowing intercalation of competing unlike structures. Overall, these competing effects led to better recognition in A6 than in A5 and A7 [See figure 4.5(d)].

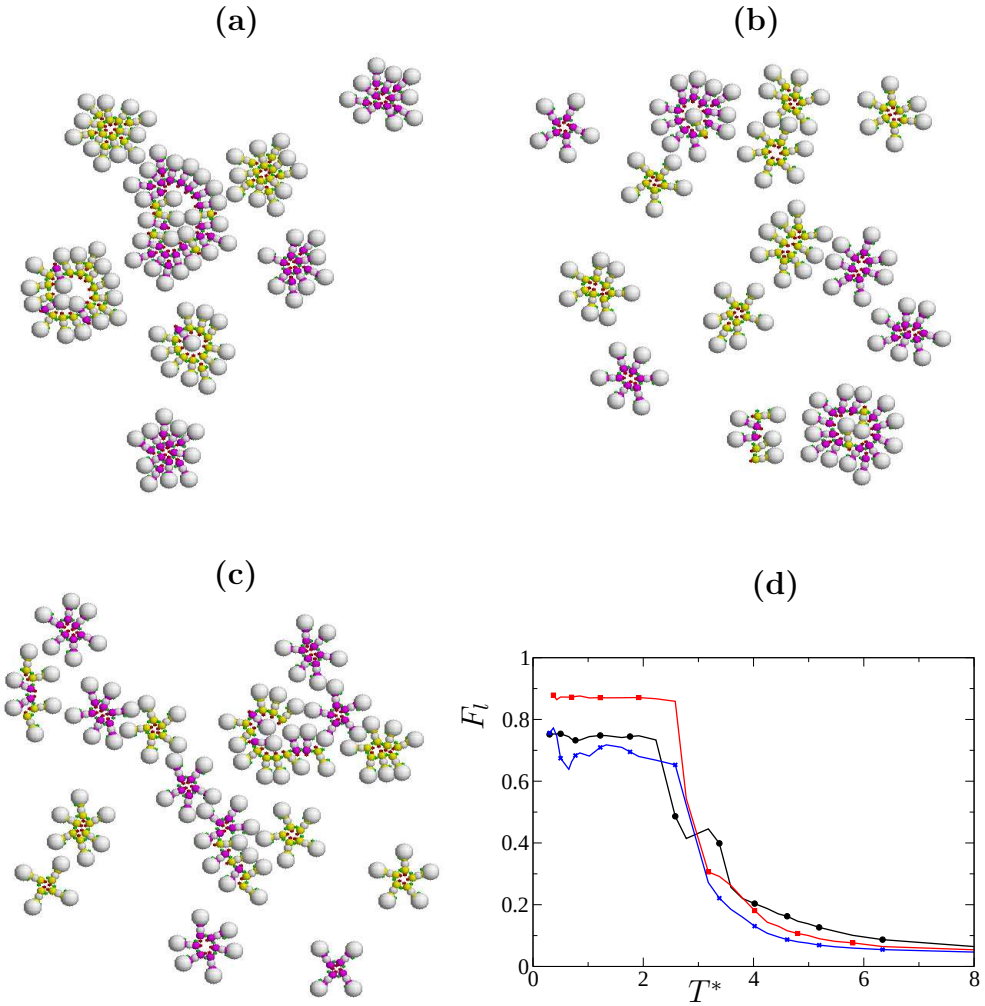

Figure 4.5: The effect of altering charge distribution on condensed phase structure. Simulation snapshots for racemic mixtures of molecules A5, A6 and A7 at T*=1.22 are presented in (a), (b) and (c), respectively. The fractions of molecules with exclusively like neighbors for A5-A7 are given in (d) as a function of temperature, with black, blue and red lines, respectively.

Models in which the outer charge pair was held constant and the inner pair de-

creased in magnitude were also examined (results not presented here). In these systems, dipolar alignment competed with tailgroup attraction in such a way that condensed phases lost their micellar organization and with it, the ability to exhibit chiral recognition.

4.4 Steric effects

Clearly in the surface self-assembly of the molecules examined here, the ability to form micellar structures was an essential precursor to chiral recognition. The preference for micelle formation in these systems was due on one hand to the presence of the strongly attractive tailgroup and weakly attractive headgroup, and on the other hand, to the wedge-like molecular shape. In this section, we discuss the changes arising from modifying group sizes in order to enhance or perturb this overall shape.

4.4.1 Changing the geometry at the outer chiral center.

In Models B-D, we modified the molecular geometry by using larger chiral groups and increasing headgroup size to maintain the wedge-like molecular aspect. In molecule C, we also changed the chirality of the outer chiral group such that B and C are diastereomers. Representative snapshots of condensed phase geometries for racemic mixtures of B, C and D are presented in Figure 4.6(a)-(c). The figure indicates that increasing the aspect ratio of the molecular wedge did not enhance chiral recognition from the reference point of Molecule A1. In mixtures of molecules A1, B and D, between 80 and 90% of molecules have exclusively unlike neighbors. In fact, analysis of the dimer minimum energies for these molecules [see Figures 4.3(a) and 4.7(d)], showed similarities between the dimer minima of A1, B and D. While the location

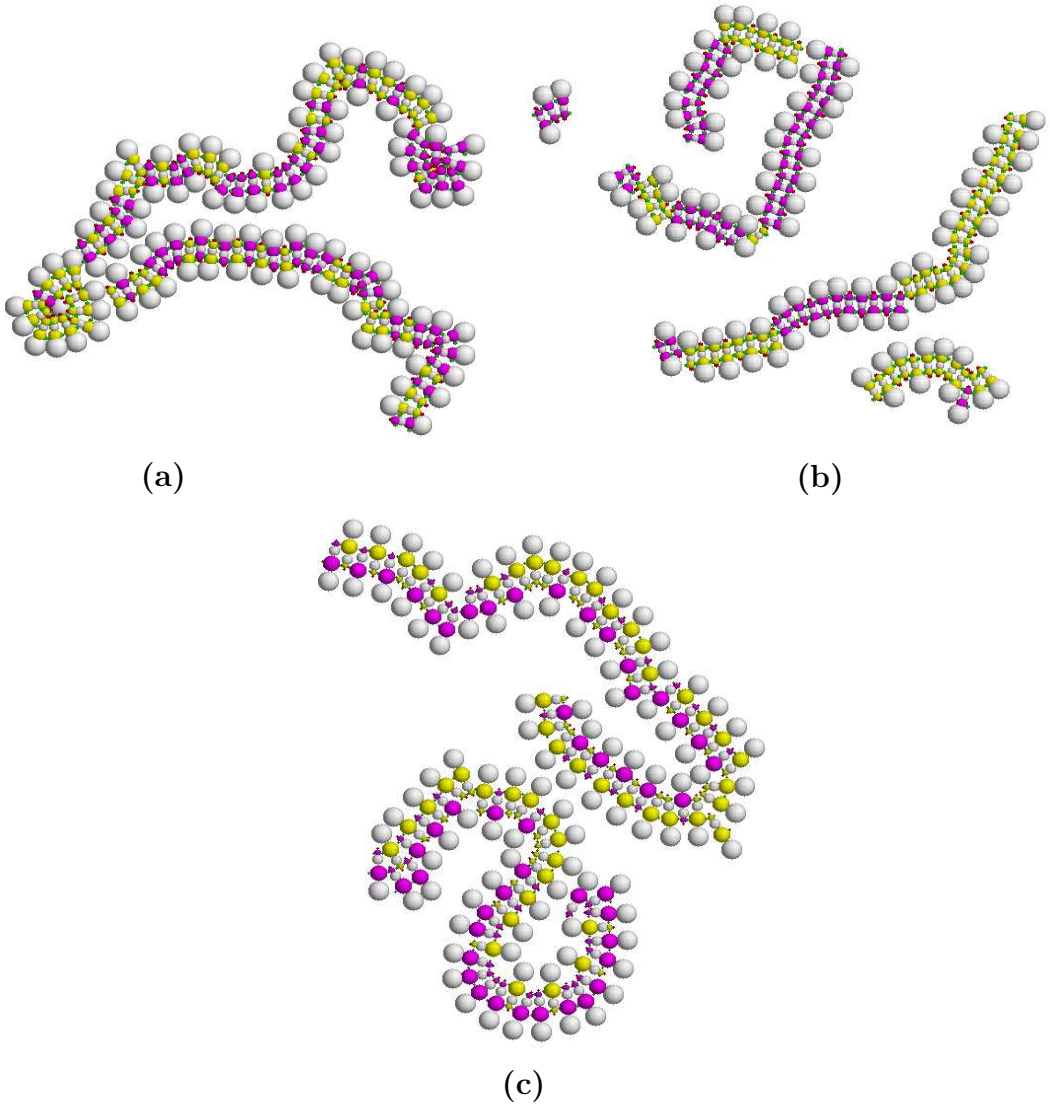

Figure 4.6: The impact of geometry at the outer chiral atom on condensed phase behavior. Simulation snapshots are presented for racemates of molecules B (a), C (b) and D (c), at T*=1.22.

of the minima moved towards larger separations as wedges became broader, the differences between like and unlike minimum energies stayed the same. Decreasing the magnitude of charges again led to improvements in the extent of chiral recognition in molecules B and D (results not included here).

In fact, while results for B closely resembled those from the series of A molecules, the double chains of D molecules were highly stable even when the magnitude of charges was cut in half - though the extent of local enantiomeric excess did increase in the latter case. The underlying reason for this behavior in molecules B and D is that charges on bulkier atoms are forced further apart, thus leading to lower interaction energies. In molecules A1, B and D, the outer charge pairs (of equal magnitudes across the models) were located on progressively bulkier atoms. Like configurations required alignment of the outer charge pairs of all the molecules involved in the homochiral structure, while unlike double chains required the alignment of alternating outer and inner charge pairs. The electrostatic attraction of the heterochiral polymorph occurred therefore at shorter distances than outer pair-outer pair interactions in the homochiral polymorph. This discrepancy in charge pair distances between like and unlike structures further enhanced the preference for unlike structures when increasing the size of the outer chiral atoms, while maintaining the charge distribution.

In order to exploit the stability of the double chain arrangement for molecules with relatively large dipole moments, we inverted the chirality of one of the two chiral atoms. Molecule C is a diastereomer of Molecule B, presenting opposite chirality on the outer chiral atom. Extended homochiral domains were observed for molecule C in condensed phase, with chain-like structure. However, unlike structures of C were not equivalent to like structures of B, and vice-versa. Though structurally similar, double chains of model C were more dominant in condensed phases than they were in model B. This preference was particularly striking when examining the dimer potentials in Figure 4.7, where the like dimer of C can achieve much more stable minima than the unlike dimer of B. The latter was destabilized by steric repulsion between the outer charged spacer atom of one molecule and the large headgroup of the other.

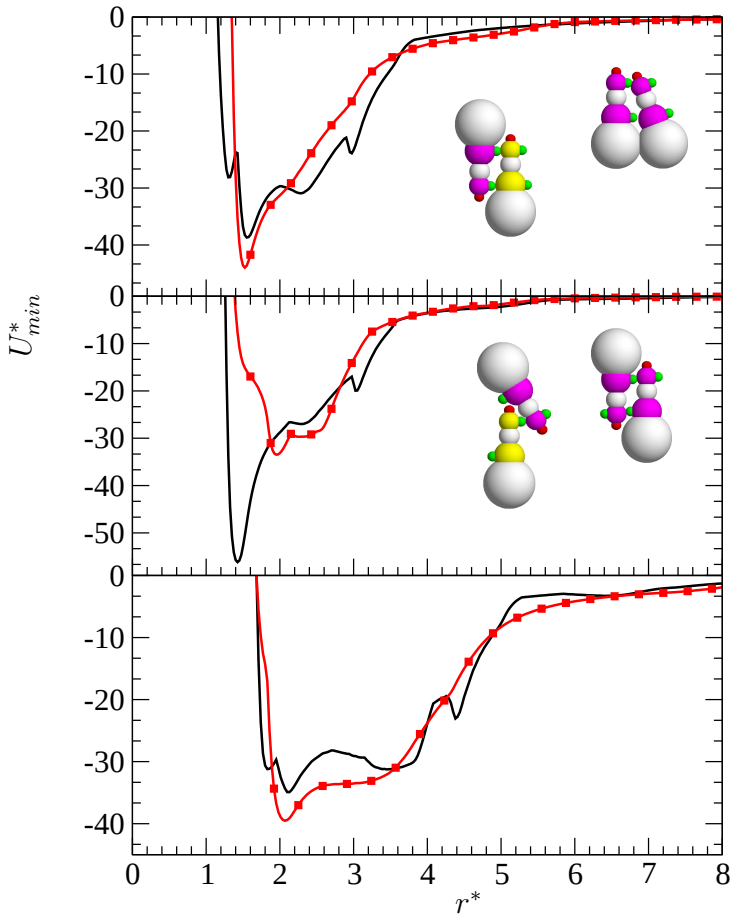

Figure 4.7: Pair potential minima for dimers and trimers with reduced charges in the outer charge pair. From top to bottom, Molecules B through D are represented. Dimer structures corresponding to like and unlike minima are also included for molecules B and C. Black lines indicate like dimer minimum energies, and red squares represent the unlike dimers.

Conversely, unlike micellar configurations were not achieved in racemic mixtures of C, because the necessary wedge-like unlike dimers experienced repulsive electrostatic interactions. Minimum energy unlike dimers for molecule C were weakly bound, which further enhanced chiral resolution in this system. Like micellar geometries were also achievable, but less favorable than the double chain configurations, with well aligned molecular charges. Analysis of stable trimer geometries, not included here, showed

the third molecule forming a wedge with its nearest atom in the stable double chain trimer. This structure was reflected in the condensed phase snapshots [for example, in Figure 4.6(b)], where wedge-like structures were interspersed with double chains, leading to extended homochiral chain-like geometries.

4.4.2 Bulkier center groups.

An alternate route promoting chiral resolution in the models presented here is to destabilize double chain structure formation through steric repulsion. To this end, we created a bulky group at atom 3, and, to maintain the wedge-like aspect of the molecules, also increased the size of the headgroup. These changes resulted in Molecules E and F, with condensed phase structures illustrated in Figure 4.8. These systems were well separated, with about 90% of molecules presenting exclusively like nearest neighbors in condensed phase. The less bulky molecule E allowed further extension of the micelle, by addition of like molecules to the initial structure in a second tier [see, for example, Figure 4.8(a)]. Second tiers were inhibited in model F by the bulky headgroups of the molecules assembled in the central micelle. In essence, the partitioning of electrostatic interactions proved to be an effective route to chiral amplification in these model systems.

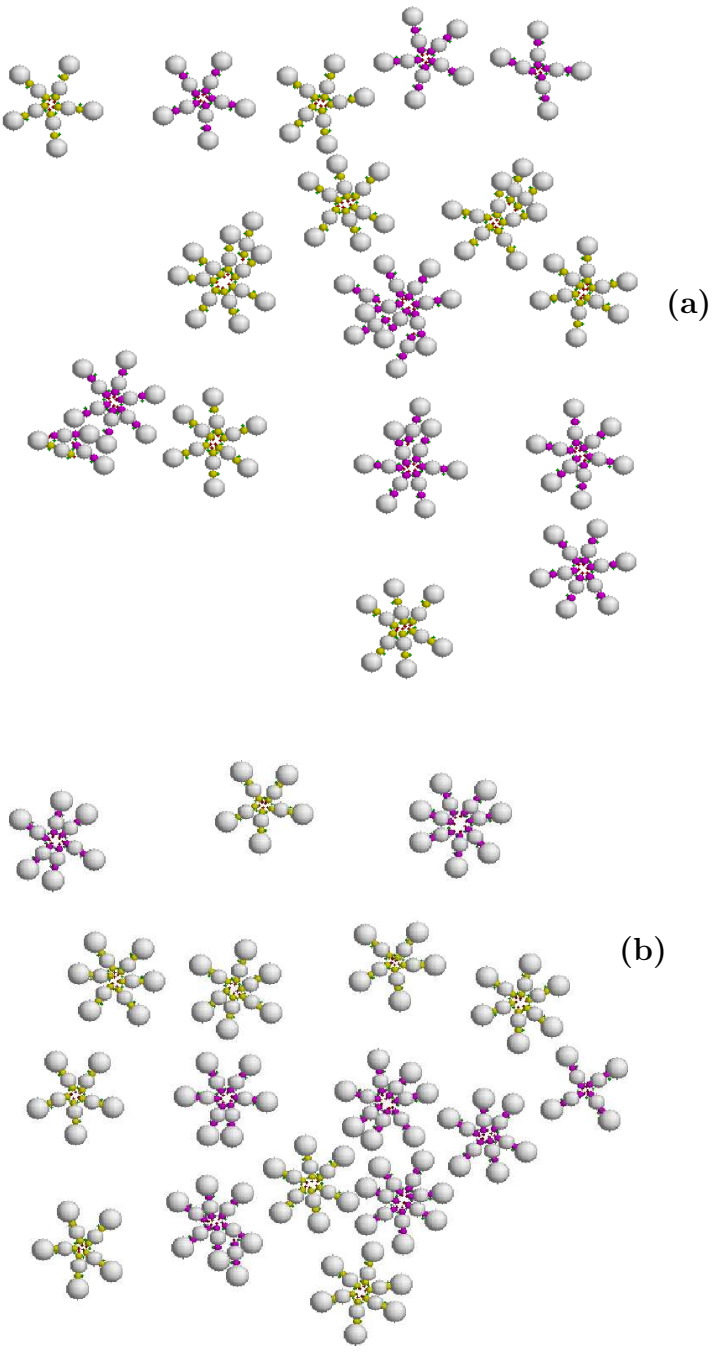

Figure 4.8: Simulation snapshots for racemic mixtures of molecules E (a) and F (b) restricted to evolve in two dimensions, at T*=1.02.

4.5 Summary

We examined the interplay between geometric and electrostatic effects in promoting chiral recognition at the two-dimensional self-assembly of several model systems. We worked with a molecular model that has been previously shown to not undergo the formation of chiral structures at two-dimensional assembly, despite its similarity to simpler models which did so successfully. Our present model instead, exhibited polymorphism, with metastable homochiral structures, and the heterochiral polymorph lower in energy. We examined how molecular attributes such as molecular charge and geometry could be tuned to enhance chiral recognition in the extended racemic mixture. Like and unlike dimer PESs were drawn to understand the effect of these features on intermolecular potentials. Trimer interactions were also analyzed, to gain insight into multi-body effects. Our results showed that dimer potentials alone did not always forecast whether molecules would undergo chiral structure formation at their two-dimensional assembly. However, dimer and trimer PESs together provided significant insight into the complex effects of simple molecular changes on the overall process.

Wedge-shaped molecular geometries, with strongly attractive tailgroups and bulky headgroups, promoted the formation of round micellar structures at two-dimensional assembly. Electrostatic interactions within a micelle would provide the preferential molecular alignment necessary to ensure the homochirality of the micelle. However, in our base model, unlike non-micellar structures were preferentially stabilized by electrostatic interactions. In such a case, our results showed that reducing the magnitude of these charges can enhance enantioselectivity in the self-assembly process. The modality of the charge reduction was also important, as molecules that were

able to form compact homochiral stable structures were most successful in chiral recognition at self-assembly. Models that assembled in two-tier homochiral structures, through discriminating interactions extending to nearest as well as next-nearest neighbors, presented highly enantioselective condensed-phase structures. Models for which the local homochiral structures were more porous allowed intercalation of unlike molecules, with loss of selectivity. Among the geometrical changes we attempted, enhancement of the wedge-like molecular aspect did little to improve enantioselectivity. On the other hand, the forced separation of the outer charge pairs by introducing bulky central groups assisted the formation of predominantly homochiral structures in two-dimensional condensed phases.

Chapter 5

Chiral effects in amino acid adsorption on Au(111): A comparison of cysteine, homocysteine and methionine

Several theoretical studies have focused on the adsorption of cysteine on gold surfaces, but to our knowledge, no such studies exist for methionine or homocysteine. Thiolate, thiol and dithiol adsorption at the Au(111) surface were investigated in several density functional theory studies,[69, 77, 83, 148, 149] as were cysteine dimers.[81] The adsorption of cysteine at the Au(110) surface also received significant attention, with studies considering both native and reconstructed surfaces.[38, 139, 150–152] Several points emerged from this work, foremost being the strong dependence of DFT-calculated binding energies on the initial configuration of the surface-supported molecules. Most studies use known stable gas-phase cysteine/cysteinyl conformers as

initial configurations. For the Au(111) surface, of interest here, the reported enthalpy associated with the exothermic adsorption process was between -0.3 and -1.3 eV, with the most stable conformations bound to the surface via both the thiol and the amino groups.[77, 81, 148] Significant stabilization is reported for cysteine molecules involved in hydrogen bonding with nearby molecules (from -0.3 eV for a monomer to -0.85 eV/molecule in the dimer).[81]

The focus of the work presented in this Chapter is on whether chiral recognition can occur upon surface assembly on a weakly-binding substrate, such as the (111) facet of Au, and compare our results to those obtained on a more reactive surface, the 1×2 reconstructed Au(110) surface. Density Functional Theory calculations were used to examine binding conditions in like and unlike dimers and trimers of chiral amino acids, as precursors of pattern formation in extended systems. In order to understand how the interplay between surface binding and intermolecular interactions leads to chiral recognition upon adsorption, we studied the adsorption behavior of cysteine, homocysteine and methionine, on an ideal Au(111) lattice. To overcome the conformational sampling problems of zero-Kelvin DFT calculations, we used Parallel tempering Monte Carlo to generate a set of target initial structures, which we then further optimized in DFT. The nature of our classical force field was such that the thiol group optimized in PTMC calculations at a hollow site above the surface, where it could maximize the number of nearest Au neighbors. This was of little consequence to the results presented in this work, as further optimization, in a quantum chemical framework, moved this location to the usual off-bridge site. The classical calculations served, however, to a great degree, in finding optimum molecular conformation in the adsorbed state, as most of our DFT calculations equilibrated close to their PTMC-generated initial structure. The adsorption structures of the monomers, dimers and

trimers of sulfur containing amino acids and their binding to the Au(111) surface are described in the Sections 5.3, 5.4 and 5.5, respectively.

5.1 Models and simulation details

The molecular structures of the cysteine, homocysteine and methionine adsorbates are presented in Figure 5.1. Different adsorption modes (thiol vs. thiolate adsorption) were considered. Cysteine and homocysteine were deposited on the gold surface in both the physisorbed R−SH (thiol or mercaptan) and the chemisorbed R−S (thiolate) forms, whereas only the R−S−CH_3 (thioether) form of methionine was employed. All the chiral adsorbates were considered in their dextro isomer, except in unlike dimers where dextro and laevo isomers are assembled together. Results for the laevo isomers are expected to mirror those for the dextro isomers as follows: no chirality aspects enter monomer interactions with the achiral surface, like LL and DD dimers behave identically, as do unlike LD and DL dimers.

For PTMC calculations, the substrate was a two-layer Au(111) slab, with 127 gold atoms. The size of the non-periodic simulation box was chosen so that interactions between image cells used in further DFT calculations would be negligible. Evaporative events (particles leaving the simulation box) were forbidden, by rejecting moves that led to evaporation.

Molecular flexibility was considered by calculating contributions from intramolecular terms to the total energy of the system as described in Chapter 2. Bond lengths were held constant. Only intermolecular nonbonded interactions were considered, described by pairwise atom-based Lennard-Jones and Coulombic potentials.

For DFT calculations the substrate was a three-layer, 168-atom Au (111) slab,

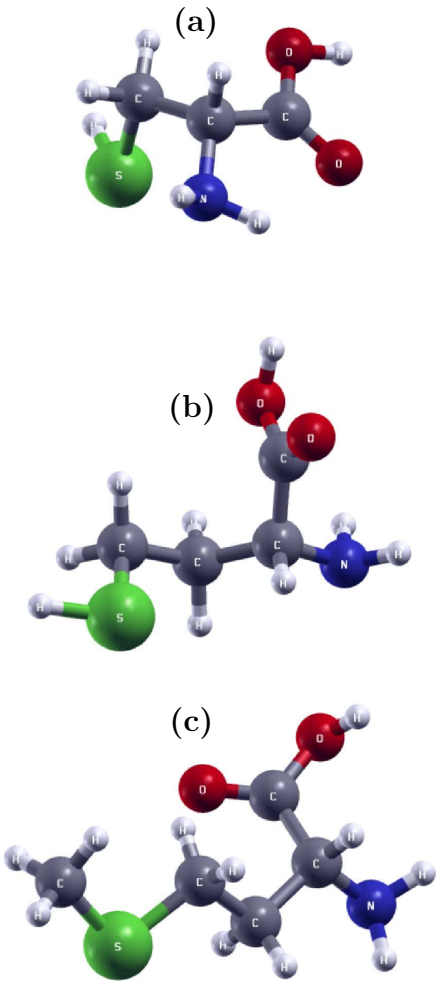

Figure 5.1: Molecules investigated: (a) D-cysteine, (b) D-homocysteine, and (c) D-methionine. Atom coloring is consistent with the figures below.

with periodic boundary conditions. A third ideal Au(111) layer of atoms was added to the PTMC simulation structure to ensure convergence of the surface energy. In all geometry optimizations, two layers of gold atoms were held frozen, while the top layer was allowed to optimize.

5.2 Density Functional Theory (DFT) calculations

DFT is an electronic structure method that was used to study the binding conditions of several organic molecules adsorbed on gold surfaces. The Spanish Initiative for Electronic Simulations with Thousands of Atoms (SIESTA) code, version 3.1, [153, 154] was used for all DFT calculations. The Perdew-Burke-Erzenhof [155] (PBE) generalized gradient functional was employed along with Troulier-Martins [156] pseudopotentials for all atoms. In SIESTA, the standard basis set for valence electrons is double-ζ plus polarization (DZP), and this basis set was used for the calculations reported here, with a pseudo-atomic orbital confinement radius of 1 mRy.[139].

5.2.1 Binding energies

The stability of various adsorbed monomer, dimer and trimer conformations and binding motifs are examined in this work. Binding energies were calculated based on the reaction enthalpies corresponding to the individual process. The chemisorption energy of a thyil monomer is

$$E_b^S = E_{complex} - E_{molecule} - E_{Au_n} + \frac{1}{2}E_{H_2} \tag{5.1}$$

Similarly, the adsorption energy for a thiol (including methionine) is

$$E_b^{SH} = E_{complex} - E_{molecule} - E_{Au_n} \tag{5.2}$$

The stabilization energy of an adsorbed molecule in an m-mer (dimer or trimer) on the surface is, in the case of thyil adsorption,

$$E_b^{m-S} = \frac{1}{m}(E_{complex} - mE_{molecule} - E_{Au_n} + \frac{m}{2}E_{H_2}), \tag{5.3}$$

and for thiols (including methionine) it is

$$E_b^{m-SH} = \frac{1}{m}\left(E_{complex} - mE_{molecule} - E_{Au_n}\right). \tag{5.4}$$

In all equations, E_{Au_n} is the calculated energy of the surface, E_{molec} is the gas phase energy of cysteine, homocysteine or methionine molecule, $E_{complex}$ is the total energy of the adsorbed molecule-surface complex, and E_{H_2} is the gas phase energy of a hydrogen molecule. In the results presented below, all participants in a given reaction were considered at the same level of theory, and with the same basis set.

5.3 Monomer structures and binding

In low-temperature PTMC calculations, monomer configurations in which the entire molecule was parallel to the surface dominated the ensemble. As the temperature increased, the adsorbate oscillated between planar configurations [see Figure 5.2(a), for example] and configurations where the COOH group desorbed [Figure 5.2(b), D-cysteinate at 141 K]. The molecules went through an upright configuration at even higher temperatures [around 200 K for cysteinate, Figure 5.2(c)], and were able to move along the surface at the highest temperatures considered in our simulations. The longer backbones in homocysteine thiolate led to higher backbone desorption temperatures, while physisorbed molecules were able to desorb and move along the surface at lower temperatures than chemisorbed ones.

Naturally, these results are highly dependent on the classical force field, and in

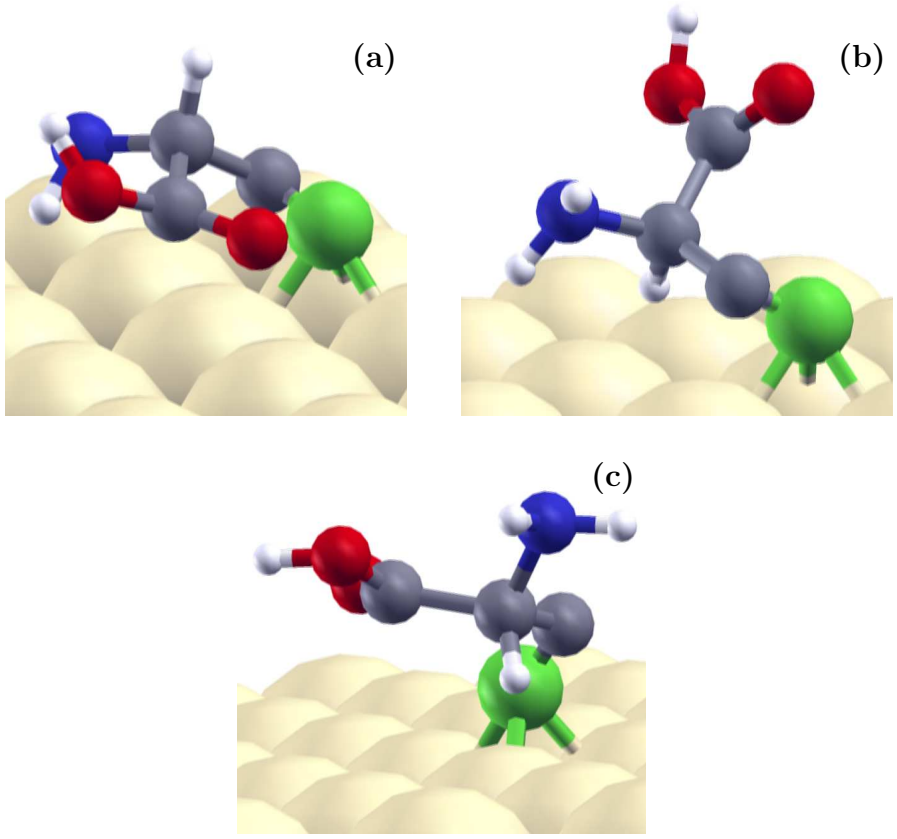

Figure 5.2: Snapshots of PTMC replicas for chemisorbed D-cysteine at (a) 63 K, (b) 141 K and (c) 252 K.

fact could be to some extent predicted by simply examining the interaction parameters of Table 2.1. One of the main issues with the presented force field is its use of generic terms for the surface-molecule interaction, independent of the reactivity of the exposed Au facet.[83] In fact, the Au(111) surface presents low reactivity, even for thiol adsorption, relative to other topologies of the Au substrate. Because of its low reactivity, the Au(111) surface is not well represented by the generic Au-atom force fields. The PTMC calculations tended therefore to overemphasize the interactions of the molecule and the surface for these particular calculations. More reliable adsorbed structures and binding information were pursued by further optimizing

PTMC snapshots using DFT. Low temperature snapshots were generally chosen as initial structures, as DFT operates at 0 K. However, snapshots from intermediate temperatures were also re-optimized, in order to more rigorously explore the differences between the classical and the quantum potential energy surfaces. PBE calculations on Au(111)–adsorbed monomers generally converged to planar molecular geometries, with the thiolate or thiol groups surface bound, and the molecular backbone parallel to the surface. Geometries of the most stable adsorbed D-cysteine, D-homocysteine and D-methionine monomers on Au(111) are presented in Figure 5.3.

Neither cysteine nor homocysteine were able to accommodate efficient binding of both the thiolate and the amino groups on the surface. Configurations where both were bound experienced some conformational strain, which made them less stable. As a consequence of this competition between intramolecular and molecule-surface interactions, the amino-bound and unbound structures of Figure 5.3 [(a) and (b) for cysteine and (c) and (d) for homocysteine thiolates] had very similar binding energies (See also Table 5.1). This behavior was also seen in our PTMC calculations, where configurations with the amino group parallel to the surface (rather than oriented towards it) were predominant at low temperatures. On the other hand, methionine and homocysteine mercaptan, being more weakly attached to the surface by their thiol group, were able to attach their amino group to one of the surface atoms, achieving as a result a competitive overall binding to the surface, despite their weaker sorption mode.

The single-molecule adsorption of D-cysteine on the Au(111) surface was consistent to that observed previously in the troughs of the (110)1×2 reconstructed surface.[139] Troughs in the (110)1×2 reconstructed surface are in essence small-width (111) facets, with 9-coordinated exposed gold atoms on the trough sides. On

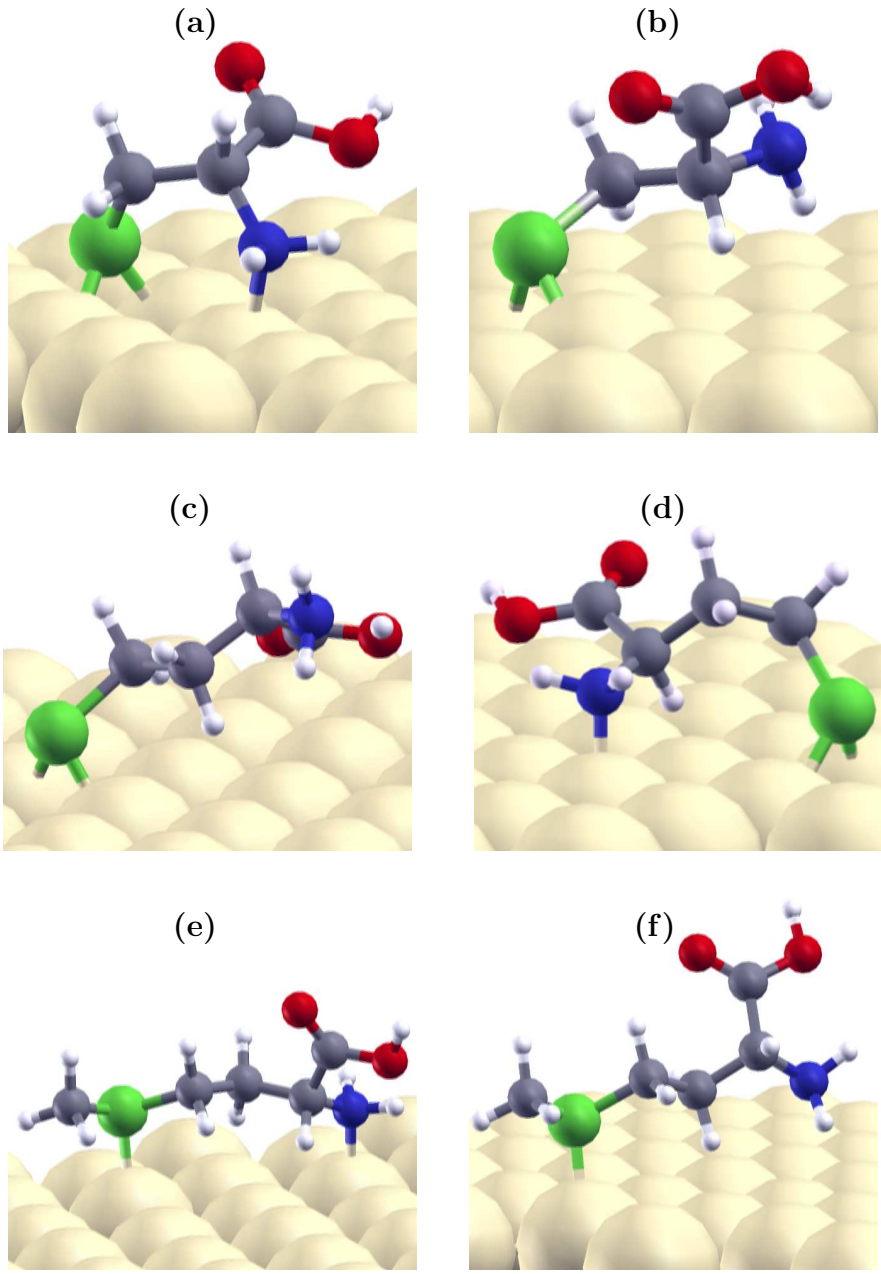

Figure 5.3: Equilibrium chemisorbed structures of D-cysteinate (a,b), homocysteine thiolate (c, d), and methionine (e,f) monomers. The binding energies for (a) and (b) are identical, and those for the more strongly bound homocysteine (c) and methionine (e) are given in Table 5.1. For the more weakly bound homocysteine (d) and methionine (f) monomers, the binding energies were -0.3 eV and -0.7 eV, respectively.

Table 5.1: Monomer binding energies and distances to the nearest Au atoms

Molecule	Surface facet	Active species	E_b[1] (eV)	(d_1, d_2) (Å)
D-cysteine	(111)	thiolate	−0.4	(2.6,2.6)
		thiol	−0.4	(2.8,4.0)
D-homocysteine	(111)	thiolate	−0.4	(2.5,2.6)
		thiol	−0.5	(2.8,4.0)
D-methionine	(111)	thioether	−0.9	(2.7,3.6)
L-cysteine[2]	(110) trough	thiolate	−0.3	(2.6,2.6)
	(110) ridge	thiolate	−0.6	(2.4,3.4)
	(110) vacancy	thiolate	−1.2	(2.5,2.5)

[1]Binding energies are reported to the nearest 0.1 eV to reflect our level of confidence in the DFT-calculated values. The fact that the truncated binding energies for homocysteine and cysteine are identical is fortuitous. For physisorbed structures E_b was corrected by eliminating the basis set superposition error (BSSE).
[2] Reference [139].

the reconstructed Au(110) surface, cysteine preferred binding at the more reactive 7-coordinated ridge sites, and, when sufficient thermal energy was provided for Au atom removal and diffusion, even removed surface reconstruction upon chemisorption. In the latter case, cysteine chemically bound at the resulting 6-coordinated kink sites. Cysteinate adsorption at these sites was very stable, with the thiolate group bound to the kink site and a nearby surface atom, the amino group physisorbed to nearby Au atoms at the exposed (110) facet, and overall adsorption energies of −1.2 eV.

5.4 Dimer structures and binding

Comparative analysis of the interactions between molecules in like (homochiral) and unlike (heterochiral) adsorbed dimers provided a first-order insight into the ability of a molecule to undergo chiral recognition upon surface deposition. Amino acid molecules in their neutral (non-zwitterionic) forms mainly interact through hydrogen

bonding, which led, in the molecules considered here, to stabilization of the dimer over non-interacting monomers. Although both amino and carboxylic groups can be involved in amino acid hydrogen bonding, surface-supported amino acids often achieve their most efficient binding via their carboxylic acid groups.[38, 81, 139] Where such binding was possible, we found this trend to hold in most of the dimers considered here, though structures in which amino groups were involved in hydrogen bonding were also observed. Both of the groups were also involved at times in surface binding, and the overall behavior of the adsorbed dimer was a result of an interplay between intermolecular and molecule-substrate interactions.

PTMC calculations of cysteine (radical) dimers at low temperatures led to minimized structures with thiyl groups close together and molecules upright [see Figure 5.4(a)], optimizing lateral interactions. The upright geometries, with molecular backbones close together, were too unwieldy for the geometric rigour of the double hydrogen bonds between COOH groups. Rather, the amino group on each molecule bound to the oxygens in the other, with sufficient stabilization to compensate for the energetic cost of the upright molecular conformations. Higher temperature replicas found other stable conformations, with thiyl groups further apart and geometries closer to the surface, even if the surface approach came at the cost of lateral dispersive forces and hydrogen bond breaking [Figure 5.4(b)-(d)].

Stronger molecule-surface interaction due to the larger molecular size in homocysteine and methionine led to parallel structures throughout a larger area of phase space, while the added molecular flexibility allowed these molecules to establish stronger COOH−based hydrogen bonds (as seen in the DFT results presented in Figure 5.5)

As for monomers, several of the more stable PTMC dimer configurations were re-optimized using PBE/DZP. The most strongly-bound configurations for like and

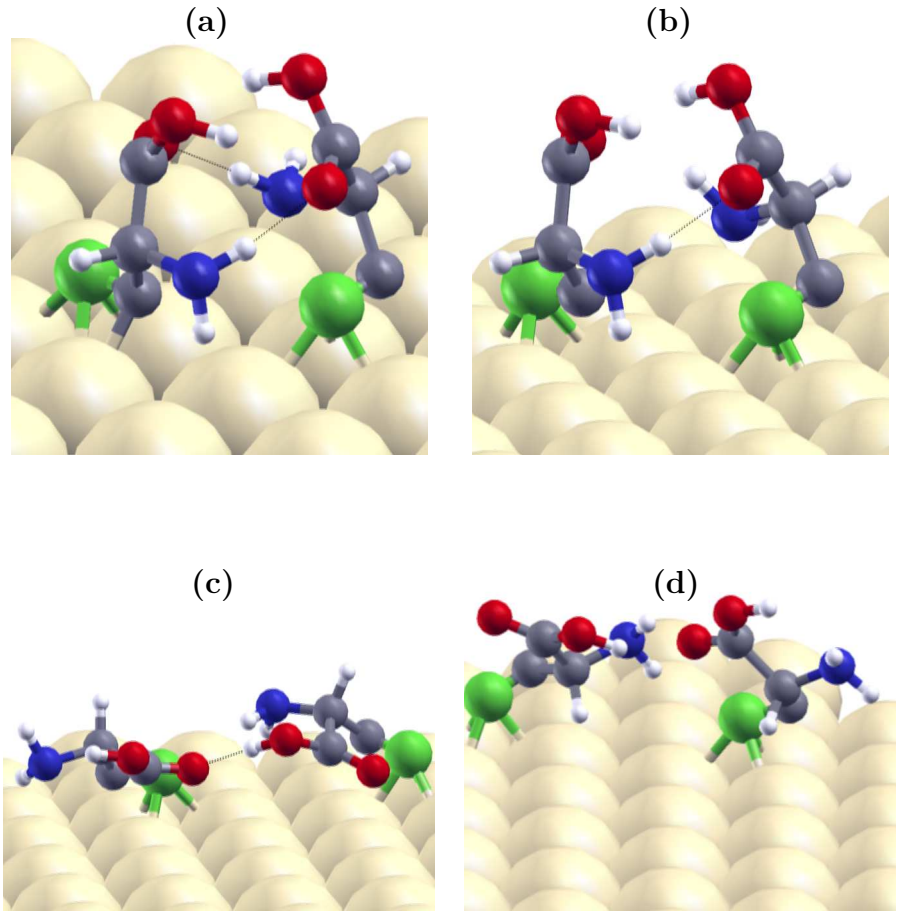

Figure 5.4: Snapshots of PTMC replicas for like chemisorbed cysteinyl dimers at (a) 63 K, (b-c) 141 K and (d) 252 K. At the intermediate temperature, the replica sampled both upright and flat stable configurations, as shown in panels (b) and (c), respectively.

unlike dimers are presented in Figure 5.5, and their surface binding energies are given in Table 5.2.

The difference between the binding energies per molecule presented in Table 5.2 and the monomer binding energies in Table 5.1 is the dimer stabilization energy and reflects lateral (intermolecular) interaction strengths. In this work, stabilization energy by hydrogen bonding in amino acids adsorbed at the Au(111) surface was generally weak. Hydrogen bonding stabilization was about 0.3 eV in cysteine and

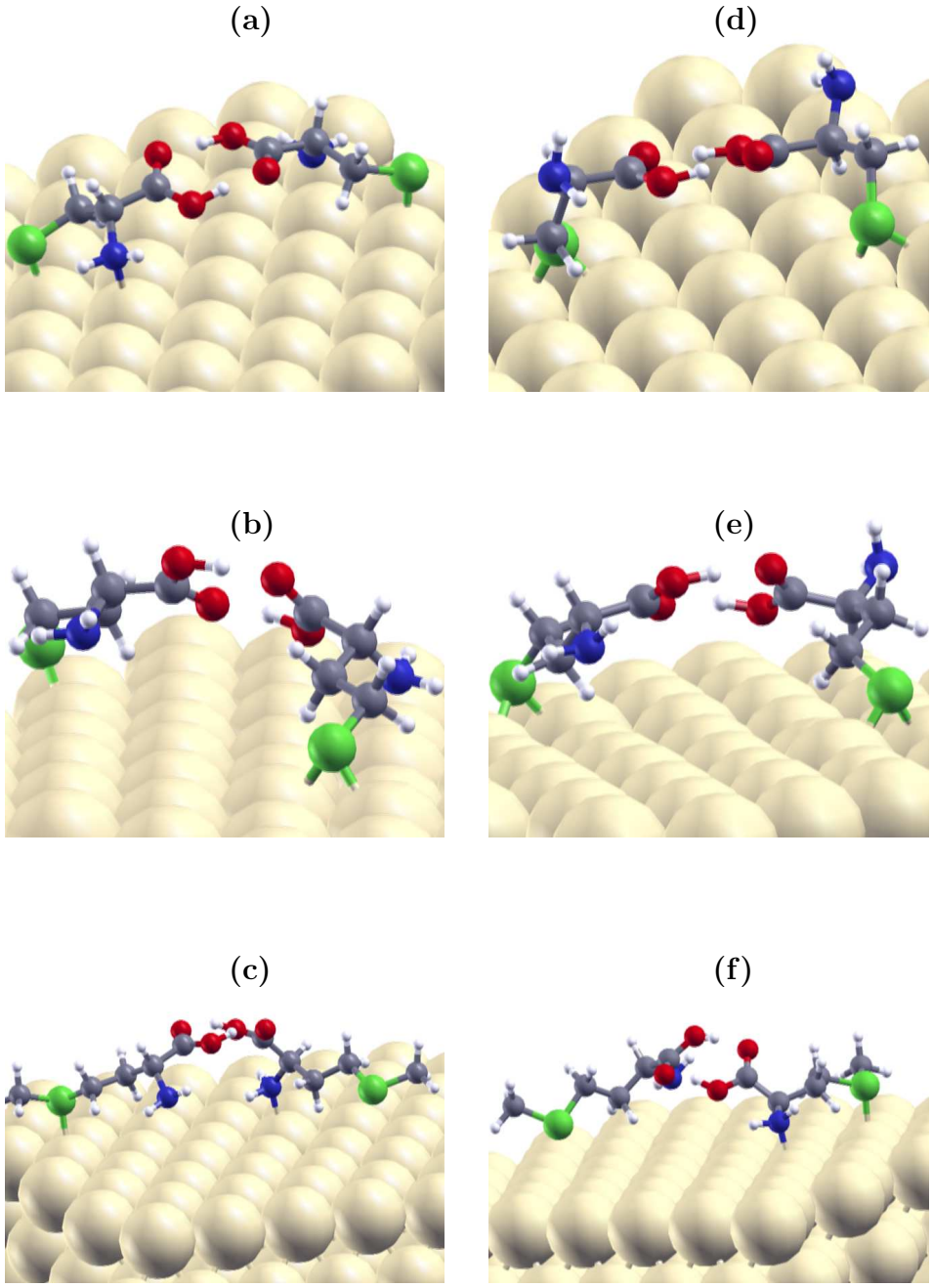

Figure 5.5: The most stable equilibrium adsorbed structures of like (a-c) and unlike (d-f) dimers of cysteine, homocysteine and methionine, respectively. Insets show the top profile of the homocysteine dimers.

Table 5.2: Binding energies per molecule for adsorbed dimers.

Molecule	State	Chirality	E_b[1](eV)	(d_1, d_2)[2](Å)
cysteine	thiyl	DD	−0.7	(2.5,3.5),(2.5,3.5)
		LD	−0.6	(2.5,2.6),(2.6,2.6)
homocysteine	thiyl	DD	−0.7	(2.6,2.6),(2.5,2.7)
		LD	−0.6	(2.5,2.6),(2.5,2.5)
	thiol	DD	−0.4	
		LD	−0.4	
methionine	thioether	DD	−0.9	
		LD	−1.0	

[1]For physisorbed structures E_b was corrected by eliminating the BSSE.
[2]Distances between S and its nearest Au atoms.

homocysteine radical dimers, and negligible in thiol or thioether (methionine) dimers, also reflected in slightly longer hydrogen bonds formed in the latter compounds. These values were weaker than hydrogen bonding stabilization values of 0.3−0.5 eV, found in cysteine dimers adsorbed on 2×1 reconstructed Au(110) surfaces.[139]

It should be noted that cysteine dimers did not H−bind well in their upright PTMC−generated configurations. Instead, more stable dimer structures were obtained upon optimization of monomers highly parallel to the surface. In the optimum cysteine dimer structure presented in Figure 5.5(a), there was a trade-off between dimer stabilization by hydrogen bonding and the required less stable top site thiolate adsorption geometry. The longer backbone of homocysteine did not require a similar trade-off, although adsorption energies were similar.

By and large, the molecules considered here did not exhibit chiral discrimination in their dimer structures formed on Au(111) facets. Although chiral specificity interactions can often be seen as competing with the surface interactions of the molecule, insufficient strength of the latter can lead to an accommodation of a larger range of configurations. This in itself can be detrimental to chiral recognition, which relies on

efficient interactions in configurations specific to one but not the other chiral pair. Figure 5 illustrates how like and unlike dimers of cysteine, homocysteine and methionine can achieve equally strong intermolecular bonding by configurational adjustments that are not sufficiently hindered on the weakly attractive, nonspecific Au(111) surface.

5.5 Trimer structures and binding

A first order insight into the effects of multibody interaction in the formation of surface-supported condensed phase was sought by examining trimers of the three amino acids, in a PTMC/DFT approach similar to that used for dimers and monomers. Like and unlike trimers were examined: like trimers were homochiral, while unlike trimers had one molecule of opposite chirality to the other two. As shown in Table 5.3, adsorbed molecules experienced negligible stabilization upon trimer formation, while the more effective dimer binding in homocysteine radicals was slightly inhibited in the trimer structure.

Table 5.3: Binding energies per molecule for adsorbed trimers.

Molecule	State	Chirality	E_b[1] (eV)
cysteine	thiyl	DDD	−0.5
		LDD	−0.4
homocysteine	thiyl	DDD	−0.3
		LDD	−0.4
	thiol	DDD	−0.5
		LDD	−0.4
methionine		DDD	−1.0
		LDD	−1.1

[1]For physisorbed structures E_b was corrected by eliminating the BSSE.

Snapshots of trimer geometries are shown in Figure 5.6. Neither homochiral nor

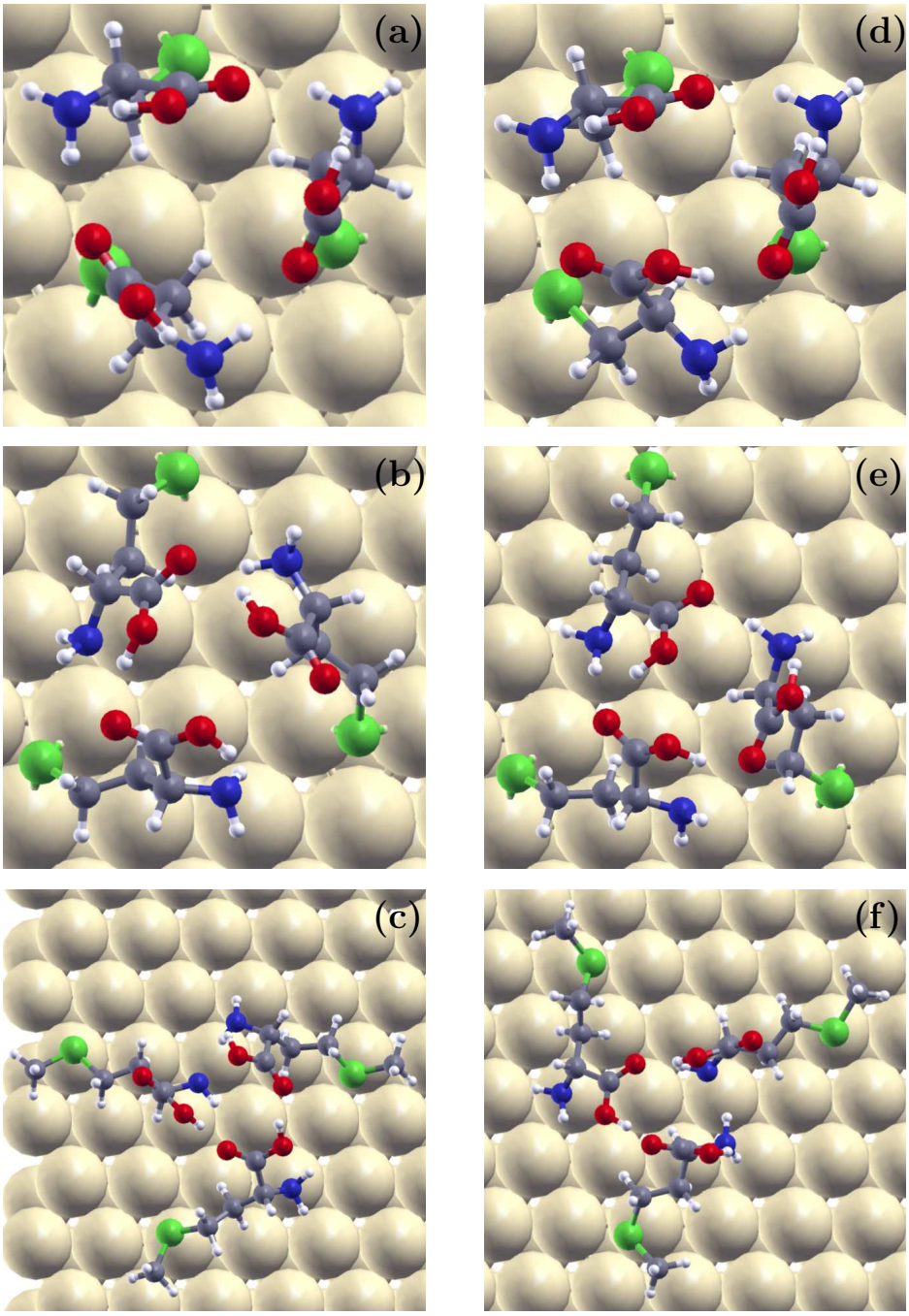

Figure 5.6: The most stable equilibrium adsorbed structures of like (a-c) and unlike (d-f) trimers of cysteine, homocysteine and methionine, respectively.

heterochiral trimers were able to form COOH−based trimer hydrogen bonding. In fact, cysteine and homocysteine radical dimers, which established efficient hydrogen bonding, became less stable when the third molecule was introduced.

In fact, PTMC calculations showed low-temperature trimers in well-arranged, hydrogen-bound configurations for all of the amino acid molecules considered here, but these configurations lost cohesion in the subsequent DFT runs. In the DFT optimization, thiyl groups relocated from hollow sites to bridge sites, and the overall molecular adjustment led to loss of H−bonding in the cluster, or involvement of the amino groups in the H−bonding. In the physisorbed homocysteine and methionine on the other hand, the interactions between the thiol group and the surface atoms were weaker. H−bonds were preserved at the cost of even weaker SH–Au interactions, with the end result being a similar binding energy per molecule as in the case of adsorbed monomers.

5.6 Summary

We examined the surface binding of momomers and formation and stability of like and unlike dimers and trimers of sulfur containing amino acids using DFT approach. The initial structures were identified by PTMC simulations and were further PBE-optimized. Molecules bound to the surface mainly through sulfur atom, and only when both sulfur location and a least molecular deformation allowed, it bound through nitrogen as well. By and large, chiral recognition was not observed upon surface assembly of cysteine, homocysteine and methionine on a weakly-binding substrate, such as the (111) facet of Au surface. The molecules did not discriminate between enantiomers upon formation of dimer and trimer structures which were described by

similar binding energies. Dimers were stabilized through relatively strong hydrogen bonding between carboxyl groups, whereas COOH−based trimer hydrogen bonding was generally inhibited.

Chapter 6

Self-Assembly of cysteine and related chiral amino acids on Au(111) surfaces: A Parallel Tempering Monte Carlo Study

In this Chapter, theoretical studies of enantiopure and racemate extended systems of sulfur containing chiral amino acids adsorbed on Au(111) surfaces are presented. Different molecular states of cysteine, methionine and homocysteine and their self-assembly are considered. We examine the surface self-assembly and the stability of the adsorption patterns over a range of temperatures using Parallel Tempering Monte Carlo method. Extended structures of neutral cysteine, homocysteine and methionine formed upon adsorption and were mostly stabilized through hydrogen bonding. As seen in Chapter 5, two substituent groups may participate in hydrogen bonding : the carboxyl group and amino group. The most efficient binding, however, was achieved

by carboxyl groups. Amino groups were also seen to be involved in hydrogen bonding with carboxyl groups and rarely with other amino groups. These two substituents occasionally participated in binding with the gold surface.

6.1 Simulation Details

We examined enantiopure systems composed of 50 molecules and racemic mixtures of 100 molecules adsorbed on a gold surface, in a simulation box, with no periodic boundary conditions. The size of the simulation box, and of the substrate, respectively was large enough that it did not impact the density of the resulting structures, at the temperatures of interest here. Evaporative events were forbidden, by simply rejecting moves that led to evaporation. The energy of the system was described in equation 2.3 as a sum of intramolecular and intermolecular potentials. Model molecules of cysteine, homocysteine and methionine were described and shown in Chapter 5 (Figure 5.1). The gold surface used here was modeled using a one layer Au(111) slab. The number of atoms depends on the molecules that were adsorbed. Larger molecules needed a larger surface in order to keep the density relatively similar between different systems, within low- to medium-coverage conditions. We roughly calculated the surface coverage using rectangular molecular footprints of the most common adsorbed molecular geometry. The surface coverage, S_c, was calculated as follows:

$$S_c = \frac{N \cdot S_m}{S_s} \tag{6.1}$$

where N is the number of molecules, S_m is the rectangular molecular footprint and S_s is the gold surface area. The rectangular footprint area, S_m, was calculated as:

$$S_m = (x_{max} - x_{min}) \cdot (y_{max} - y_{min}) \tag{6.2}$$

where x_{max}, x_{min}, y_{max} and y_{min} were the maximum and minimum of x and y atomic coordinates of the adsorbed molecule. The estimated surface coverage was less than 40%, and consequently the actual coverage was even lower.

6.2 Extended systems of D-cysteine

The generally accepted argument is that thiols chemisorb on gold surfaces by homolytic cleavage of the mercapto group near the substrate, with the formation of a covalent S−Au bond, and an adsorbed H radical or molecular H_2.[38, 66, 67] Prior to the fission of the mercapto bond, the molecule is considered to be physisorbed. This mechanism varies widely depending on the identity of the mercaptan, the presence of other binding groups, the nature of the gold surface, as well as environmental conditions such as annealing temperature and surface coverage.[35, 43, 68, 69, 157] In fact, for many coverage conditions, thyil radicals coexist with intact thiols. In our study, thiols and thyils systems were treated specifically in different simulations. The stronger interaction between thyils and gold was described by a larger value of the Lennard-Jones energy parameter (see Table 2.1). We found that the adsorption patterns were largely unaffected by the presence or removal of the hydrogen atom on the thiol group.

6.2.1 Adsorption in thyil form

A simulation snapshot of D-cysteine in its neutral thyil form onto a Au (111) surface is shown in Figure 6.1. Molecules were involved in extended structures in which

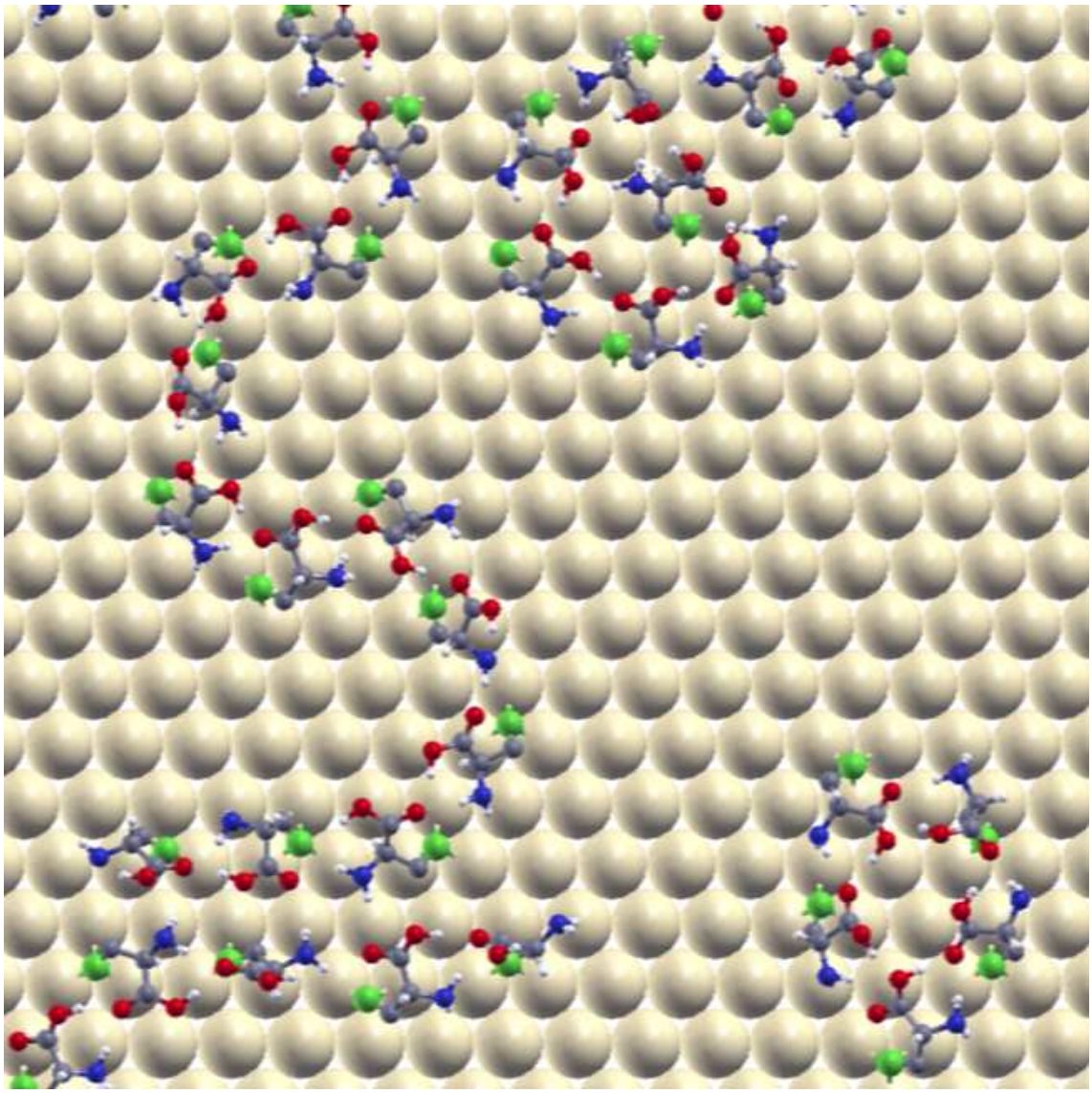

Figure 6.1: A simulation snapshot of D-cysteine in thyil form adsorbed on Au(111) surface at T=296 K.

the thyil groups bound to three-folded hollow sites. The preference for the hollow

sites where sulfur maximized its number of gold atom neighbours was driven by the centrosymmetric Lennard-Jones potential that was used to describe the S−Au interaction. Our previous study, however, showed that in a quantum chemical framework sulfur location moved generally to the bridge site.[158]

Cysteine molecules were mainly involved in two types of structure : rosette-type micellar structures of four to eight molecules and extended chain configurations. The rosette clusters had carboxyl groups involved in hydrogen bonding in the centre of the cluster pointing slightly away from the surface, whereas the thyil groups were expelled toward the exterior of the cluster and bound strongly to the gold. The amino groups were pointing towards the surface and were seen to engage in hydrogen bonding with carboxyl groups. Hydrogen bonding stabilized the chain conformations of cysteine as well. Molecular chains, however, were slightly less stable than round structures due to the lack of hydrogen bonding between molecules that belong to the ends of the chain, since the molecular binding to the surface and intermolecular interaction were relatively similar in both types of structure.

A large range of adsorption temperatures were studied. Due to a very strong sulfur-gold binding, the molecules did not completely desorb from the surface at highest temperatures considered in our simulations. However, they were highly mobile at such temperatures and therefore were able to move along the surface and rearrange. Except for the sulfur, that remained bound to the surface at all temperatures, the backbone of the molecule desorbed at higher temperatures and could undergo at any time the geometry re-optimization. The simulations at the highest temperatures considered here (up to 755 K), may not resemble a real physical system, since cysteine molecules were found to dissociate upon desorption from reconstructed Au(110) surface around 440 K.[43] Nevertheless, these temperatures were useful because they

allowed low-temperature replicas to gather information about regions of the potential energy surface that were only accessible at high temperatures.

A simulation snapshot at a higher temperature (T=403 K) is shown in Figure 6.2. The adsorption patterns seen in the Figure were relatively similar to the patterns formed at room temperature (see for example Figure 6.1). Rosette-type clusters and molecular chains that were stabilized through H−bonding were formed at higher temperatures as well. However, as discussed in Chapter 5, as the temperature increased, the adsorbate oscillated between planar configurations (in which the entire molecule was parallel to the surface), configurations in which the COOH groups desorbed and upright configurations (in which both COOH and NH_2 pointed away from the surface). Similar adsorption configurations were encountered in extended systems considered here. At higher temperatures the fraction of molecules that had the backbone desorbed was larger than at lower temperatures (see Figure 6.3 (b), for example). Accordingly, at 403 K all the configurations mentioned above coexisted, with more molecules adsorbed in the upright configuration than at lower temperatures (Figure 6.3 (a), T=296 K). However, the configuration in which amino group pointed towards the surface and COOH group pointed away from the surface dominated the adsorption pattern at 403 K as it did at 296 K.

6.2.2 Adsorption in thiol form

Since mercaptans may preserve their thiol groups upon adsorption on gold surfaces, the adsorption of amino acids in thiol forms was also considered in our study. A simulation snapshot for the physisorption of cysteine molecules onto Au(111) at room temperature is presented in Figure 6.4. As may be seen in the Figure, the adsorption structures of thiols were relatively similar to the thyils. Extended molecular chains

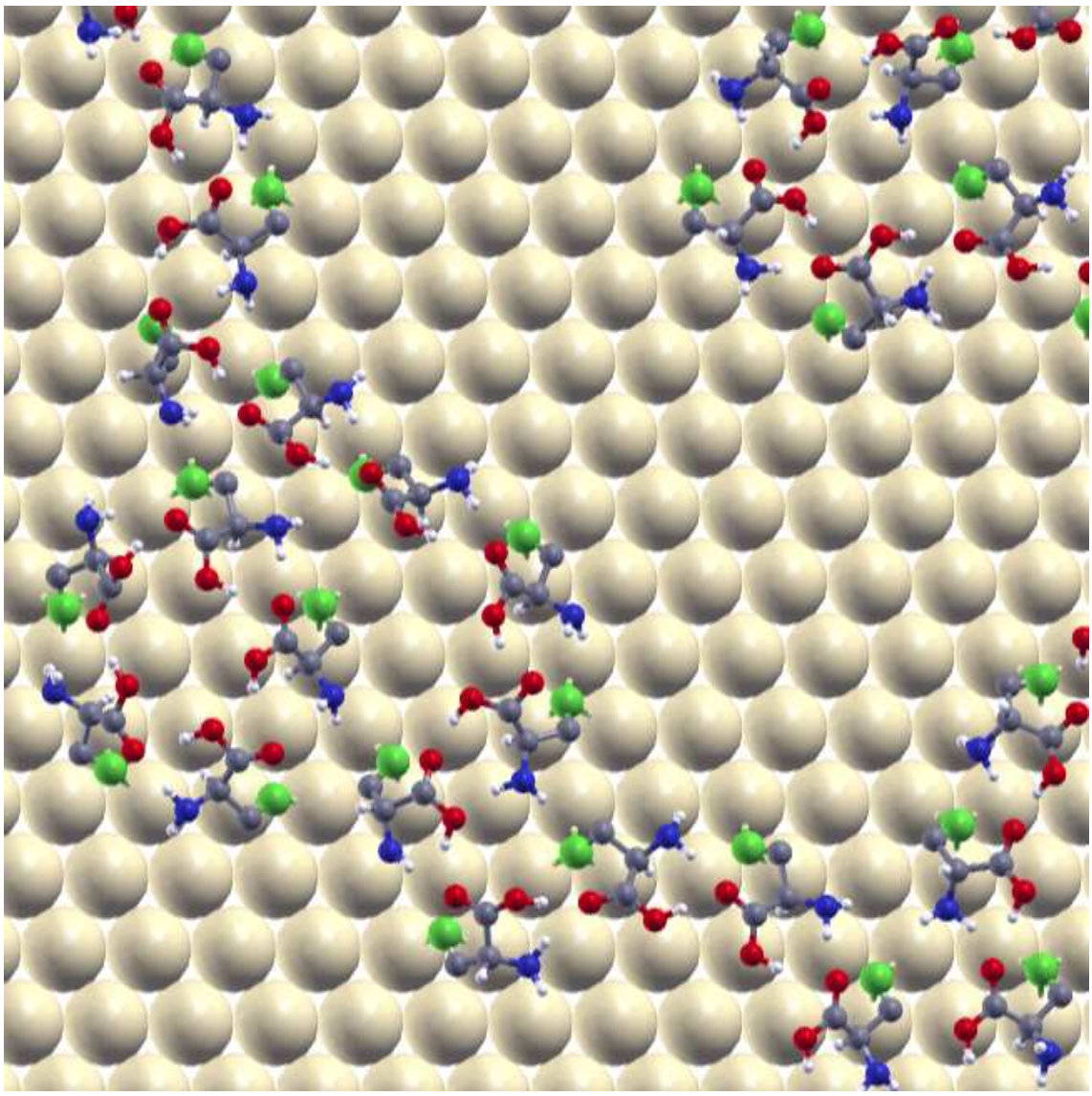

Figure 6.2: A simulation snapshot of D-cysteine in thyil form adsorbed on Au(111) surface at T=403 K.

and rosette clusters were encountered on the gold substrate. Here, however, the sulfur bound mainly to the bridge site. The hydrogen of the thiol group interfered in the binding of sulfur with gold in a hollow site. This locations also did change after geometry optimization using quantum calculations, to those in which sulfur of the

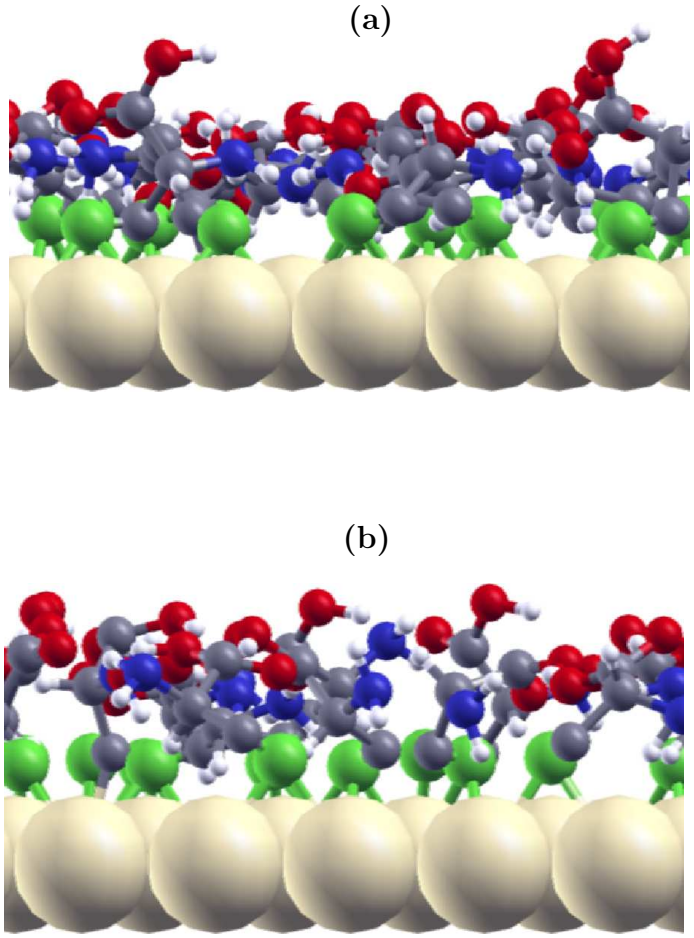

Figure 6.3: Simulation snapshots of D-cysteine in thyil form adsorbed on Au(111) surface at T=296 K (a) and 403 K (b). Side views are presented for a part of the surface and the corresponding adsorption layer.

thiol group adsorbed generally on top of a gold atom. The amino groups of cysteine molecules were generally adsorbed closer to the surface, whereas carboxylic groups were as previously involved in hydrogen bonding with vicinal molecules pointing away from the surface. The S−Au was weaker than in thyil case, but still relatively strong and molecule stayed bound to the surface even at higher temperatures. However, the

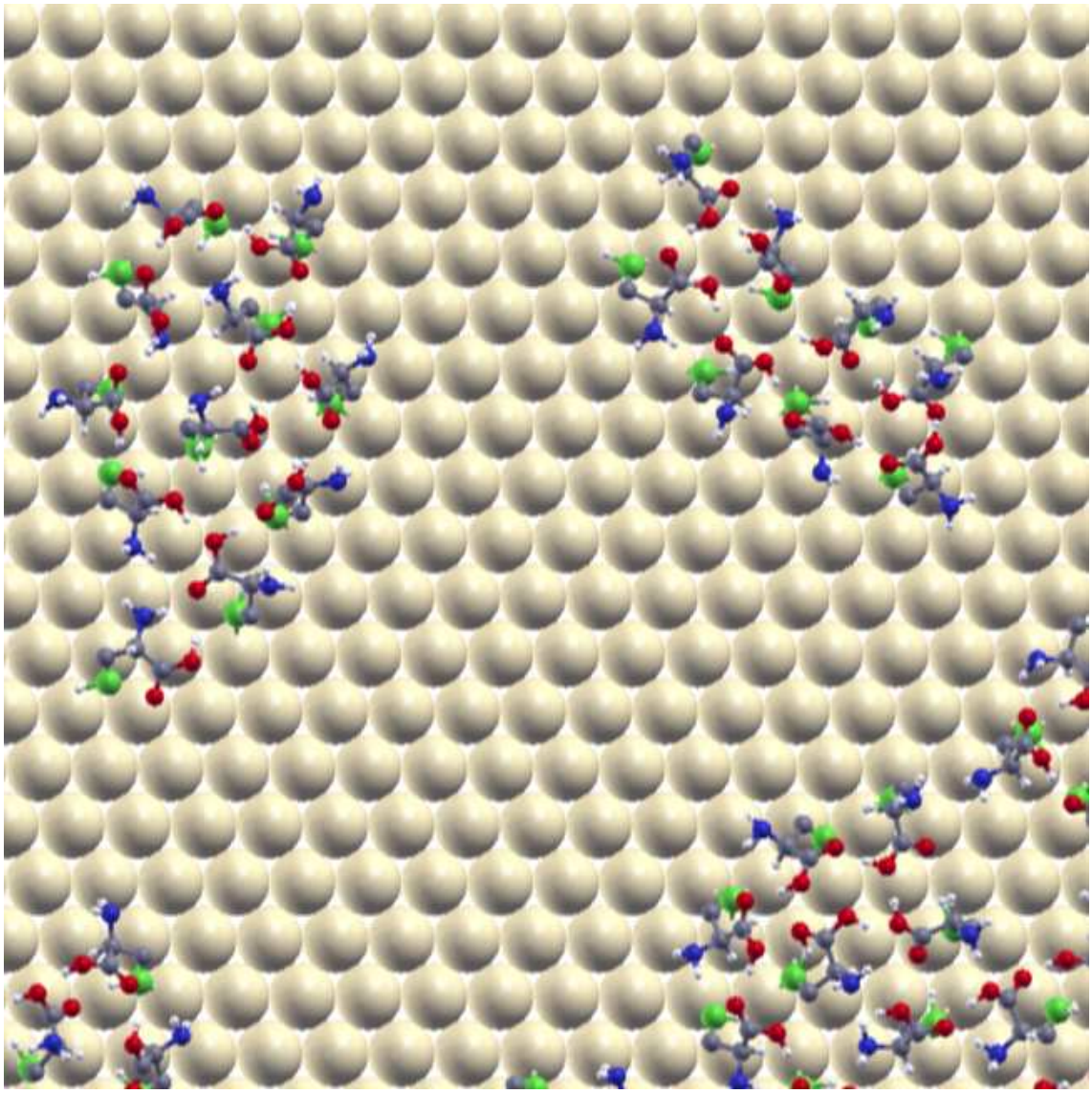

Figure 6.4: A simulation snapshot of D-cysteine in thiol form adsorbed on Au(111) surface at T=296 K.

thiol forms were able to move along the surface at lower temperatures than thyils.

The adsorption patterns of thiols were denser and less ordered than thyil clusters. That was supported by the smaller S−S distances between neighbouring molecules. The S−S distances between nearest neighbours of physisorbed molecules were on average between 4−5 Å, whereas chemisorbed molecules were further apart with S−S

distances between 5.5−6.5 Å. Consequently, thiol molecules interacted less with the surface than thyils and more with each other. Since molecule-substrate interaction was weaker for the thiols, the intermolecular interactions have a larger impact on final adsorption structure, and consequently led to the formation of conglomerates that were more compact than thyils. Thiols established intermolecular H−bonding of similar strength as thyils (O−O and O−N distances of roughly 2.6−2.9 Å). Thus, intermolecular dispersion interaction as well as sulfur locations dictated the self-assembly product for thiol molecules.

At lower temperatures, the adsorption aggregates were slightly more dense, with few S−S distances smaller than 4 Å. A simulation snapshot for physisorbed cysteine at 141 K is shown in Figure 6.5. Similar H−bonded slightly distorted rosette clusters were formed, however, the clusters interacted with each other. Isolated clusters were less encountered at lower temperatures. Snapshots at higher temperature presented similar aspects as the snapshot obtained at room temperature (Figure 6.4).

6.3 Extended systems of D-homocysteine

Homocysteine in either thyil or thiol states assembled on the Au(111) surface in rosette clusters and extended molecular rows, as seen for cysteine. It bound to the surface mostly through sulfur atom in the same hollow sites in the thyil form and at a bridge site as a thiol (see Figures 6.6 and 6.7). Two binding conformations were competing here: (i) an upright geometry in which the molecules bound to the surface through only sulfur atom in "singular" footprint and (ii) a "parallel" configuration, in which the molecules adsorbed relatively flat on the surface.

In the upright conformation, the adsorption patterns of homocysteine were dic-

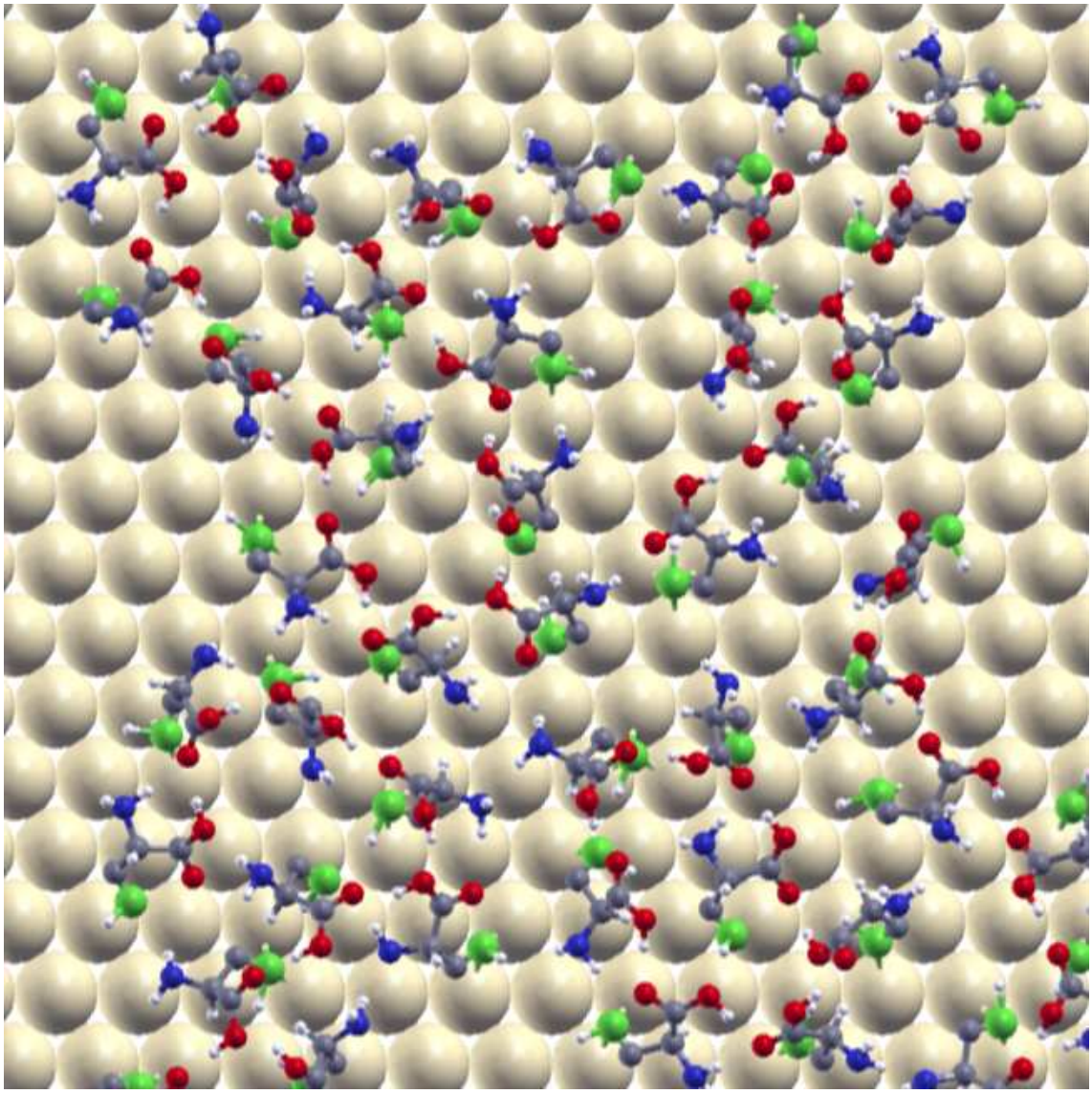

Figure 6.5: A simulation snapshot of D-cysteine in thiol form adsorbed on Au(111) surface at T=141 K.

tated by dispersion interaction between alkyl chains and intermolecular hydrogen bonding among amino and carboxylic groups. Some amino substituents in this configuration were pointing further away from the surface and were not involved in hydrogen bonding. The strong COOH−based H−bonds together with complex multibody interaction stabilized this conformation at the relatively small densities considered

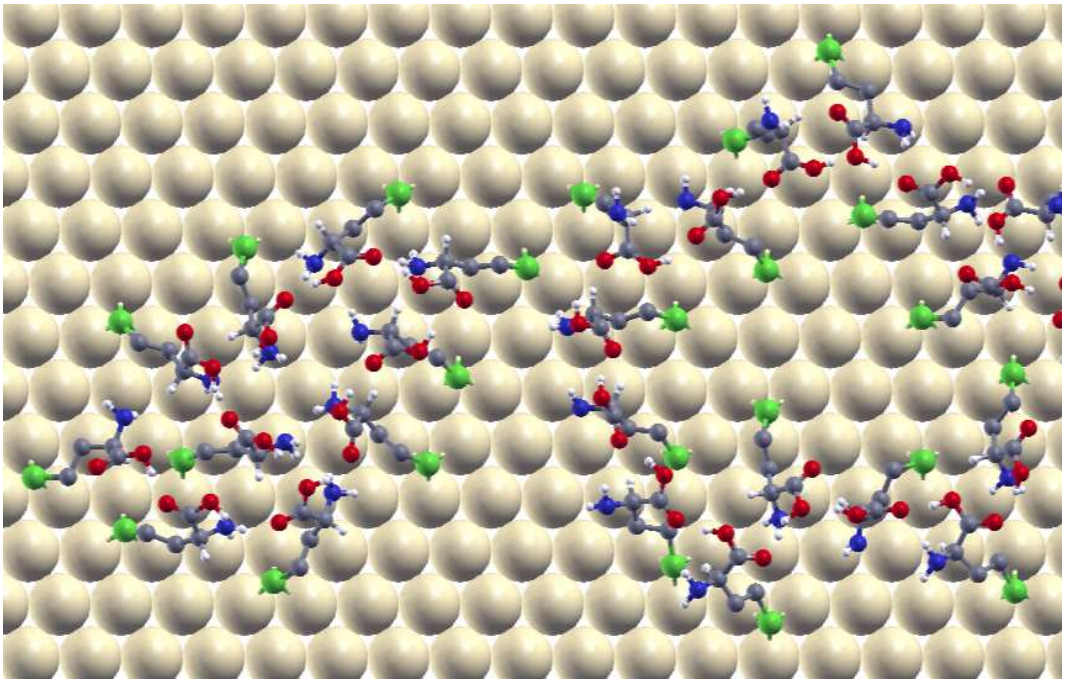

(a)

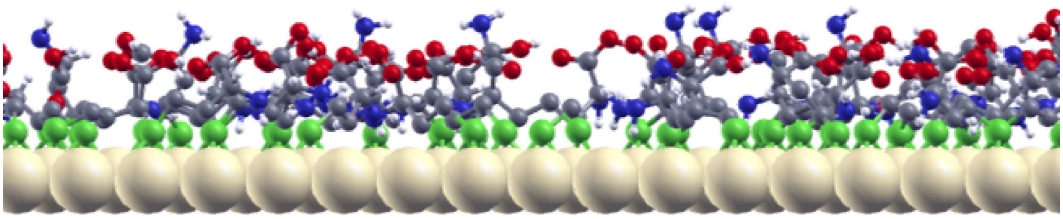

(b)

Figure 6.6: A simulation snapshot of D-homocysteine in thyil form adsorbed on Au(111) surface at T=296 K. The top (a) and side (b) views are presented.

here.

In the "parallel" configuration homocysteine molecules adsorbed more or less flat, with alkyl chain relatively parallel to the surface and amino groups pointing toward the surface. This conformation was the predominant binding geometry of the ad-

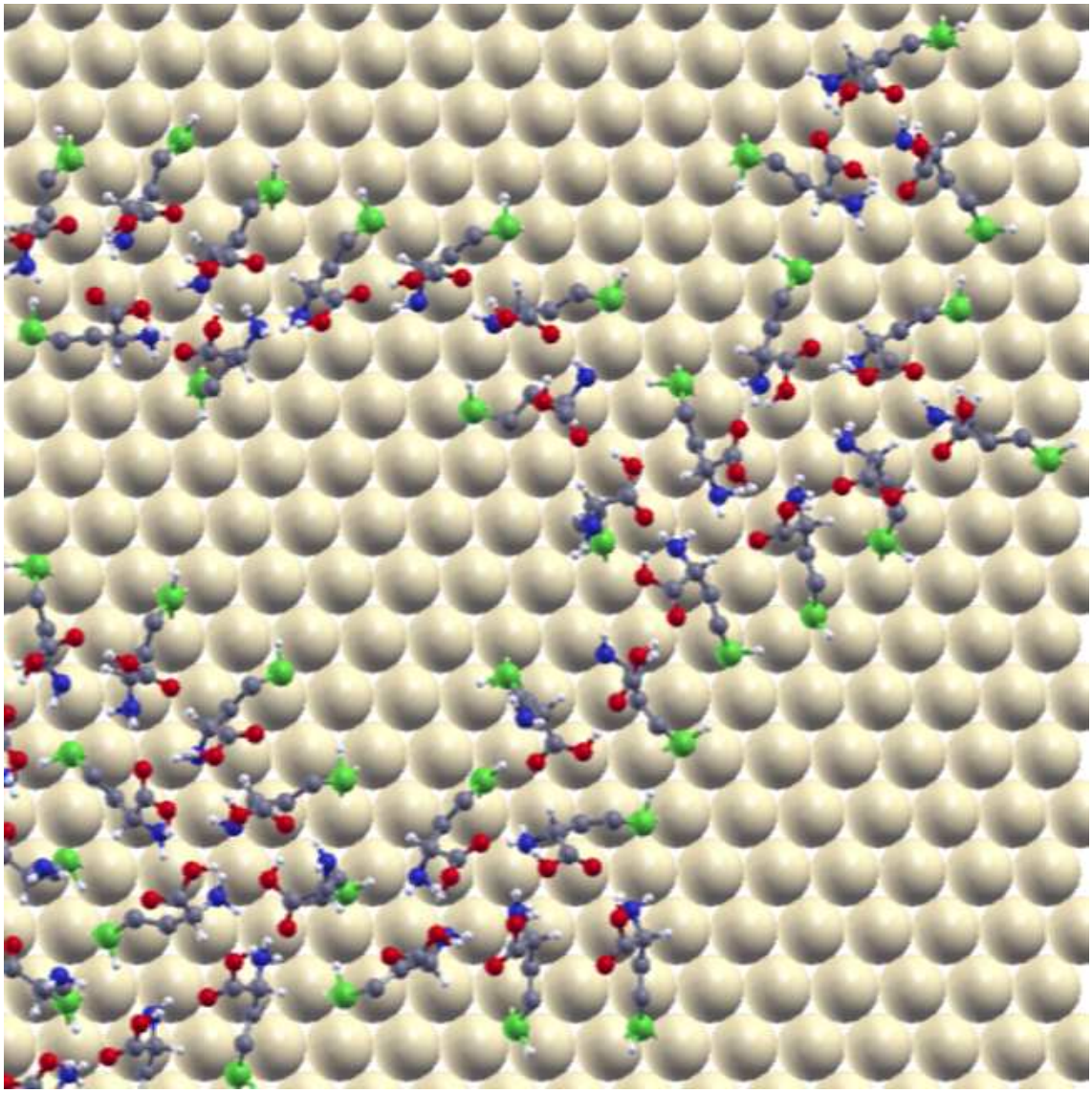

Figure 6.7: A simulation snapshot of D-homocysteine in thiol form adsorbed on Au(111) surface at T=296 K.

sorbed D-homocysteine especially at lower temperatures and led to larger footprint aggregates than the clusters formed by molecules that bound in a single point to the substrate and which were encountered more at higher temperatures. Our previous DFT studies on adsorption of up to three molecules of homocysteine on Au(111)

surface showed that flat binding geometry of homocysteine was energetically more stable than upright geometry.[158] However, in the multibody adsorption aggregates, the two configurations competed. Temperature effects on adsorption of homocysteine were similar to the adsorption of cysteine. At low temperatures the molecules mostly adsorbed in a planar conformation. The fraction of molecules in the upright conformation increased with the increase of the temperature, although there was a significantly larger fraction of upright homocysteine than upright cysteine at lower temperatures.

The intermolecular H−bonding encountered in extended systems considered here was similar to the H−binding in the trimer structures discussed in Chapter 5. The double hydrogen bonds between COOH groups formed in dimer structures could not be satisfied in the extended configurations, because in such configuration only two molecules were mainly involved in H−bonding. The molecules in the extended configurations established H−bonds with two neighbouring molecules through COOH groups and occasionally though NH_2 groups.

6.4 Extended systems of D-methionine

The methionine molecule had a methyl terminal group attached to the sulfur atom with the S−C bond slightly longer that the S−H bond, that allowed the sulfur to bind to a hollow site maximizing its gold neighbours. The methionine adsorbed on the surface in an upright conformation through sulfur atoms as well as parallel geometry through the sulfur, alkyl chain and nitrogen. The upright geometry was not seen for dimer and trimer adsorption on Au(111) even at highest temperatures. Geometries with molecular backbones close together were often seen at higher temperatures,

although the molecules were still in a parallel geometry (see Figure 6.8). In this

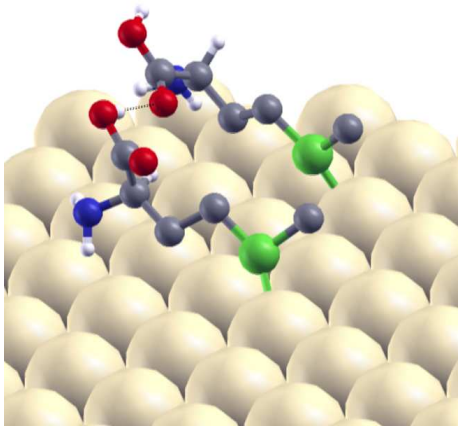

Figure 6.8: A simulation snapshot for like D-methionine dimer adsorbed on Au(111) surface at T=296 K.

configuration, the molecules maximized the dispersion interaction with the surface as well as with each other. DFT calculations found this dimer configuration energetically slightly less stable than the configuration in which double COOH−based H−bonds were formed (see for example Figure 5.5, Chapter 5). However, in the multibody system investigated here, the configuration presented in Figure 6.8 was a precursor in adsorption pattern formation (see Figure 6.9). The presence of other interacting molecules impacts the interaction between the two molecules and consequently may stabilize such pair configuration that are not necessarily the lowest in energy when studied isolated. Extended hydrogen bonded supramolecular rosette clusters and chain structures were formed upon adsorption of D-methionine onto Au (111). Fully upright molecules were not encountered in our study of adsorption of dimers and trimers, but they were occasionally seen in the extended systems. The stability of the optimal parallel geometry of the isolated dimers was overcome by the multibody interactions and consequently promoted the upright geometry.

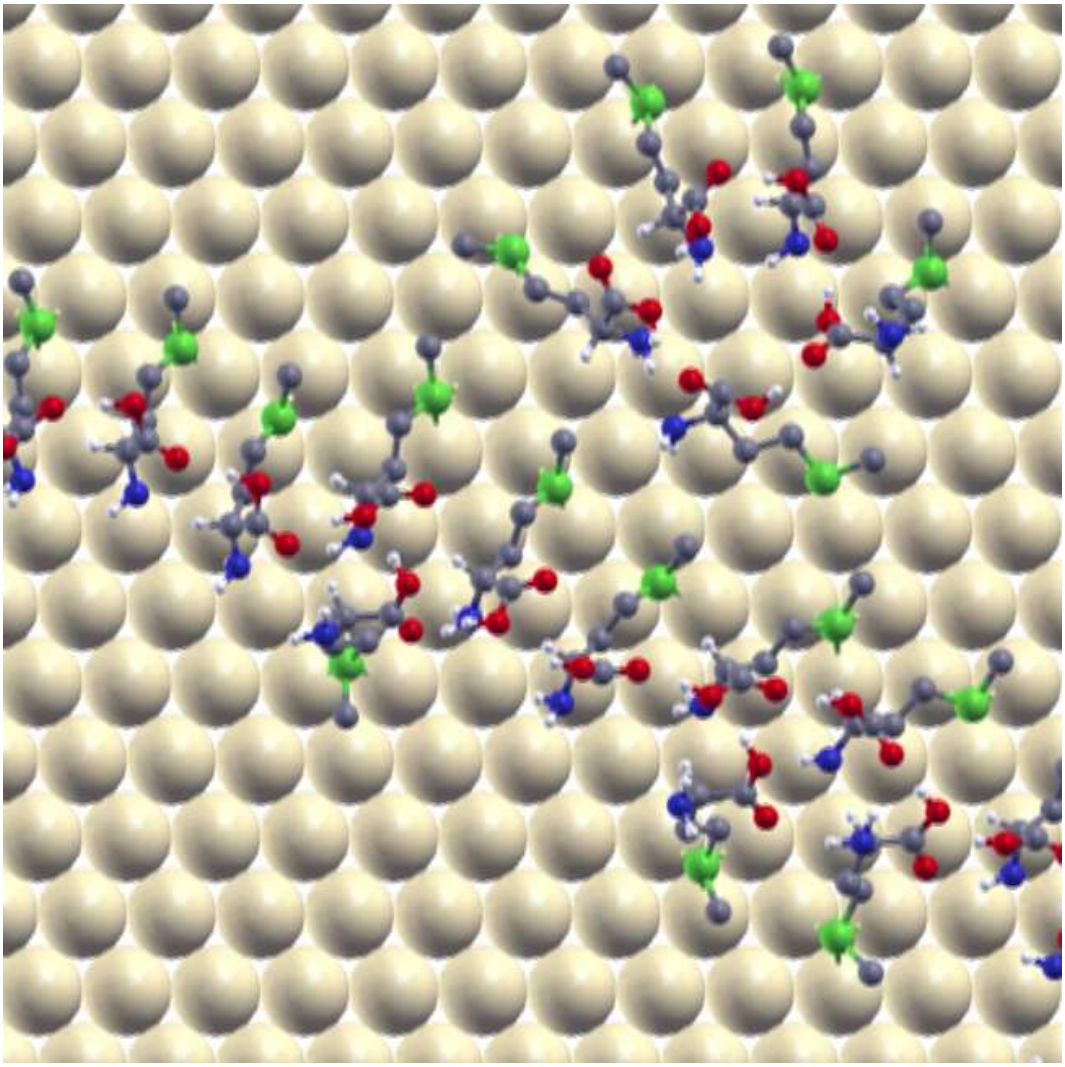

Figure 6.9: A simulation snapshot of neutral D-methionine adsorbed on Au(111) surface at T=296 K.

6.5 Racemic mixtures

Racemic mixtures of cysteine, homocysteine and methionine were also studied. The adsorption patterns were very similar to those formed by enantiopure compounds. Simulation snapshots of racemic cysteine and homocysteine in thyil forms are shown in Figures 6.10 and 6.11 (a). Neutral molecules as either thyils or thiols were in-

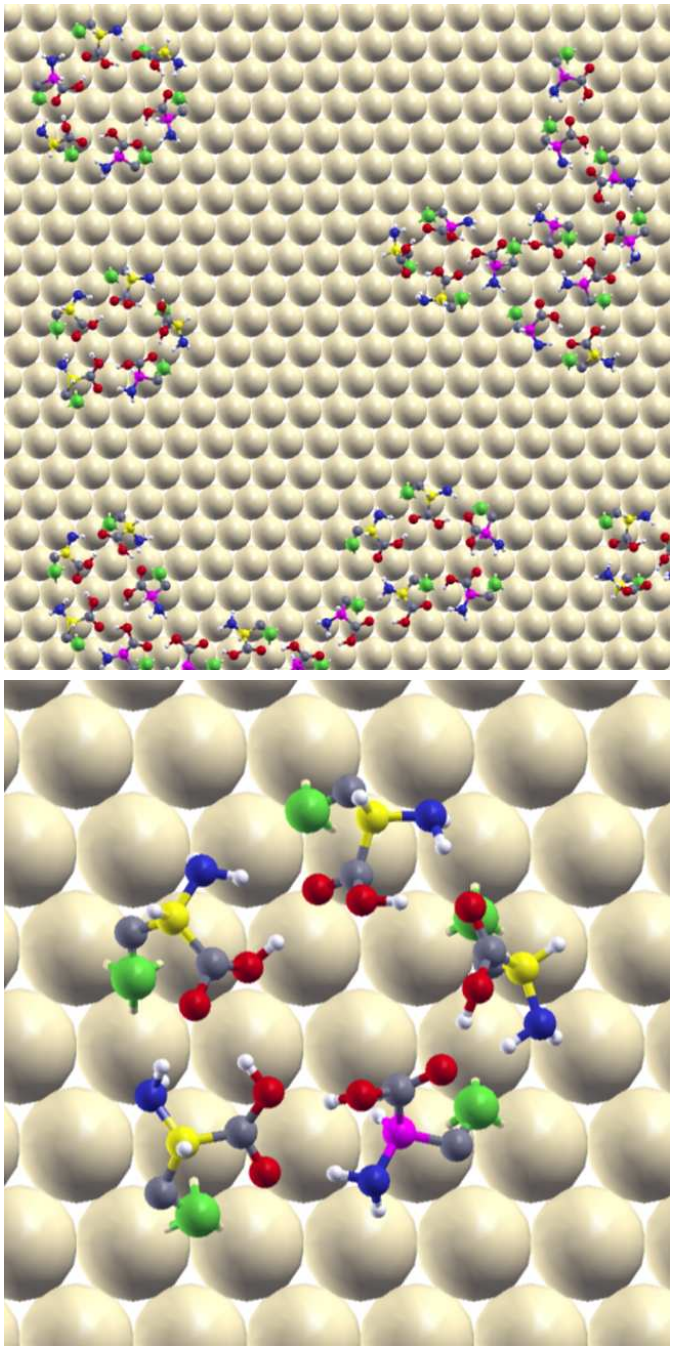

Figure 6.10: (a) A simulation snapshot of racemic neutral D-cysteine adsorbed on Au(111) surface at T=321 K. (b) Enantiomerically enriched rosette cluster. The cluster is a local detail from the snapshot shown in panel (a). Chiral carbon atoms in the two enantiomers are indicated in yellow and magenta, respectively.

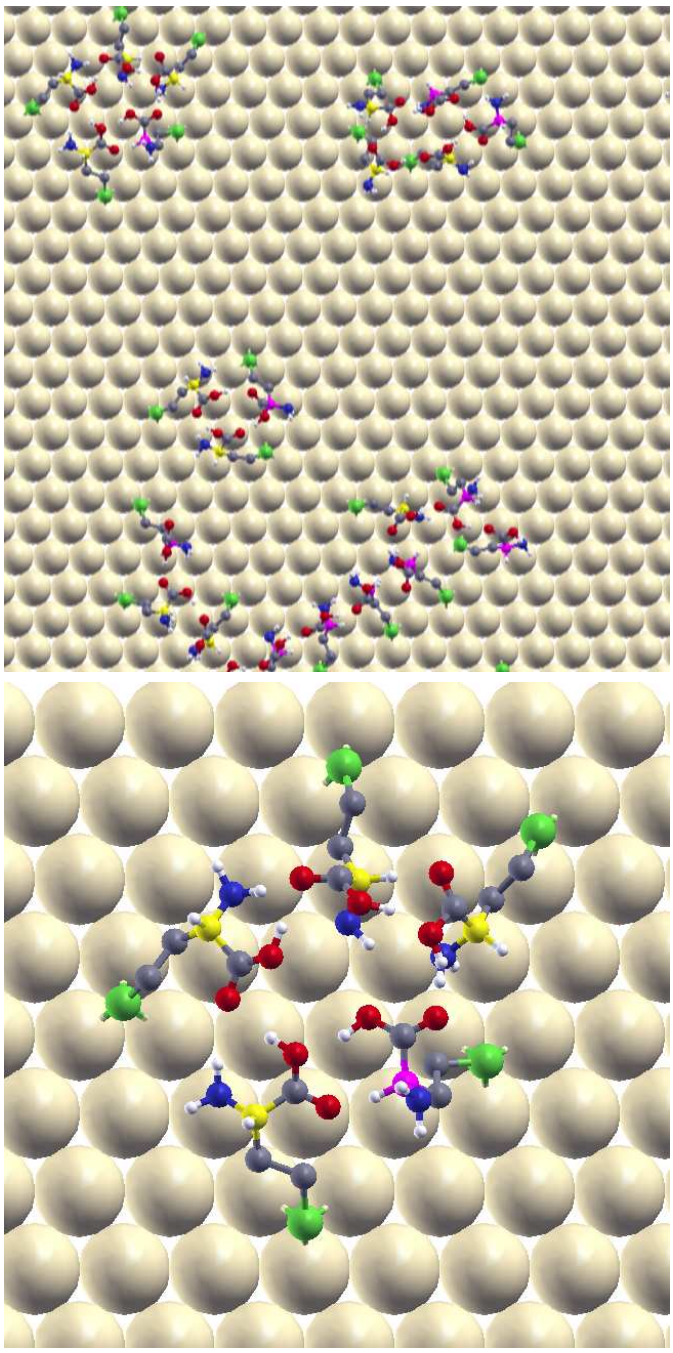

Figure 6.11: (a) A simulation snapshot of racemic neutral D-homocysteine adsorbed on Au(111) surface at T=277 K. (b) Enantiomerically enriched rosette cluster. The cluster is a local detail from the snapshot shown in panel (a). Chiral carbon atoms in the two enantiomer are indicated in yellow and magenta, respectively.

volved in rosette clusters and extended molecular chains. Hydrogen bonding between carboxyl and amino groups stabilized the adsorption assemblies. As can be seen in the simulation snapshots, enantiomerically enriched domains formed upon adsorption of neutral state racemic mixtures. Generally the molecules preferred to adsorb on the surface with nitrogen pointing towards the surface and hydrogen of the chiral atom pointing away from it. The enantiomer that was found in excess in a rosette cluster bound to the surface in the same way, with amino group pointing towards the surface and involved in H−bonding with a neighbouring COOH group (see Figure 6.10 (b)). In order to be part of the rosette cluster and participate in hydrogen bonding in the same way through both carboxyl and amino groups, the enantiomer of the opposite chirality adsorbs with H atom of the chiral carbon pointing towards the surface and amino group slightly pointing away from it. In this configuration, however, the amino group interacted less with the surface and often could not be involved in H−bonding either. The interplay between intermolecular hydrogen bonding and molecule-surface interaction (in particular due to relatively strong N−Au interaction), therefore, promoted the formation of homochiral or enantiomerically enriched clusters. Similar adsorption structures were seen for racemic methionine adsorbed onto Au(111).

6.6 Summary

We investigated several enantiopure and racemic sulfur-containing chiral amino acids and their self-assembly on Au(111) surface using PTMC method. These amino acids mainly attached to the surface through sulfur atoms and were involved in different supramolecular structures based on their binding modes and molecular states. Neutral molecules were involved in hydrogen-bonded rosette clusters as well as molecular

rows as a result of the interplay between surface - adsorbate and molecule-molecule interactions. Additional hydrogen bonding between edge molecules, with either carboxyl, amino or both groups involved slightly stabilized the micellar geometry over molecular chains. Homocysteine and methionine adsorbed in two conformations: an upright and "parallel" geometries. The latter dominated the adsorption patterns over a relatively large range of temperatures.

Chapter 7

Adsorption on Naturally Chiral Surfaces

Naturally chiral surfaces may exhibit enantiospecific properties upon adsorption of chiral molecules. In order to fully exploit the potential of these surfaces in enantioselective chemistry, we need to understand the adsorption mechanism at a molecular level. Chiral surfaces are energetically non-uniform and present surface atoms with different coordination numbers and thus different reactivity. Lowest coordinated metal atoms have been shown to have an important role in molecular adsorption and are generally preferred for binding.[70, 159] Force fields which describe the adsorbate-substrate interaction that accounts for uneven surface energy are therefore desired. Using a such force fields is particular important in the simulation of molecules that chemisorb on non-uniform surfaces. We used DFT calculations to quantify the coordination dependence of surface-molecule interaction and develop corresponding force field parameters. Simulation results about correlation between coordination number and binding energy of small organic molecules are discussed in Section 7.2.

Chiral adsorption of toy models, as well as adsorption of cysteine amino acid on naturally chiral surfaces was studied using PTMC simulations that included coordination specific surface-adsorbate interaction and are described in Section 7.3 and 7.4, respectively.

7.1 Chiral surface models

The surface models used in this study were representative for chiral substrates with ideal structures. The real structures of the chiral metal surfaces differ from those of the ideal termination of the bulk crystal.[44, 47, 104] The real structures are generally subject to thermal roughening that involves the diffusion of atoms along the step edges. The diffusion of the atoms causes the coalescence of kinks, and consequently induces the formation of non-ideal kink structures at the intersections of longer step edges. However, despite the structure differences, the real surface structure maintains its chiral terrace-step-kink structure and the net chirality of the ideal surface structure.[85, 92, 93] Thus, using the ideal structure in the simulations is expected not to have a significant impact on adsorption pattern formation.

Such surfaces as copper, platinum, silver and gold with (643) and (531) geometry have been frequently used in experimental and theoretical studies. The (643) chiral surface has a structure formed of well defined (111) terraces, (100) steps, and (110) kinks. The (531) surface, on the other hand, has the same three low miller index microfacets, but which cannot be classified as terraces, steps, or kinks because they all are of the same size.[104] The ideal structures of (643) and (531) surfaces and the corresponding coordination numbers of the surface atoms are presented in Figure 7.1. As seen in the figure, surface atoms at the kink and edge step sites exhibit lower co-

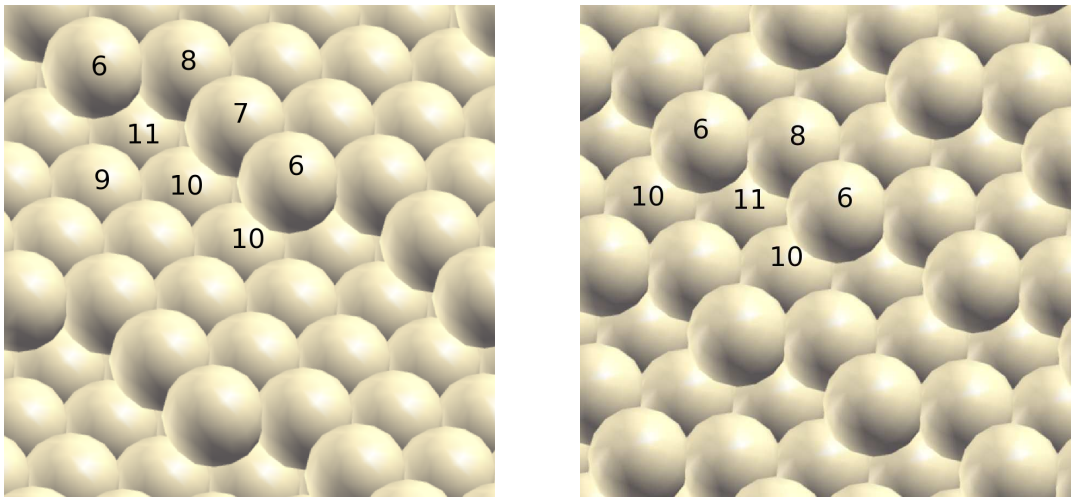

Figure 7.1: Models of the ideally terminated (643) (a) and (531) (b) chiral surfaces and the corresponding coordination numbers of surface atoms.

ordination numbers. The coordination number (CN) of a surface atom represents the number of its nearest neighbours. The bulk coordination number of a face-centered cubic structure is 12, whereas the surface coordination number is always lower.

Based on surface coordination number, the adsorption sites of a chiral surface, in order of energetic preference, are kink, step edge, and terrace sites. The outer kink atoms of the (643) and (531) surfaces have the lowest coordination number 6 and are consequently the most reactive sites on the surface. Inner kink atoms have coordination number 8, which are relatively more reactive than a terrace atoms with coordination numbers 9, 10 and 11. Step atoms of the (643) surface have coordination number 7 and thus are generally preferred binding sites. However, terrace sites that consist of (111) facets of different width may better accommodate the adsorbate molecules or the adsorption assemblies than step or kink sites. Thus, there is always a balance between the energetics of the surface and the steric effects that impact the

self-assembly process which is yet to be understood.

The two chiral surfaces that were investigated here have distinct geometries. The (643) surface has wider terraces and longer steps, whereas the (531) surface presents a higher density of kink sites (see Figure 7.1). Nevertheless, experimental studies of the adsorption of (R)-3-methylcyclohexanone on (643) and (531) chiral surfaces has been shown to be quite similar in spite of distinct differences between their ideal surface structures.[104] Thus, although the (531) surfaces has a greater density of highly reactive chiral kinks, it was not necessarily more enantiospecific than the (643) surface for the adsorption of R-3MCHO. For a better understanding of enantiospecificity of naturally chiral surfaces, a larger number of related systems are needed to be investigated.

7.2 Coordination dependent force field parameters

The sulfur containing amino acids described in Chapter 5 bound mainly to gold surface trough sulfur and nitrogen atoms. Small organic molecules as methylthiol, methylamine and dimethyl sulfide (see Figure 7.2) present similar binding to the gold and represent simpler models that may be used in quantum calculations of interaction energies. The binding of these model molecules to different coordinated Au atoms

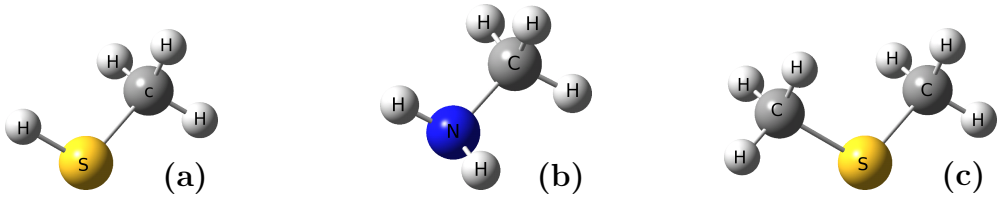

Figure 7.2: Small organic molecules that were investigated by Ting et al. in the study of coordination dependent binding to gold: methylthiol (a), methylamine (b) and dimethyl sulfide (c)

was investigated in our group by Elvis Ting using DFT calculations as implemented in the SIESTA code and briefly described in Chapter 5.

The gold surface used for the calculations was modeled using a 20-atom Au (643) slab with no periodic boundary conditions. The gold atoms were kept frozen during the optimization process. Binding energies were calculated using equation 5.2. The correlation between the coordination number of surface atoms and binding energies is shown in Table 7.1.

Table 7.1: Coordination specific binding energies

Coordination number[1]	E_{CH_3SH} (eV)	$E_{CH_3NH_2}$ (eV)	$E_{(CH_3)_2S}$ (eV)
6	0.9	0.8	0.9
7	0.6	0.6	0.7
8	0.4	0.4	0.5
9	0.2	0.3	0.3

[1]Coordination number represents the number of nearest neighbours of a surface gold atom

Surface atoms with coordination number 6 that belong to outer kink sites (see Figure 7.1) were found to be about four times more reactive than terrace surface atoms with coordination number 9. Adsorption is therefore much stronger on chiral surfaces that present lower coordination number atoms than on flat surfaces as it is Au (111) that has only surface atoms with coordination 9.

The calculated binding energies presented in Table 7.1 include besides interaction of central atom (sulfur and nitrogen) with the gold surface, dispersion interaction between methyl groups and hydrogen atoms attached to it and the substrate. The contribution of dispersion interaction is, however, much lower relative to the strong binding of sulfur and nitrogen, and thus the data presented in the table represents a relatively good approximation for the interaction of the central atom and the sub-

strate. In particular, we developed force field parameters that described a comparative adsorption strength specific to distinct coordination numbers. According to Table 7.1, the interaction between the adsorbate and the surface atoms with a coordination number 6 was described by an energy parameter which was around two times larger than the energy parameter between the adsorbate and the 8-coordinated surface atoms. The least reactive surface atoms with coordination number 9 and higher were described by the same attraction strength.

7.3 Chiral adsorption of model molecules

Our study about surface effects of flat achiral surfaces in chiral adsorption, described in Chapter 3, showed that the adsorbed patterns and geometries of molecules A were largely unaffected by surface attraction or layout. Chiral resolution was achieved by restricting the molecules A to evolve in two dimensions, while the surface-molecule interactions had a lower impact on the quality of separation. Chiral surfaces, however, exhibit kink-edge-terrace structures that add complexity to the two-dimensional chiral adsorption. We investigated the self-assembly of model molecules A on two chiral surfaces (643) and (531), respectively, by considering different surface atom sizes, which implies different layouts as well as different surface attraction. Smaller surface atoms present a higher density of atoms per unit area and thus induce a stronger surface attraction.

Racemic mixtures, composed of 100 model molecules, adsorbed on the (643) and (531) chiral surfaces were equilibrated using PTMC method in simulation box with no periodic boundary conditions. The size of the simulation box is large enough that it does not impact the density of the resulting structures. Intermolecular interactions

are described with pairwise atom-based Lennard-Jones and electrostatic potentials described by equation 2.7. Surface-molecule interactions are adjusted for specific coordination number of surface atoms. The model molecules considered here are described in detail in Chapter 3.1 and shown in Figure 3.1, respectively. Briefly, the molecule presents one chiral center that incorporates partial charges as well as the spacer group. Asymmetry is created by the small strongly attractive tailgroup and the bulky less attractive headgroup.

Chiral separation was achieved upon adsorption of model molecules A on achiral solid substrates. The molecules presented intermolecular chiral recognition when adsorbed on naturally chiral surfaces as well and were involved in formation of homochiral rosette clusters at low and intermediate temperatures. A simulation snapshot of racemic mixture of molecule A adsorbed on a (643) chiral surface is shown in Figure 7.3. The rosette structures in the figure resembled the structures obtained on flat achiral surfaces. As previously, the final geometries were not significantly affected by the different sizes of the surface atoms. On the chiral surfaces considered here ($\sigma_s^* >= 2$), hetereochiral double chains were often not observed. The fraction of molecules that were involved in unlike structures was bellow 1%, whereas up to 90% of molecules were involved in homochiral rosette clusters, as seen on flat surfaces. Moreover, the average sizes of the clusters formed here, were similar to the averages obtained on flat surfaces with $\sigma_s^*=2$. Around 50% of molecules were involved in homochiral five-molecules clusters at low and intermediate temperatures. The adsorption patterns of molecules A were governed overall by intermolecular interactions. Surface-molecule interactions decided the locations of the clusters, but did little influence their formation. The rosettes were formed mostly at kink sites and closer to the stepped edges of the surface. Such sites were preferred for binding due to the presence of the lowest

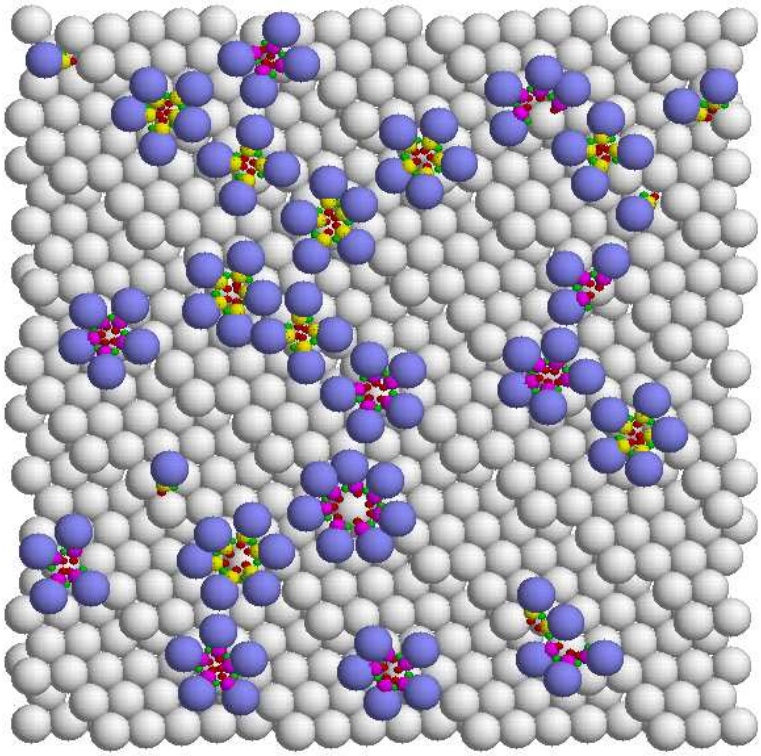

Figure 7.3: A simulation snapshot of molecules A adsorbed onto (643) chiral surface with σ_s^*=2 at T*=1.81. Although identical, the chiral centers in the two enantiomers are colored in yellow and magenta, respectively.

coordinated surface atoms (coordination number 6).

A larger fraction of single molecules were seen on chiral (643) surface at lower temperatures. Single molecules were adsorbed near kink sites and were stabilized there due to strong surface attraction. The interaction between single molecule and kink (including edge) sites was competing with the adherence of the former to an existing cluster. At such adsorption sites, single molecules established lateral interactions with surface atoms with lower coordination number from the steps and kinks, as well as with underlying terrace surface atoms. On flat surfaces single molecules were observed generally at relatively high temperatures.

When the surface atoms were larger (Figure 7.4), the molecules formed a rosette

cluster on top of the most reactive surface atom (outer kink atom, CN=6). A second

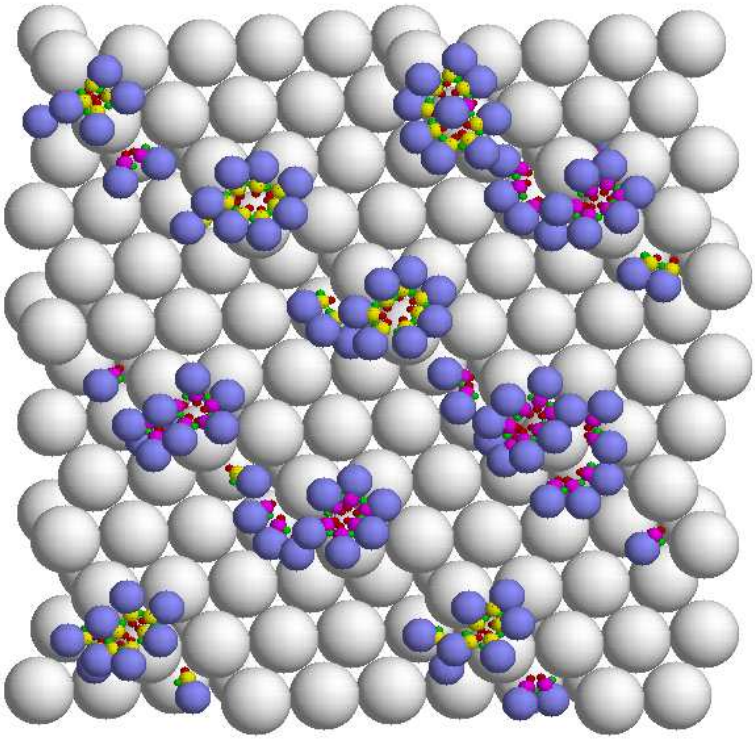

Figure 7.4: A simulation snapshot of molecules A adsorbed onto (643) chiral surface with σ_s^*=4 at T*=1.81. Although identical, the chiral centers in the two enantiomers are colored in yellow and magenta, respectively.

structure was formed on the adjacent lower terrace, around the bottom of the outer kink atom. The outer kink atom could accommodate more than one structure due to its large size and it was preferred for binding because of its strong reactivity. Molecules at the bottom (on the lower terrace) adsorbed with the strongly attractive tailgroup to the kinks and edges, whereas bulky less attractive headgroup were interacting mostly with the surface atoms corresponding to the terrace sites. On smaller atom-surface (Figure 7.3), the adjacent terraces were separated by a step edge of a lower height (one atom height, of a smaller size), and the lowest coordinated gold atom (outer

kink) could not be involved in more than one structure because of the arising steric effects. The clusters formed on adjacent terraces sharing the same outer kink atom would have been too close together.

The rosette structure formed on top of the outer kink atom had the strong attractive tail groups gathered together on top of the 6-coordinated kink atom or at a bridge site between two lowest coordinated surface atoms (CN 6 and 7, see for example Figure 7.1). Smaller size rosettes (up to 6 molecules) adsorbed generally on one terrace, whereas larger size rosettes extended on the two adjacent terraces around the outer kink atom. Rosette clusters slightly distorted towards an elliptical geometry with the tailgroups in the bridge or off-bridge positions were often encountered on surface with larger atoms. The grooves between surface atoms were large enough to accommodate such structures. Moreover, the bridge sites were attractive adsorption sites and consequently preferred for binding because the molecules here bound to the two lowest coordinated surface atoms. All the adsorption structures formed on chiral (643) surface were homochiral.

The adsorption features of naturally chiral (531) surface were also investigated here. Simulation snapshots of molecules A adsorbed on chiral (531) surfaces are shown in Figure 7.5. Two atomic sizes of the underlying surface are presented. A large fraction of single molecules was encountered at low and intermediate temperatures, especially on surface with lower size atoms (Figure 7.5 (a)). The latter presented reactive adsorption sites that could accommodate single molecules in such a way that the molecule gained direct binding from two lowest coordinated surface atoms, that corresponded either to the same terrace or to the nearby lower terrace. As opposed to (643) surface described by the surface atoms of similar size that accommodated the structures generally along the steps (Figure 7.3), the structures on (531) surface

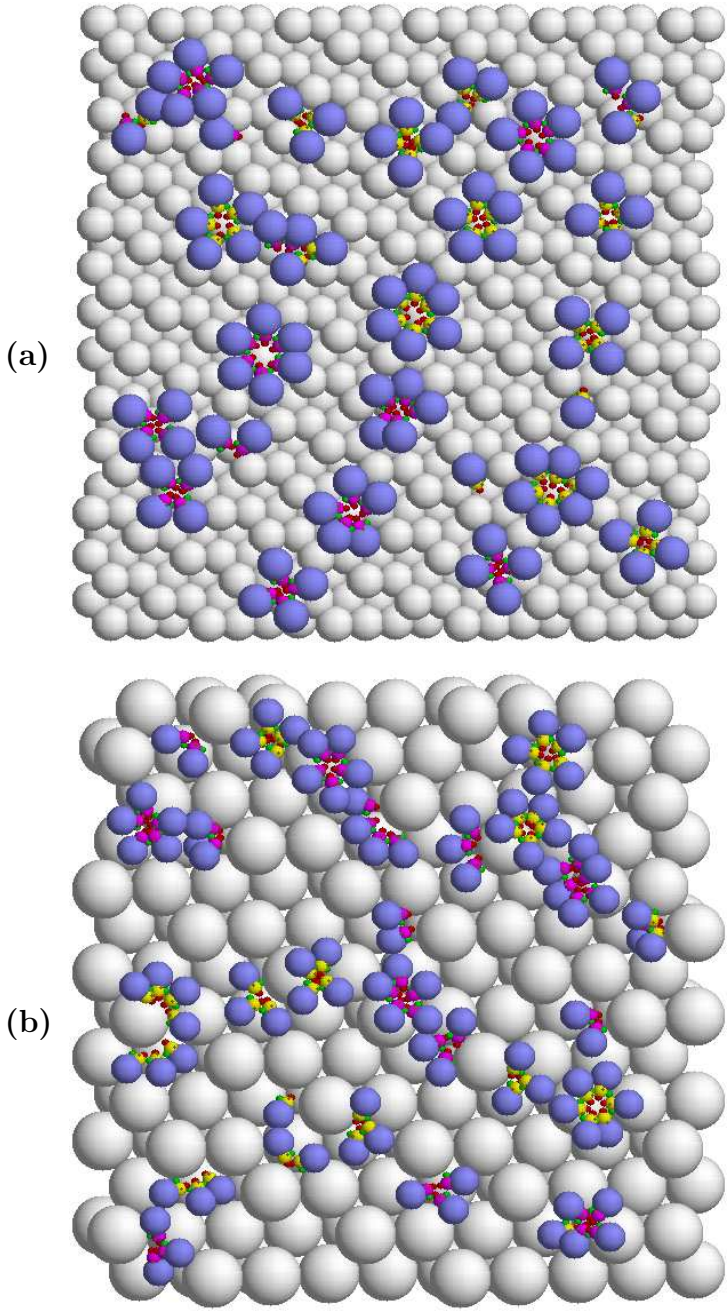

Figure 7.5: A simulation snapshot of molecules A adsorbed onto chiral (531) surface with σ_s^*=2 (a) and 4 (b) at T*=2. Although identical, the chiral centers in the two enantiomers are colored in yellow and magenta, respectively.

were more evenly distributed. The (531) surface presented a larger and uniform distribution of kinks and when characterized by small size surface atoms it could be seen as a more or less horizontal uniform surface with an enhanced roughness and reactivity.

Larger atomic size of the (531) surface presented relatively similar adsorption features as correspondent (643) surface. The lowest coordinated atom was involved as before in formation of homochiral structures from both upper and lower terraces. The structures that belonged to neighbouring terraces were either of the same or different chirality. Thus, the overall adsorption patterns formed around low coordinated atoms were often heterochiral, unlike the structures formed on surface with smaller atomic sizes that were generally homochiral. The temperature dependence of the fraction molecules involved in like local structures (F_l) formed on (531) surface is shown in Figure 7.6. As seen in the Figure, the fraction of molecules that had exclusively like neighbours decreased with increasing the size of the surface atoms. The clusters formed on the surface with σ_s^*=4 were more disaggregated then the structures formed on the surface with smaller atoms (see Figure 7.5), which resulted in a lower overall F_l value. Also, the clusters that belonged to adjacent terraces were too close to each other, and thus the nearest neighbours of a molecule involved in a homochiral clusters might belong to nearby clusters that were or were not of the same chirality.

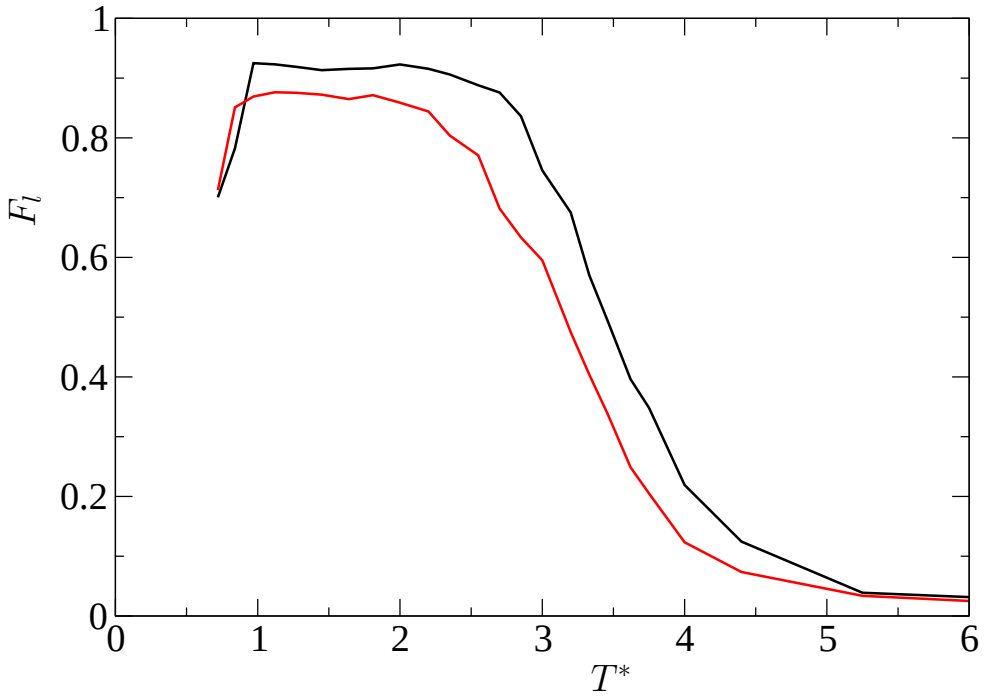

Figure 7.6: Temperature dependence of the fraction of the total number of molecules A involved in like local structures. Chiral (531) surfaces with σ_s^*=2 (black line) and 4 (red line) were considered.

7.4 Adsorption of cysteine on chiral Au(643)

Cysteine was previously shown to adsorb enantioselectively on chiral gold surfaces. A recent DFT study on adsorption of cysteine on the Au (321) surface [80] showed that cysteine molecules adsorbed much stronger on the chiral Au(321) than on the non-chiral Au(111) and discriminated between the two enantiomers of the chiral surface. At low coverage, the adsorption of L-cysteine was energetically favored on the Au(321)^S surface than the adsorption of D-cysteine with roughly 0.4 eV energy difference. A similar trend has been observed by Greber et al. [70] for cysteine adsorption on Au(17 11 9)^S. Two distinct adsorption geometries were found experimentally for

D- and L-cysteine on Au (17 11 9)^S surface. DFT calculations confirmed the experimental structures and predicted that D-cysteine bound 0.14 eV stronger to S kinks of the gold surface than it did L-cysteine.

7.4.1 Simulation details

Molecular flexibility is an important feature that must be considered in particular, in studying the enantiospecific adsorption. In order to present enantiospecific interaction, the molecules have to be able to change their equilibrium conformation and interact efficiently with the uneven sites of the surface, such as kinks and steps. Generally the energy associated with molecular deformation is overcome by the strong adsorption giving rise to stable adsorption patterns. Often, a much stronger interaction with the substrate is exhibited by an enantiomer of a chiral molecule, which means that an adsorption site can be a better fit for one enantiomer than for the other. The surface in this case discriminates between two mirror images of a molecule and thus exhibits enantioselective interaction.

We investigate the adsorption of enantiopure and racemic cysteine on chiral Au(643) surfaces using PTMC simulations. The coordination number specific surface-adsorbate interaction, as well as the molecular flexibility were considered in this study. Implementing molecular flexibility increased significantly the computational cost of our simulations. Lennard-Jones energy parameters for cysteine-gold interaction shown in Table 7.2 are specific for gold atoms with coordination number 9 and higher (ϵ_9). Lower coordinated surface atoms were described by a stronger interaction. The energy parameters from Table 7.2 were appropriately adjusted for the chiral surface

Table 7.2: Lennard-Jones energy parameters for cysteine-gold[1] interaction.

Pair	ϵ(kJ/mol)
S−Au [2]	19.14
N−Au	4.760
C−Au	0.270
O−Au	0.202
H−Au	0.173

[1] Gold atoms with coordination numbers 9, 10 and 11
[2] An energy parameter of ϵ_{S-Au}=9.57 was used to describe the interaction of uncleaved SH groups to gold atoms

considered here, according to equation 7.1 :

$$\epsilon_{CN} = \epsilon_9 \cdot f_{CN}, \tag{7.1}$$

where ϵ_{CN} is the adjusted Lennard Jones parameters corresponding to a specific coordination number (CN) = 6, 7 or 8, and f_{CN} are the associated energy factors that are included in Table 7.3. For example, the interaction between nitrogen and an

Table 7.3: Coordination specific energy factors

Coordination number	Energy factor (f)
6	4
7	3
8	2
9	1

8-coordinated gold atom was described by the energy parameter of $\epsilon_{N-Au} = 2 \times 4.76$ kJ/mol = 9.52 kJ/mol, in which 2 is the energy factor associated with CN=8 and 4.76 kJ/mol is the energy parameter that describes the interaction between nitrogen and a gold atom with coordination number 9 or higher (Table 7.2).

7.4.2 Results and discussion

Adsorption patterns are strongly influenced by the molecular state of the adsorbate. Here, we considered the adsorption of enantiomerically pure and racemic mixtures of neutral cysteine in thyil form on chiral Au(643) surface. The molecules, as expected, adsorbed preferentially to the kink sites and stepped edges. Simulation snapshots of neutral cysteine molecules of same chirality adsorbed on Au(643) surface are shown in Figure 7.7.

Neutral cysteine molecules formed hydrogen bonded molecular rows and small rosette clusters as seen on Au(111) surface. The molecules bound to the surface mostly through thyil group. Outer kink atoms with lowest coordination number were preferred for binding, especially with the sulfur atom. Rosette structures were formed with sulfur located around the same outer kink, in which molecules interacted with the kink site and edges, as well as vicinal molecules. Structures in which sulfur bound to neighbouring kinks were also encountered. In the latter, the molecules adsorbed flatter on the surface, interacting with the surface terrace as well as forming intermolecular H−bonding. Rosette clusters encountered here were generally smaller than those previously seen on Au(111) surface. The preferred binding sites of chiral surface were not evenly distributed along the surface, which prevented the formation of larger clusters. Since the molecules bound strongly to the kinks through thyil groups, the sulfur location influenced the adsorption structures. Up to four kink sites were seen to be involved in a rosette cluster conformation. Consequently, small rosette clusters of three and four neutral molecules of cysteine were mainly encountered. Similar structures formed at lower temperatures (see for example Figure 7.8).

As seen previously on Au(111) surface, the most common adsorbed molecular geometry of cysteine at low and intermediate temperatures was the configuration

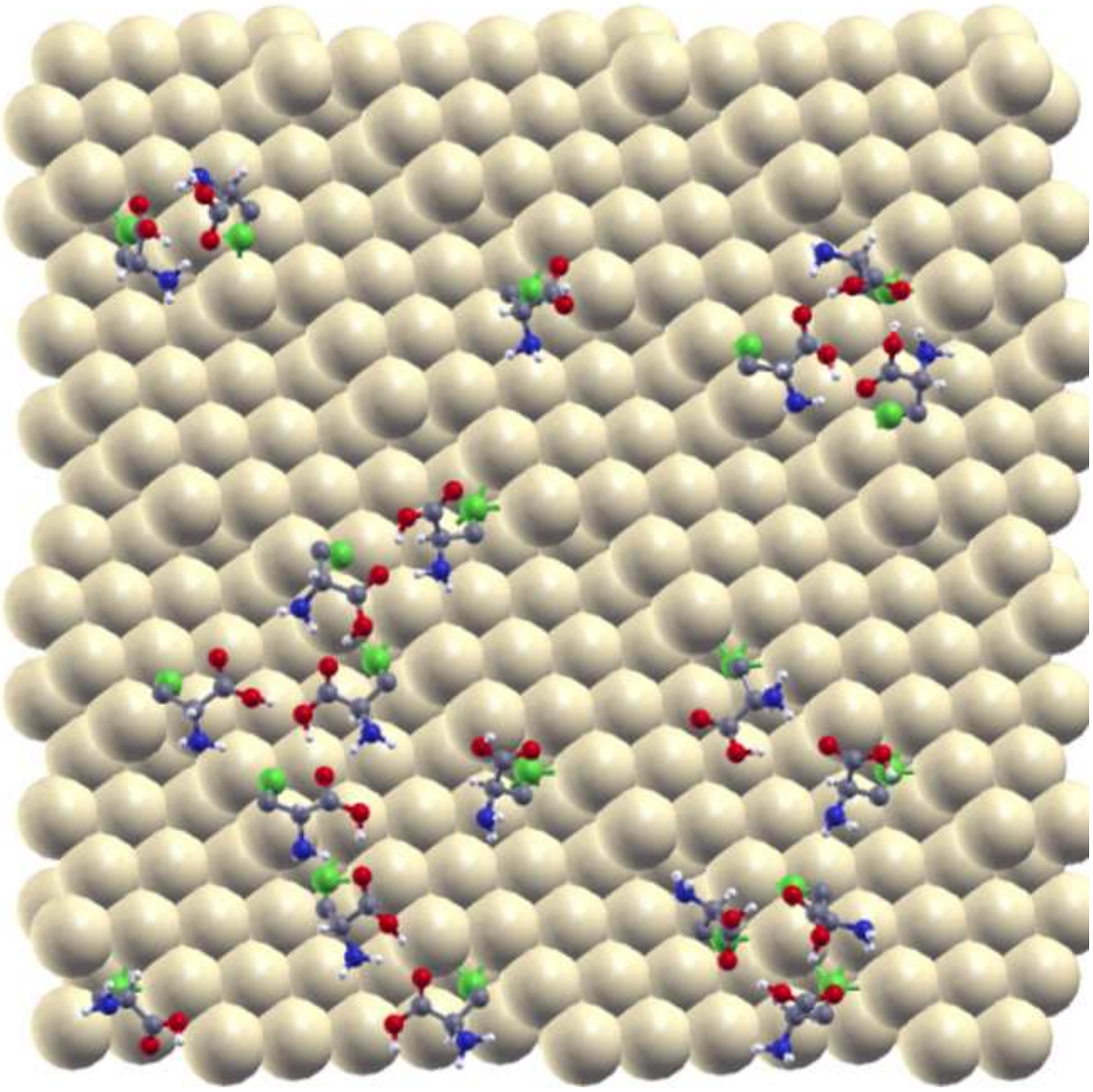

Figure 7.7: A simulation snapshot of enantiomerically pure system of neutral D-cysteine adsorbed on Au(643) surface at T=296 K.

in which the molecules bound to the surface through sulfur at a hollow site, with the amino group pointing towards the surface and COOH group generally desorbed and involved in H−bonding. At higher temperatures such geometries were competing with the upright geometry in which amino groups desorbed and pointed away

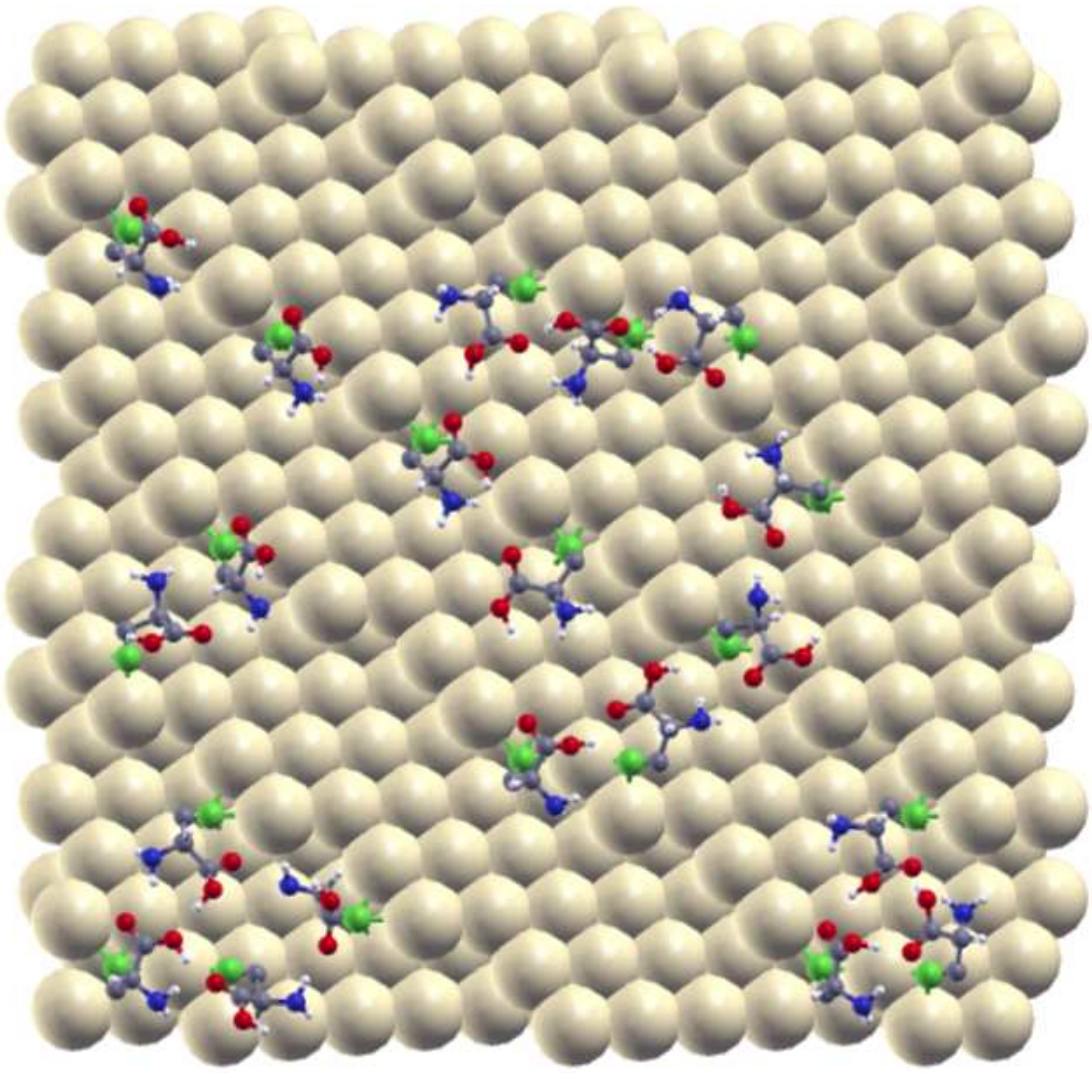

Figure 7.8: A simulation snapshot of enantiomerically pure system of neutral D-cysteine adsorbed on Au(643) surface at T=160 K.

from the substrate. The molecules were generally dispersed at higher temperatures, with only few involved in supramolecular structures. Accordingly, the intermolecular hydrogen−bonding was less preserved at high temperatures.

Racemic mixtures were also considered in our study. A simulation snapshot is

shown in Figure 7.9. Small rosette clusters and molecular chains of neutral cysteine

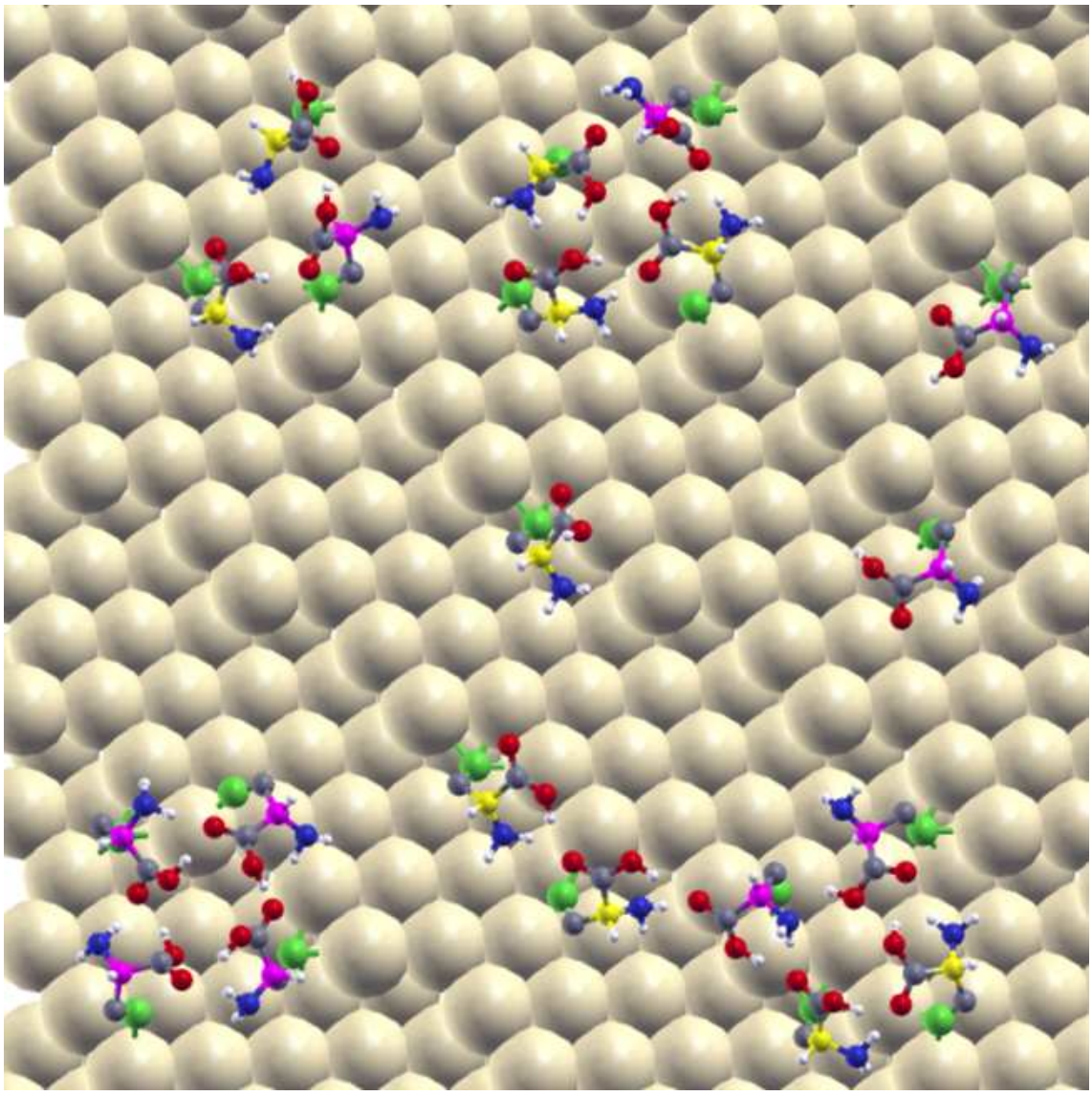

Figure 7.9: A simulation snapshot of racemic systems of neutral D-cysteine adsorbed on Au(643) surface at T=321 K. Although identical, the chiral centers in the two enantiomers are colored in yellow and magenta, respectively.

molecules were encountered, however, there was a large fraction of single molecules adsorbed to the kink and edge sites. Less assemblies were formed on the chiral

Au(643) surface considered here than on less reactive Au(111) surface. On chiral surfaces intermolecular interaction competed with stronger molecule-surface interaction, resulting in a smaller number of aggregates. The fact that less molecules were involved in self-assembly process, could be also due to trapping in very stable local minima on the highly attractive surfaces that presented complicated potential energy surfaces. Longer simulations runs might provide slightly different outcomes.

As seen in the Figure 7.9 and previously on Au(111) surface, cysteine molecules were involved in homochiral and enantiomerically enriched rosette clusters. The interplay between the strong intermolecular H−bonding in which both carboxylic and amino groups were involved, relatively strong interaction of amino group with the gold surface and steric repulsion between the H of the chiral atom and the surface led to preferential formation of like clusters.

Adsorption on complex heterochiral surfaces. Naturally chiral surfaces exist as chiral molecules in two enantiomeric forms. A complex surface that contain both mirror images (S and R) of a chiral surface was considered in our study (see Figure 7.10, for example). The surfaces were locally homochiral, and were assembled by joining together a side with R stereochemical designation and one with the S chirality. A preferential interaction of the chiral surface with the adsorbate enantiomers would be reflected in the agglomeration of one type of enantiomers on the preferred half of the surface. Enantiospecific interaction would lead to chiral segregation in the racemic mixture of the adsorbate. As the simulated joint surface pieces do not bind seamlessly, we rejected moves that placed molecules in a σ_s region around the surface middle boundary.

We investigated enantiopure and racemic systems of cysteine on $\mathrm{Au}(643)^{R\&S}$ surface. We try to learn how the molecules bind to the two enantiomers of the chiral

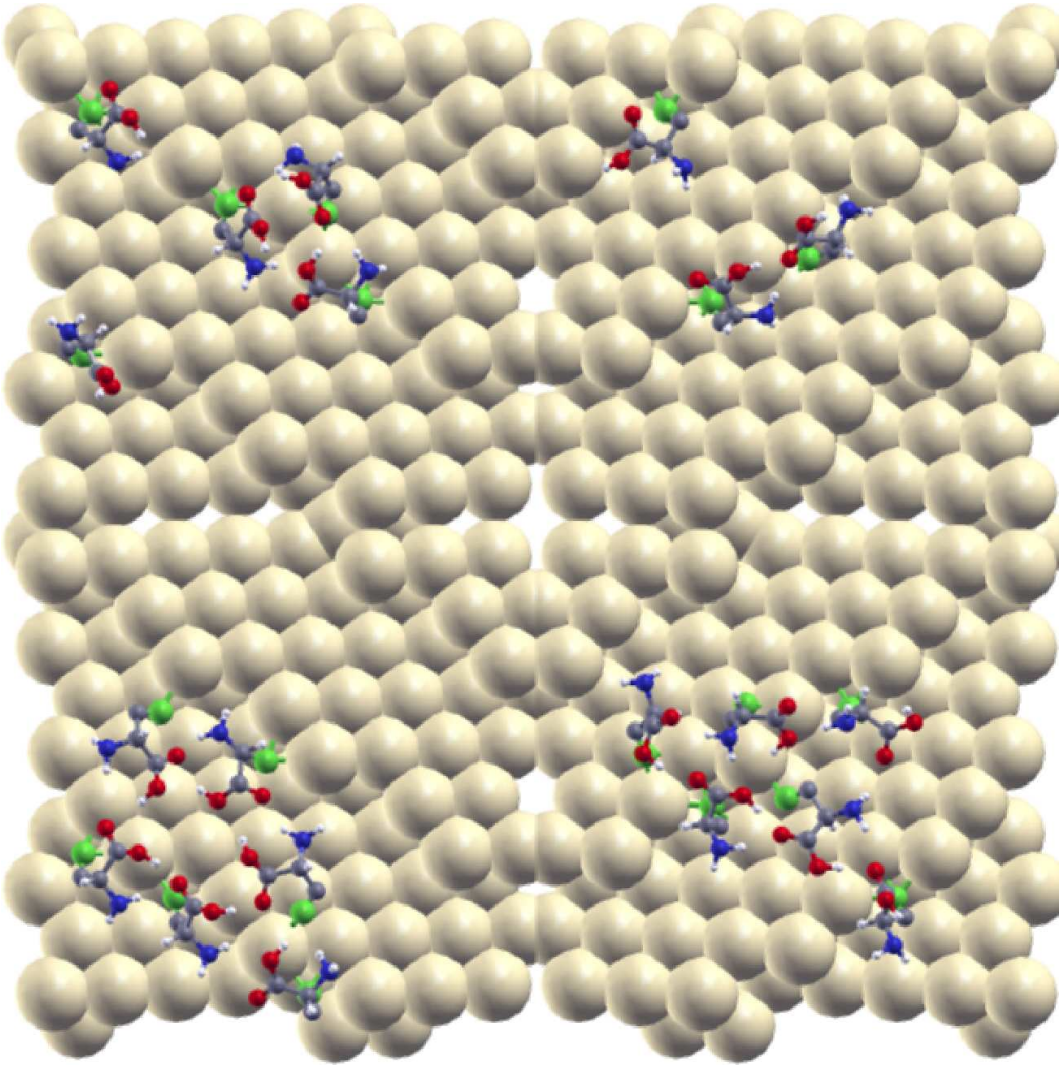

Figure 7.10: A simulation snapshot of enantiomerically pure system of neutral D-cysteine adsorbed on Au(643)$^{R\&S}$ surface at T=296 K.

surface and if there are enantiospecific differences in their adsorption geometry. Simulation snapshots of neutral cysteine are shown in Figure 7.10. The molecules adsorbed similarly on surfaces with different chirality. Rosette structures, molecular rows and single molecules were encountered on the whole surface, regardless of its local chirality.

Racemic mixtures adsorbed on Au(643)$^{R\&S}$ surfaces are shown in Figures 7.11. The heterochiral surface investigated here did not induce chiral segregation in the

racemic mixtures. The molecules did not discriminate between distinct surface chirality and bound more or less equally to both sides of the surface. However, as seen

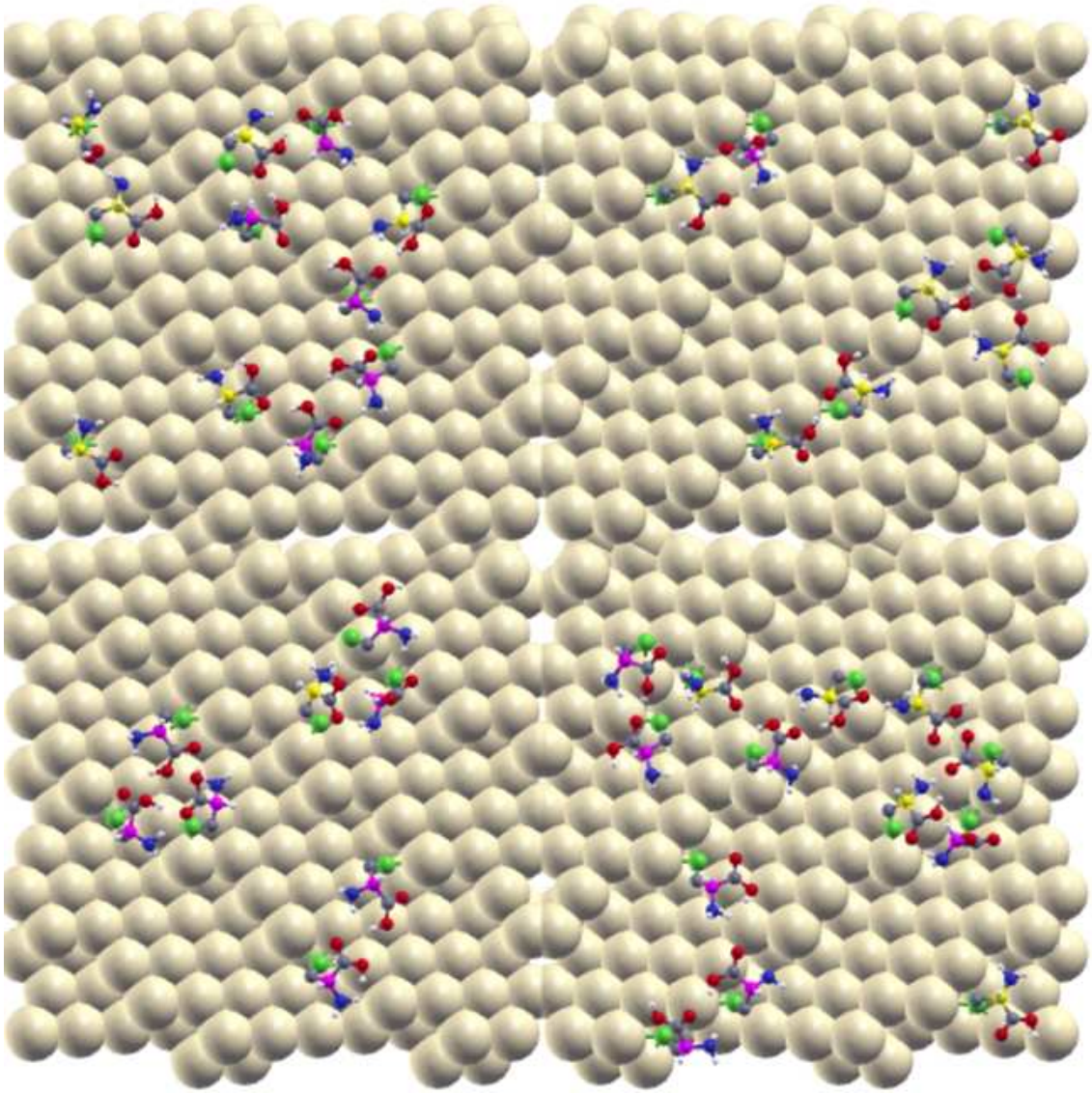

Figure 7.11: A simulation snapshot of racemic systems of neutral D-cysteine adsorbed on Au(643)$^{R\&S}$ surface at T=296 K. Although identical, the chiral centers in the two enantiomers are colored in yellow and magenta, respectively.

on flat Au(111) surfaces, as well as on simple chiral Au(643) surfaces, the molecules

here were involved in homochiral or enantiomerically enriched rosette clusters.

7.5 Chiral surfaces with uniform potential

We investigated the self-assembly of model molecules A and B (both described in detail in Chapter 3) on two chiral surfaces (643) and (531), respectively, by considering different surface attraction and surface atom sizes. Here, as a first approximation, the surface atoms, regardless of their coordination numbers were presented by the same Lennard-Jones energy parameters.

7.5.1 Molecules with one chiral center adsorbed on chiral surfaces

Chiral separation was achieved upon adsorption of model molecules A (shown in Figure 3.1 (a)) on achiral solid substrates, as well as on higher reactive chiral surfaces presented above. The molecules here adsorbed on chiral surfaces described by a uniform potential. Homochiral rosette clusters that were encountered previously on square and hexagonal surfaces formed on uniform chiral surfaces as well. The two enantiomers of the racemic mixture formed similar adsorption patterns and desorbed together from both, chiral (643) and (531) surfaces. Overall, there were insignificant differences in binding of the two mirror images of the chiral molecule on a specific enantiomer of the chiral surface.

Uniform potential (643) surfaces were not enantioselective regarding to the binding and self-assembly of the two enantiomers of the chiral molecule. Micellar homochiral structures seen here resembled those obtained on flat surfaces. Molecules adsorbed on the terraces of the surface, with (111) geometry, and overall the (643) substrate

behaved as a hexagonal surface. Single molecules were observed at inner kink sites at low and intermediate temperatures (see Figure 7.12). Inner kink sites were preferred because of greater overall dispersion interactions between molecules and surface atoms. At such sites, the molecule interacts with surface atoms from edges as well as from terraces.

A simulation snapshot of an adsorbed racemic mixture of molecule A on chiral (531) surfaces is shown in Figure 7.13. The molecules self-assembled in homochiral clusters on the chiral surface. However, chiral surfaces may alter chiral segregation. This was reflected by a larger proportion of small clusters. We calculated average numbers of k-molecule clusters, where k was considered between 3 and 10. We report these averages for k = 3–6 in Table 7.4. As shown in Table about 30% of clusters were small (3 or 4 molecules) on a flat surfaces ((111) and (100)), whereas up to 60% such clusters formed on (531) surface when the size of the surface atoms was equal to that of the bulky group of the adsorbate (σ_s^*=2), Figure 7.13 (a). Smaller clusters commensurated better with the rough surface.

Table 7.4: Average sizes of clusters formed on various surfaces at T*=1.64

Surface geometry	ϵ_s^*	σ_s^*	N_{tot}^1	$N_3(\%)$	$N_4(\%)$	$N_5(\%)$	$N_6(\%)$
(531)	1	2	41.0	19.7	40.9	30.3	8.9
		4	40.4	6.9	31.3	55.3	6.3
(643)	1	2	39.2	7.6	24.4	57.0	10.5
		4	39.0	15.0	22.4	51.5	10.6
(111)	1	2	39.5	7.1	20.3	56.2	13.7
		4	39.6	3.8	18.7	64.1	12.9
(100)	1	2	39.6	3.8	19.2	63.1	19.9
		4	38.7	5.4	6.5	66.7	20.7

[1] N_{tot} represents the total number of clusters formed on a particular surface. A larger N_{tot} indicates in itself a move towards formation of smaller clusters.

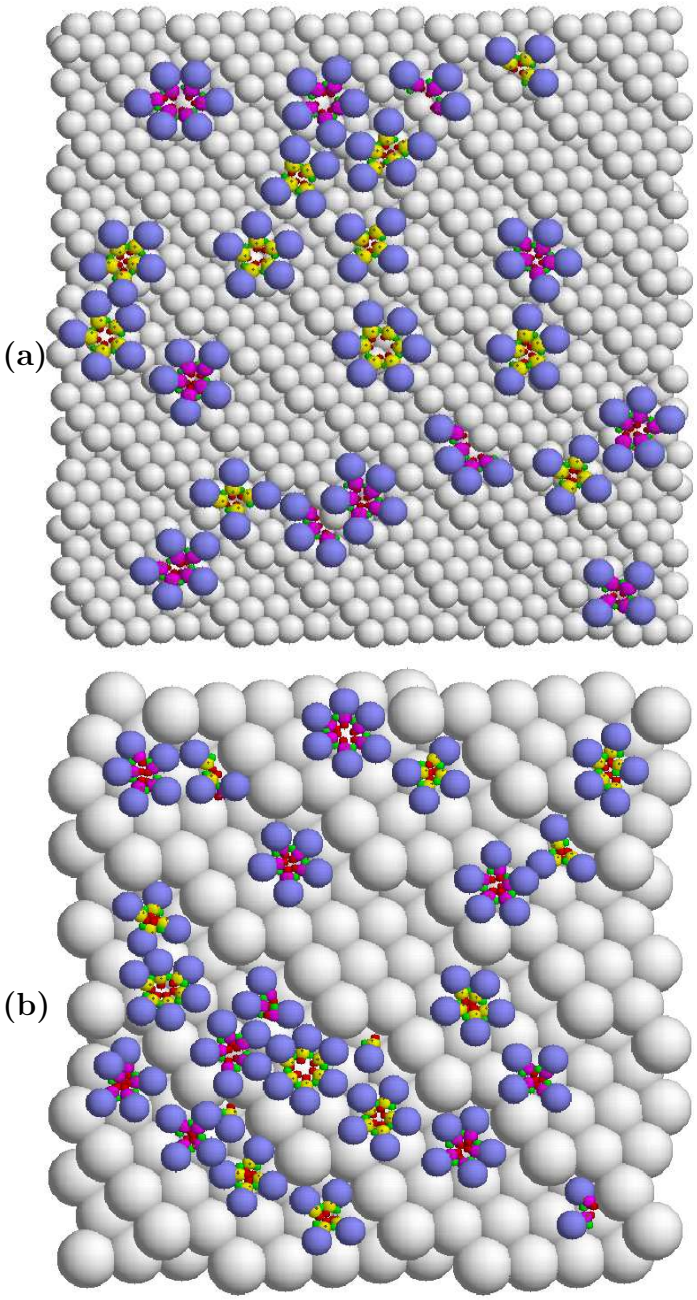

Figure 7.12: A simulation snapshot of molecules A adsorbed onto chiral (643) surface with σ_s^*=2 (a) and 4 (b) at T*=2. Although identical, the chiral centers in the two enantiomers are colored in yellow and magenta, respectively. The chiral surface here presents surface atoms that are of similar reactivity regardless of their coordination number.

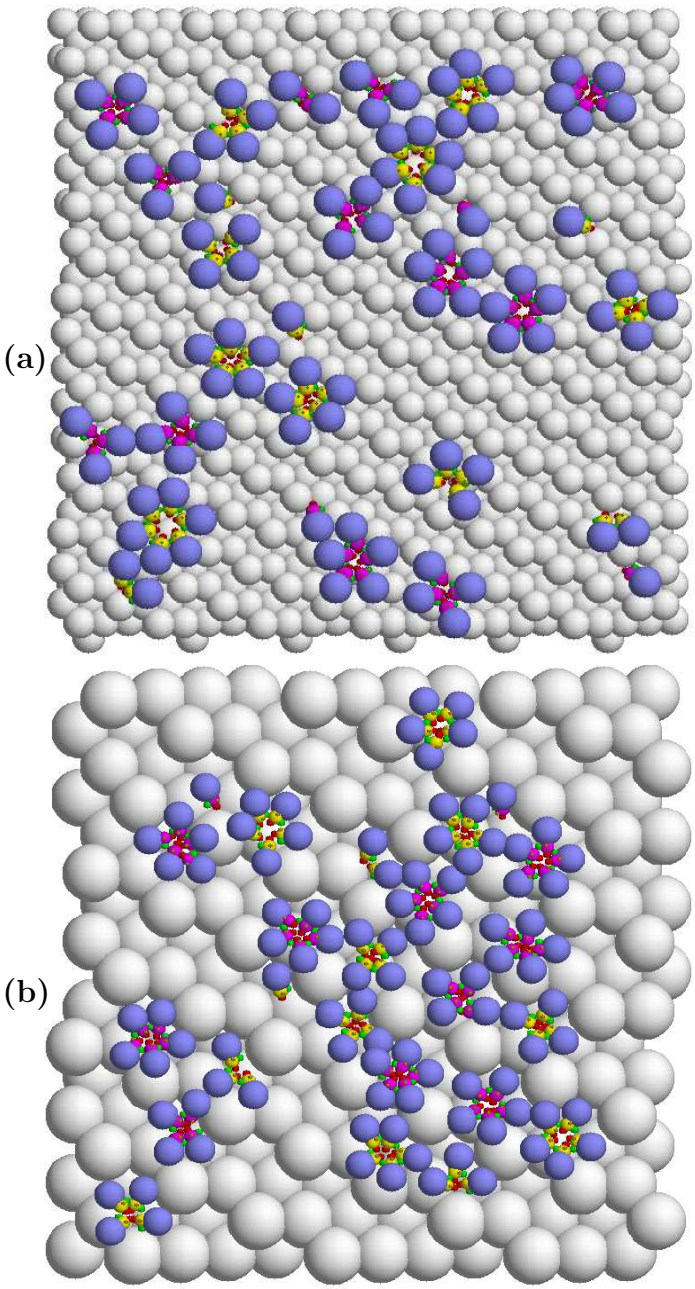

Figure 7.13: A simulation snapshot of molecules A adsorbed onto chiral (531) surface with σ_s^*=2 (a) and 4 (b) at T*=2. Although identical, the chiral centers in the two enantiomers are colored in yellow and magenta, respectively. The chiral surface here presents surface atoms that are of similar reactivity regardless of their coordination number.

7.5.2 Molecules with two chiral centers adsorbed on chiral surface

Self-assembly patterns of molecules B (shown in Figure 3.1 (a)) formed on chiral surfaces were similar to the structures formed on flat surfaces as can be observed from Figure 7.14. Larger terraces of (643) surfaces could host extended double chain structures of molecules B, in which molecules with opposite chirality generaly alternated, as well as large homochiral rosettes. The double chain formed along the terraces and near to the step edges. The temperature dependence of the fraction molecules involved in like (F_l) and unlike local structures (F_u) formed on (643) chiral surface is shown in Figure 7.15 (black lines). As seen in the Figure up to 70% of molecules were involved in heterochiral chain structures at low and intermediate temperatures. A much smaller fraction of molecules formed homochiral rosette structures on (643) surface.

The terraces of the (531) surface were narrower and could not fit a whole micelle or an extended chain. Thus the final rosette structures were not adsorbed flat on one terrace, but were shared by neighbouring terraces. The chain aggregates also extended along the terraces, up and down the stepped edges. Such chains were also less flat than the double chains formed on (643) surfaces. As shown in Figure 7.15, the fraction of molecules that had exclusively like neighbours on the (531) surface was larger (up to 40%) than on the (643) surface. The increase in like fraction was not necessarily given by a larger number of homochiral rosette clusters, but rather by the locally homochiral structures within the extended chain-like aggregate. The final adsorption pattern of molecule B was therefore influenced by the surface layout. The (643) surface with larger terraces accommodated better heterochiral double chains,

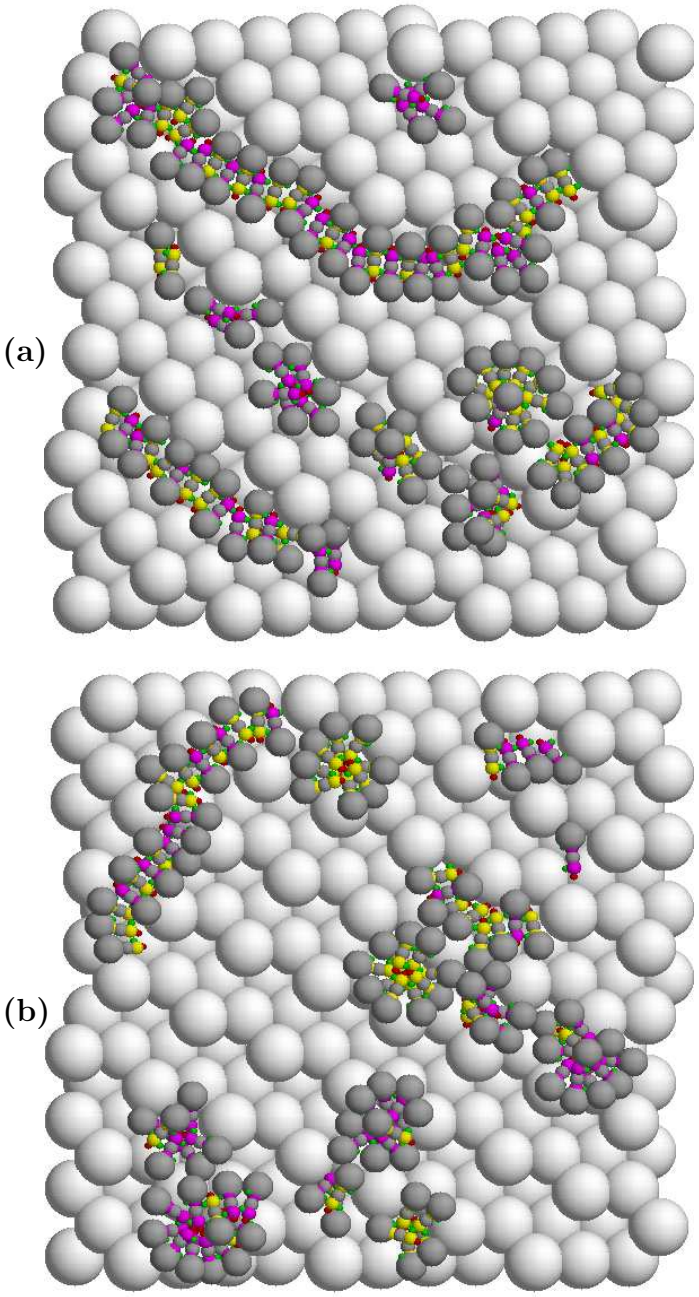

Figure 7.14: A simulation snapshot of molecules B adsorbed onto (643) (a) and (531) (b) chiral surfaces with σ_s^*=4 at T*=1.61. Although identical, the chiral centers in the two enantiomers are colored in yellow and magenta, respectively. The chiral surface here presents surface atoms that are of similar reactivity regardless of their coordination number.

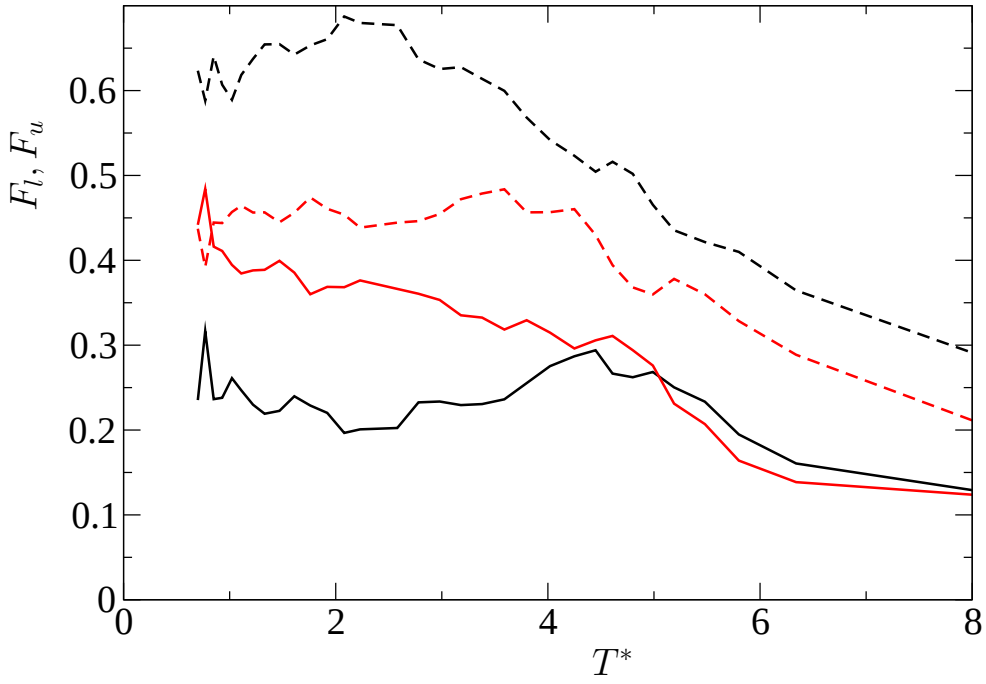

Figure 7.15: Temperature dependence of the fraction of the total number of molecules B involved in like (F_l, solid lines) and unlike (F_u, dashed lines) local structures. Black and red lines are representative for the chiral (643) and the (531) surfaces, respectively.

whereas the (531) surface with narrower terraces favored the formation of extended aggregates where locally homochiral structures of opposite chirality alternated within the same aggregate.

7.5.3 Cysteine molecules

Racemic mixtures, composed of 100 flexible neutral cysteine molecules and enantiopure D-cysteine systems of 50 molecules, respectively were adsorbed on a uniform potential (643) surface. Simulation snapshots of adsorption of neutral cysteine molecules are shown in Figure 7.16. Even though the chiral surface here presented surface atoms

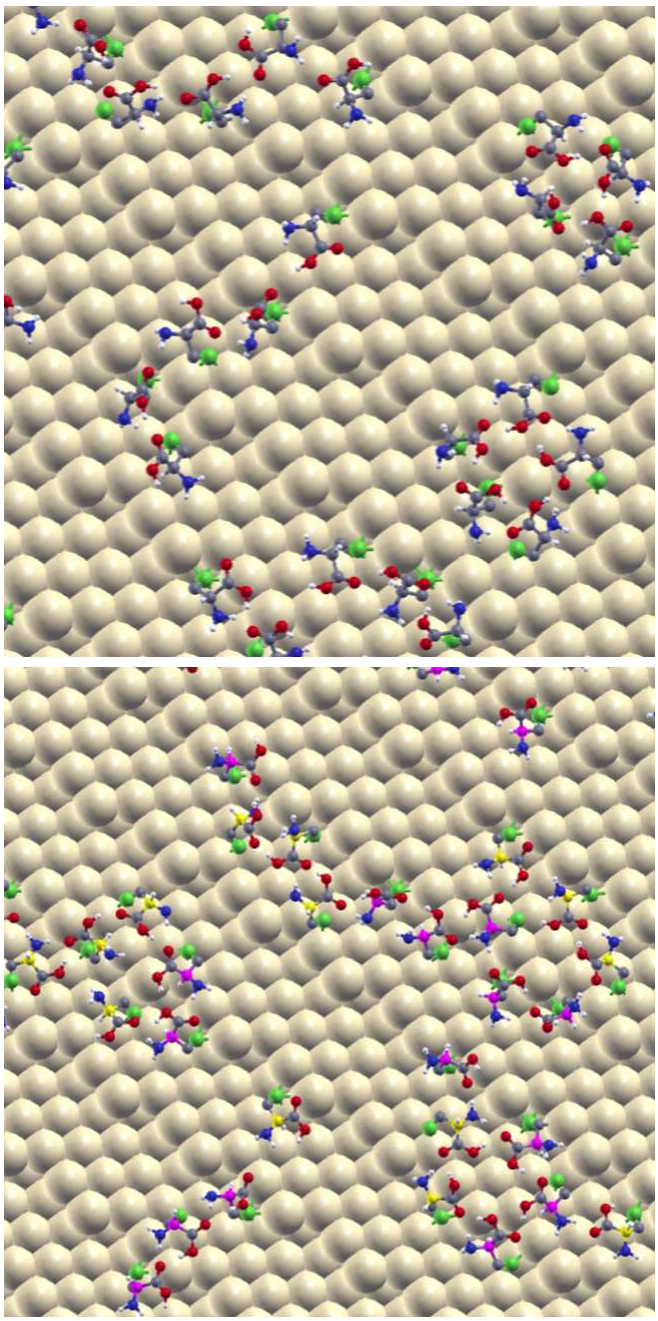

Figure 7.16: Simulation snapshots of enantiopure (a) and racemic (b) neutral cysteine adsorbed onto (643) chiral surface at T=296 K. Although identical, the chiral centers in the two enantiomers are colored in yellow and magenta, respectively. The chiral surface here presents surface atoms that are of similar reactivity regardless of their coordination number.

of similar reactivity, the molecules adsorbed mostly along the edges and around the kinks. Those locations were preferred because the molecules gained binding from terraces, as well as from the edges and kinks, and often even from the neighbouring upper or lower terraces. As seen in the Figure 7.16, H-bonded rosette structures and molecular rows were formed upon adsorption of neutral cysteine molecules that resembled the structures encountered on Au(111) surface.

Adsorption of the racemic mixtures of cysteine on chiral Au(643) were also considered. Racemic mixtures of neutral molecules presented enantiomerically enriched rosette structures as shown in Figures 7.16 (b) and previuosly seen on Au(111) surfaces. Relatively short molecular rows formed generally along the stepped edges. A smaller fraction of such rows, however, were seen across the edges as well.

7.6 Summary

Naturally chiral surfaces carry surface atoms with different coordination numbers. Such surface atoms present different reactivity. A suitable force field that accounts for non-uniform surface attraction is certainly desired. We used DFT calculations to design a coordinated specific force field parameters and implemented in our classical PTMC simulations. Further self-assembly of chiral toy models and cysteine amino acids on naturally chiral surfaces was investigated using PTMC. Strongly attractive kink sites generally accommodated homochiral structures of model molecules. Lowest coordinated surface atoms of a relatively large size were often involved in more than one assembled structure. The adsorption structures were formed on both facets neighboring kink sites. Simulations of chiral adsorption of flexible molecules required extensive computational cost. Smaller systems showed that molecules of cysteine

preferentially adsorbed at kink and edge sites and were involved in structures that resembled the adsorption patterns encountered on Au(111) surface. Rosette structures of neutral molecules were formed at kink sites, whereas molecular rows extended along the edges.

Chapter 8

Chiral behavior of zwitterionic adsorbed states of cysteine, homocysteine and methionine on Au(111) surface

A complicating factor in understanding the surface self-assembly of amino acids is the molecular charging state. Whether the molecule appears in neutral, zwitterionic or even anionic form depends on the presence of solvent, surface coverage, the exposed gold facet and the nature of the probing experiment.[76, 79, 152, 157, 160–162] The present understanding, based on XPS (X-ray photoelectron spectroscopy) measurements on Au(111) is that cysteine is mostly neutral at low coverage (up to a half monolayer) and zwitterionic at high coverage, even in ultrahigh vacuum (UHV) conditions.[157] On the other hand, the molecular charging state impacts its assembly patterns as well as its binding to the underlying surface.

In this Chapter, the adsorption on Au(111) of cysteine, homocysteine and methionine in zwitterionic forms is investigated. In a first attempt to understand the presence of these species in metal-supported monolayers of amino acids, we considered the adsorption of monomers and dimers of the three amino acids. Binding conditions in like and unlike dimers, as precursors of pattern formation in extended systems were examined using a combined classical/quantum methodology, and are described in Section 8.2. Extended systems of enantiomerically pure and racemic cysteine, homocysteine and methionine and their chiral self-assembly on Au(111) surface was investigated with classical Parallel Tempering Monte Carlo methods. The results of the latter studies are discussed in Section 8.3. Investigation of zwitterionic cysteine chemisorbed on naturally chiral Au(643) surface is presented in Section 8.4.

8.1 Models and simulation details

The molecular structures of the cysteine, homocysteine and methionine adsorbates in zwitterionic molecular states are presented in Figure 8.1. In this study, cysteine and homocysteine were deposited on the gold surface in the chemisorbed R−S (thiolate) forms, whereas physisorbed R−S−CH_3 (thioether) form of methionine was employed. All the chiral adsorbates were considered in their dextro isomer, except in unlike dimers and racemic mixtures where dextro and laevo isomers were present together.

For PTMC calculations of monomers and dimers, the substrate was a two-layer Au(111) slab, with 127 gold atoms. The size of the non-periodic simulation box was chosen so that interactions between image cells would be negligible. Evaporative events (particles leaving the simulation box) were forbidden, by rejecting moves that led to evaporation. Molecular flexibility was considered by calculating contributions

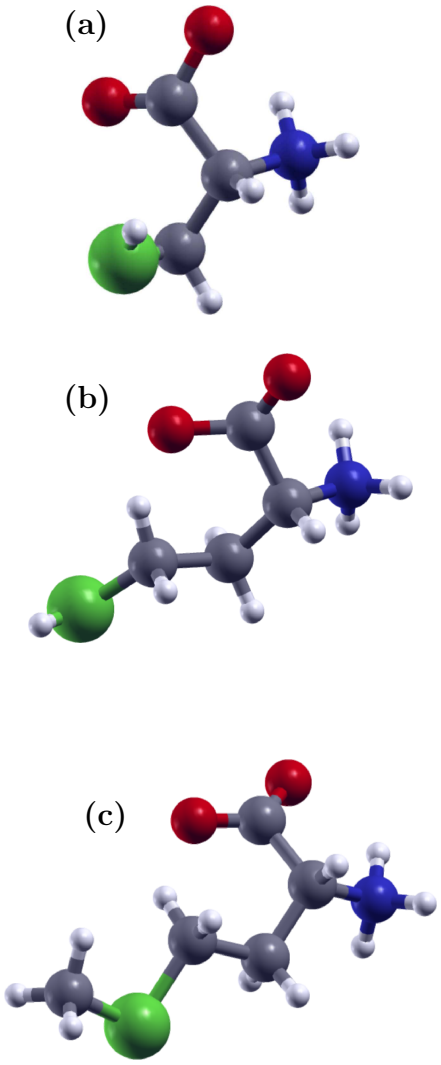

Figure 8.1: Zwitterionic molecules investigated: (a) D-cysteine, (b) D-homocysteine, and (c) D-methionine. Atom coloring is consistent with the figures below.

from intramolecular terms to the total energy of the system as described in Chapter 2. Bond lengths were held constant. Only intermolecular nonbonded interactions were considered, described by pairwise atom-based Lennard-Jones and Coulombic

potentials. The flat gold surface used for PTMC calculations of larger systems (50 and 100 adsorbed molecules) was modeled using a one layer Au(111) slab. The chiral (643) surfaces were modeled as described in Chapter 7. The number of atoms depends on the molecules that were adsorbed. Larger molecules needed a larger surface in order to keep the density relatively similar between different systems, within low- to medium-coverage conditions.

For DFT calculations of monomers and dimers the substrate was a three-layer, 168-atom Au (111) slab, with periodic boundary conditions. A third ideal Au(111) layer of atoms was added to the PTMC simulation structure to ensure convergence of the surface energy. In all geometry optimizations, two layers of gold atoms were held frozen, while the top layer was allowed to optimize.

8.2 Monomers, dimers and surface binding

Monomer zwitterionic structures of cysteine, homocysteine and methionine were considered in our calculations but none optimized successfully in our DFT calculations. Initial PTMC-equilibrated zwitterions underwent hydrogen transfer to reform the neutral amino acid, dissociated or were found to be unstable in their quantum equilibration. Similar behaviour has been observed previously for zwitterions on Au(110) surfaces.[139]

Significant differences between like unlike dimers were observed for zwitterionic structures. Despite the instability of zwitterionic monomers, we considered the possibility that zwitterionic forms can be stabilized by electrostatic interactions in dimers. This hypothesis followed the experimental observations of Naitabdi and Humblot [36] who found that in ultrahigh-vacuum, zwitterionic methionine was stable only

in molecular pairs or chains of molecular pairs. Several initial structures were considered in PBE for like and unlike dimers of the three amino acids. Neither like or unlike zwitterionic cysteinate dimers converged to zwitterionic forms. Rather, intermolecular proton transfer occurred during the optimization, leading to neutral dimers with NH2–COOH H-bonds (Figure 8.2 (a)). For both homocysteine and methionine however, like zwitterionic dimers converged and presented stabilization energies comparable to those of neutral dimers (see Figure 8.2 (b) and (c)), while zwitterionic unlike dimers were unstable.

Analysis of the adsorbed geometries presented in Figure 8.2 (b) and (c) revealed that zwitterionic dimers formed adsorbed geometries significantly closer to substrate than neutral dimers: Oxygen atoms were found as close as 2.5 Å from the surface in zwitterions. This minimum distance was 3.5 Å for neutral molecules. The low height geometry of the zwitterionic dimer was due to the stronger interactions between the electrostatic charges and the metal surface, and stronger intermolecular interactions requiring smaller intermolecular distances. Both of these interactions also likely contributed to the stabilization of surface-supported zwitterion dimers in vacuum conditions: the instability of chemisorbed zwitterion monomers shows that intermolecular interactions were necessary for the existence of zwitterions. The requirement of a smaller surface separation in zwitterion formation led to the inability of heterochiral zwitterions to stabilize on the surface: to form favorable dimer electrostatic orientations, one of the enantiomers in the unlike dimer was required to have the H atom on the chiral carbon pointing towards the surface. The resulting steric repulsion led to the molecule being pushed away from the surface, and destabilization of the dimer. These results suggest significant chiral discrimination in the adsorption process of zwitterions on surfaces, but more work has to be done to understand the

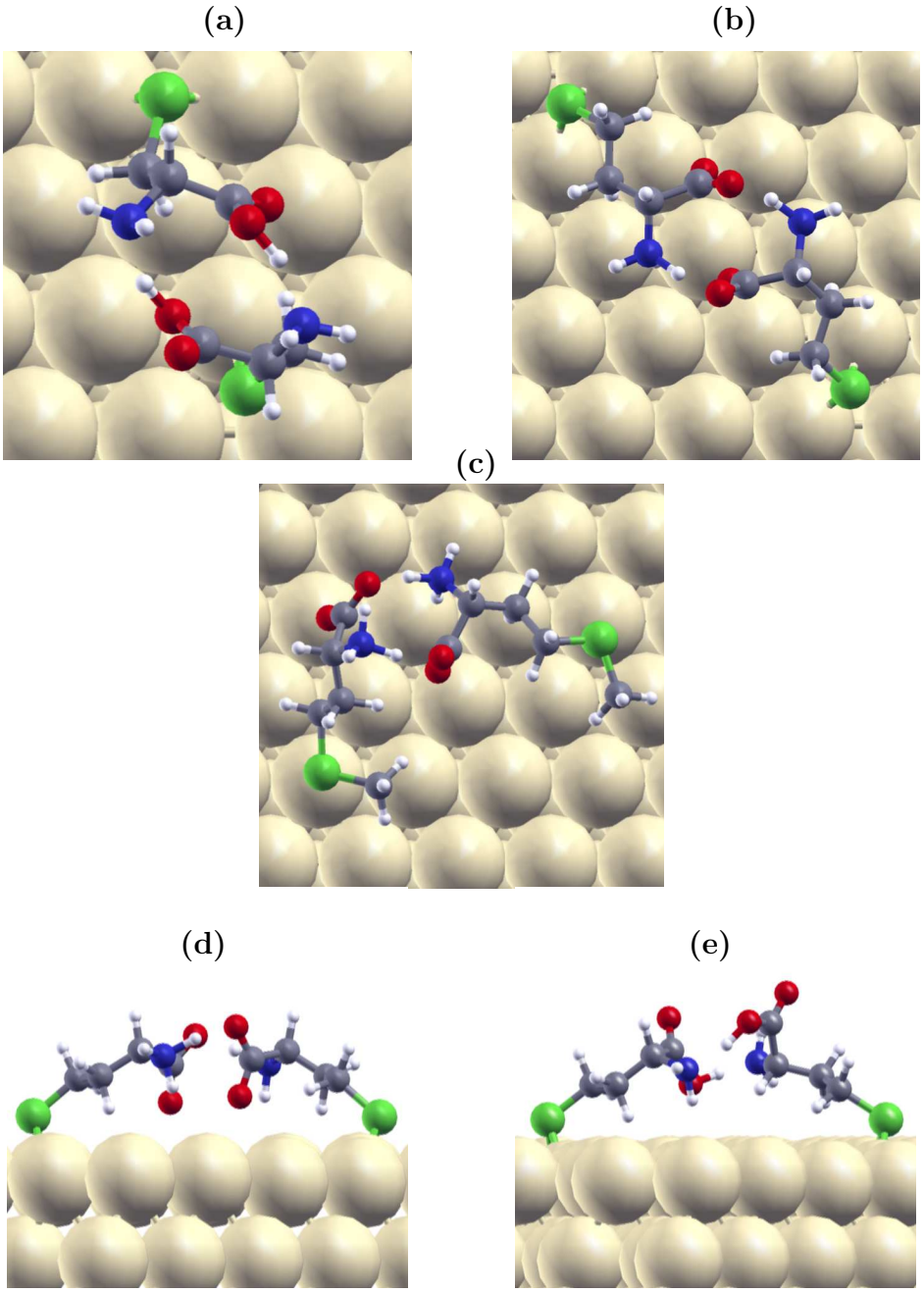

Figure 8.2: Equilibrium adsorbed structures of zwitterionic like dimers of DD-cysteinate (a), DD-homocysteinate (b) and DD-methionine (c), respectively. Side pictures showing molecular height on the surface for the like homocysteinate zwitterion dimer and the unlike dimer are presented in figures (d) and (e) Note that the cysteinate initial zwitterion equilibrated to a neutral dimer with NH2 -COOH H-bonds, as did all unlike dimers that were initially zwitterions.

formation of zwitterions in vacuum before more definitive statements on this issue can be made.

8.3 Extended systems of zwitterions

In zwitterionic adsorbates, the carboxylate group interacts stronger with the surface than the ammonium group does, but both groups are also involved in intermolecular coulombic interactions. The strong electrostatic interactions dominate the overall potential energy to the detriment of dispersive surface interactions, and thus cysteine zwitterions mainly bind to the gold surface via their thiol group.

8.3.1 Adsorption of zwitterionic D-cysteine

In zwitterionic form, cysteine molecules were involved in electrostatically driven self-assemblies. Simulation snapshots of zwitterionic D-cysteine adsorbed on Au (111) surface is shown in Figure 8.3. Positively charged NH_3^+ groups attractively interacted with negatively charged COO^- groups in a single and double row conformations. A molecular row was a relatively straight single line of molecules that self-assembled mainly through intermolecular electrostatic interactions. Each molecule interconnected with two molecules along the row: through NH_3^+ group on one side and COO^- group on the other side. The molecules bound to the surface through sulfur atom and had the backbone slightly desorbed and involved in binding with neighbouring molecules. Molecular dipoles given by the charged NH_3^+ and COO^- groups were parallel to the surface and aligned along the molecular row.

Two interacting rows of cysteine molecules formed a double-row structure (see Figure 8.3). Such double rows prevailed the adsorption pattern over single rows,

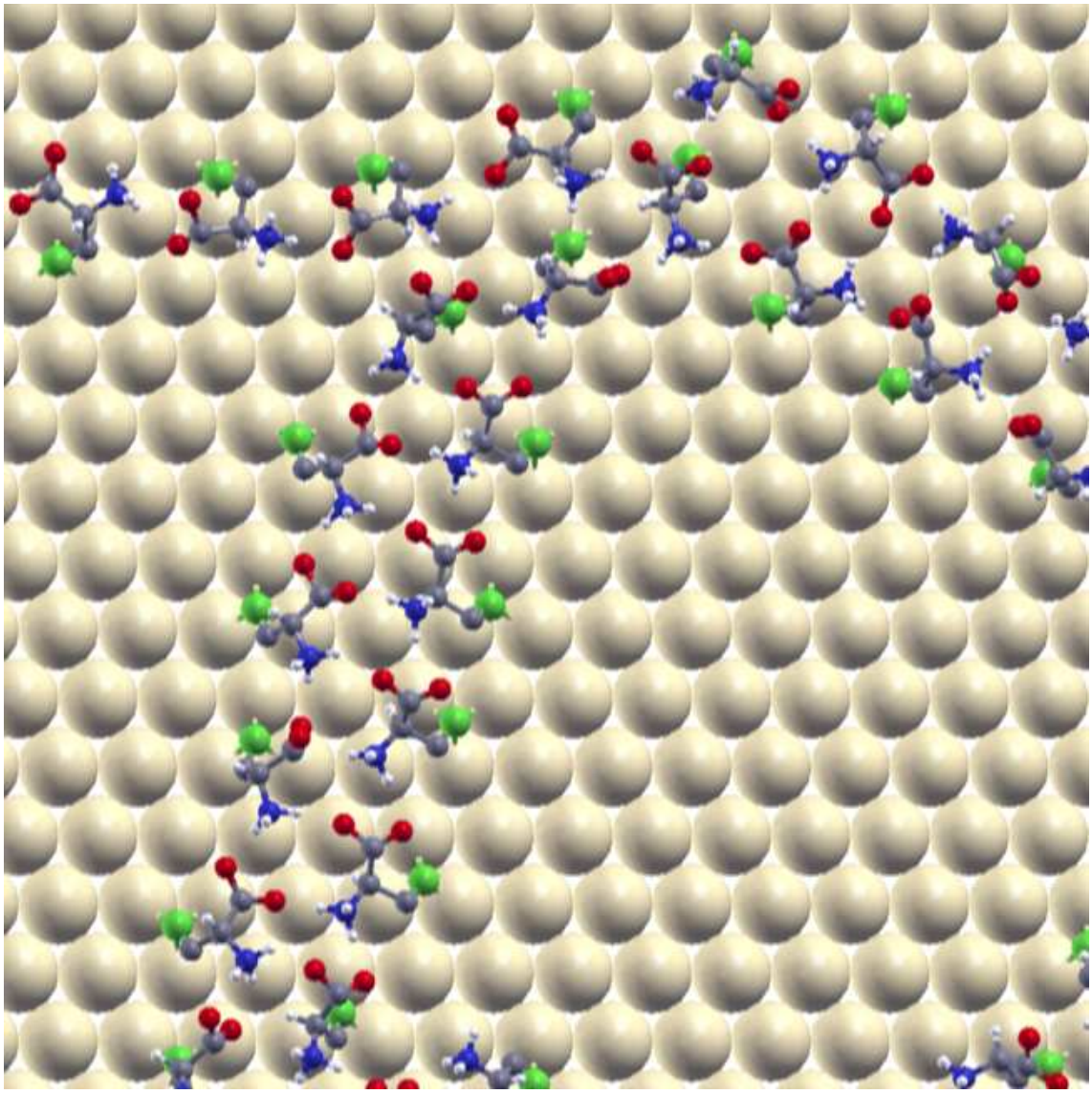

Figure 8.3: A simulation snapshot of zwitterionic D-cysteine in thyil form adsorbed on Au(111) surface at T=296 K.

because of the additional stability given by the strong interaction between the molecular rows. Each molecule that belonged to a row structure interacted to one or two other molecules from the adjacent row. As a result, two types of double rows were encountered. In the first structure, cysteine pairs were formed between parallel rows,

in which each molecule interacts with one other molecule from the opposite row. Such structure may also be seen as a single row of cysteine dimers. In the second structure, one molecule interacted with two other molecules from the adjacent row, resulting in a zig-zag type of geometry. Both of the structures can be seen in Figure 8.3. In such geometries, the dipoles of the adjacent rows established an anti-parallel alignment.

The adsorption assemblies formed upon adsorption of zwitterionic cysteine were also stabilized through H-bonding. The H-bonds were formed between oxygen of the carboxylate group and hydrogen of the ammonium group. The H-bonding was encountered along a molecular row as well as between the molecular rows in the double row geometry.

8.3.2 Adsorption of zwitterionic D-homocysteine

Zwitterionic homocysteine was mostly involved in single and double row conformations in both upright and parallel adsorption geometries described in Chapter 6. A simulation snapshot is shown in Figure 8.4. Generally, double rows of parallel adsorbed homocysteine had the NH_3^+ and COO^- groups interaction at the inner side of the row and the thiol (thyil) groups positioned outside. The double row conformation was stabilized through electrostatic interactions along the molecular row and between the adjacent rows. In the parallel geometry, the dispersion interaction between the backbone of homocysteine molecules and the gold surface offered additional stability to the adsorption pattern.

In the upright geometry, occasionally, multiple rows were formed. An example of such structure is shown in Figure 8.5. The conformations were stabilized through intermolecular electrostatic and dispersion interaction. The multiple row structure, however, was not as well organized as the double row structure, the molecules inter-

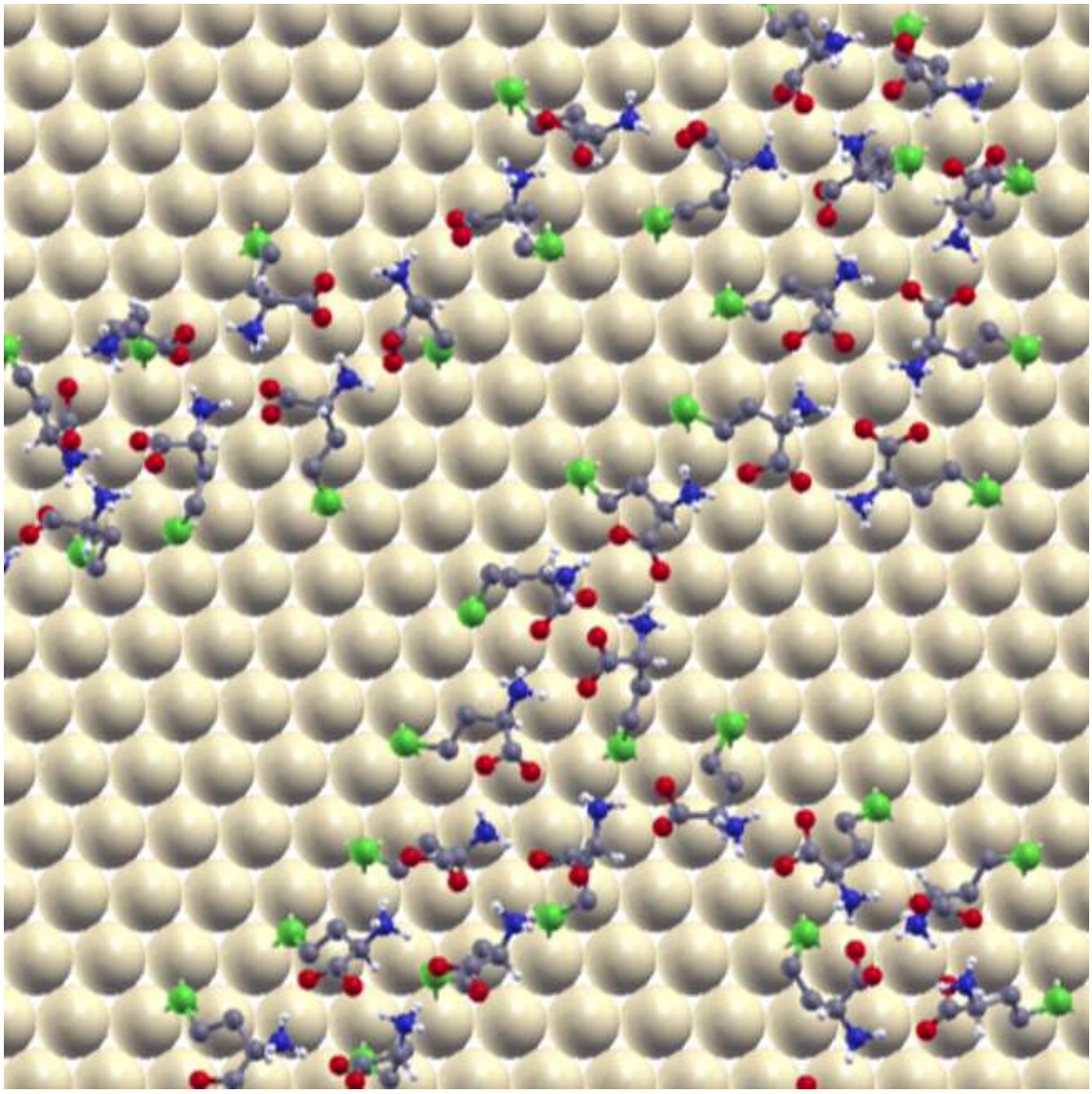

Figure 8.4: A simulation snapshot of zwitterionic D-homocysteine in thyil form adsorbed on Au(111) surface at T=296 K.

acting electrostatically not as efficient in the former because of the short-range steric repulsion. Ammonium and carboxylate groups in this configuration were both pointing away from the surface, and thus could only be involved in some of the binding with other neighbouring molecules. In a double row conformation each charged group

(a)

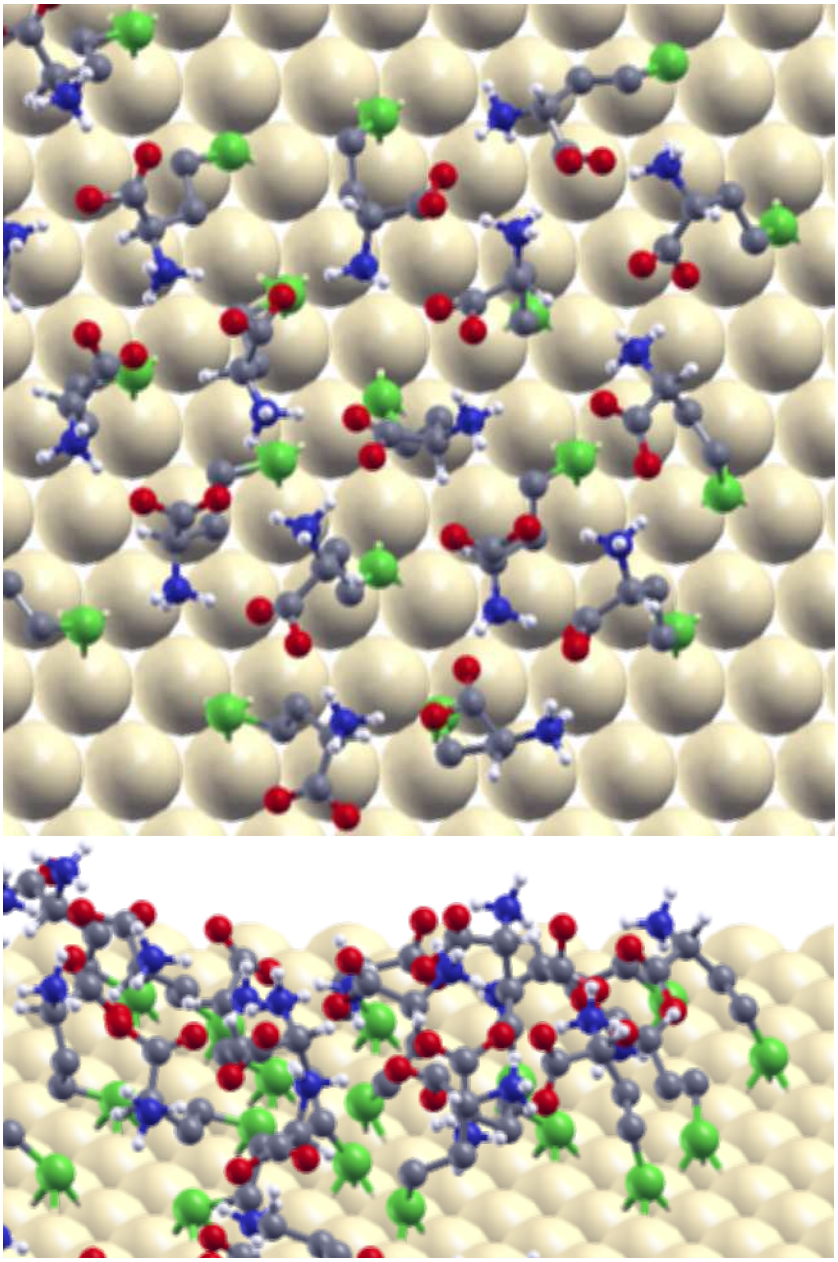

(b)

Figure 8.5: A simulation snapshot of zwitterionic D-homocysteine in thyil form adsorbed on Au(111) surface at T=296 K. The top (a) and lateral (b) views of a local multiple-row structure are presented.

interacted with two oppositely charged groups. That could not always be satisfied in a multiple row structure. The system oscillated between single, double and multiple row configurations along the entire range of temperatures considered. However, a relatively larger fraction of molecules were involved in double row conformation.

8.3.3 Adsorption of zwitterionic D-methionine

The zwitterionic D-methionine molecules adsorbed on the Au (111) surface were generally involved in double row conformations. A simulation snapshot is shown in Figure 8.6. The double row structures were similar to the structures formed by homocysteine that adsorbed parallel to the gold surface. Such double rows were stabilized through electrostatic interactions and H-bonding formed between and along the molecular rows. The parallel rows of zwitterions resemble the adsorption patterns observed by Naitabdi et al. in STM images [36]. Our simulations results were hence in good agreement with the experimental data.

8.3.4 Adsorption of racemic amino acids

Racemic mixtures of zwitterions were involved in single and double row geometries as did the enantiopure systems. Occasionally multiple rows were formed by zwiterrionic homocysteine and methionine molecules that adsorbed in an upright geometry with the backbone fully desorbed from the surface. However, the planar configurations (with the molecular backbone parallel to the surface) of homocysteine and methionine dominated overall the adsorption pattern. Simulation snapshots obtained for the adsorption of racemic mixture of cysteine and methionine, respectively are shown in Figure 8.7. As can be observed from the Figure, in zwitterionic configurations chirality

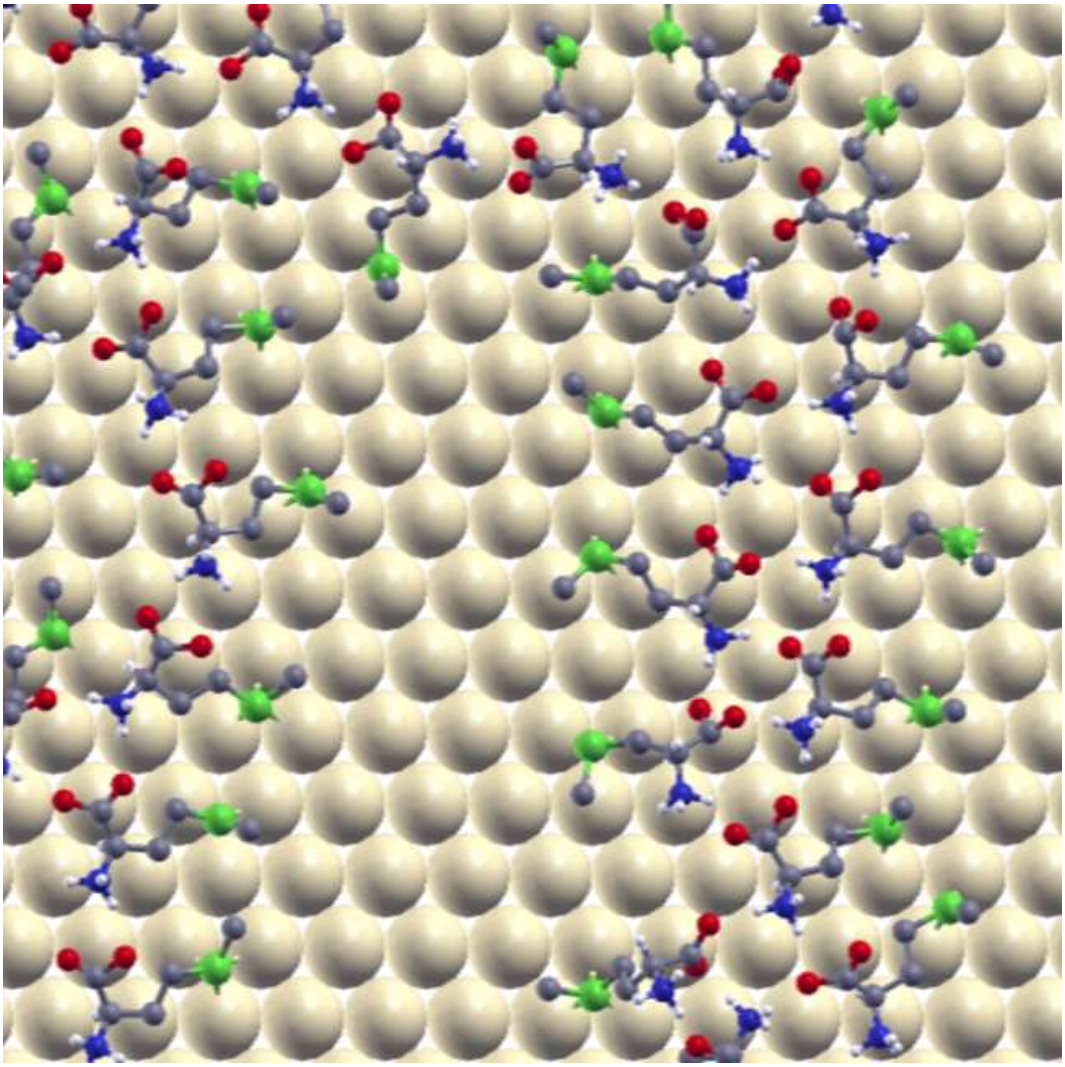

Figure 8.6: A simulation snapshot of zwitterionic D-methionine adsorbed on Au(111) surface at T=296 K.

was conserved along the row. Single homochiral molecular rows were coexisting with homochiral or racemic double parallel rows. Double rows generally consisted of two homochiral chains of the same or different chirality.

Zwitterionic molecules presented chiral recognition along the molecular row. PTMC simulations of zwitterionic dimers of homocysteine and methionine presented two competing structures for like dimers. Such dimer structures formed by homocys-

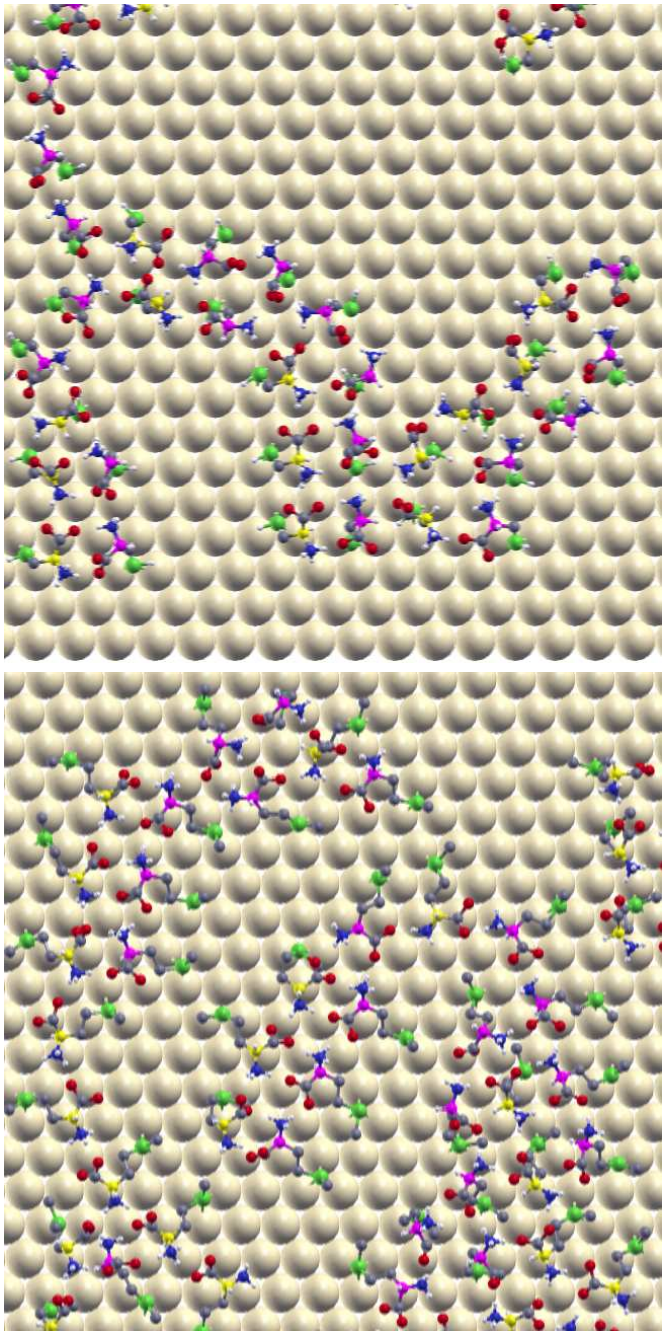

Figure 8.7: A simulation snapshot of zwitterionic racemates: cysteine (a) and methionine (b) adsorbed on Au(111) surface at T=277 K. Although identical, the chiral centers in the two enantiomers are colored in yellow and magenta, respectively.

teine are presented in Figure 8.8. The two configuration were illustrative of “inter-” and “intra-row” local structures. In ”inter-row” geometry (see Figure 8.8 (a)), the molecules had their thyil groups further apart as if they were parts of opposite molecular rows if referring to the bulk simulations. In “intra-row” structure (see Figure 8.8 (b)) the thyils groups were closer to each other as if the molecules belonged to the same molecular row. Both structures were stabilized through electrostatic interaction, H-bonding and adsorbate-surface interaction. The “intra-row” structure, however, presented an additional stability due to dispersion interaction between molecular backbones. Unlike dimers equilibrated with PTMC formed only the ”inter-row” structure, in which thyil groups were further apart. As a result, the molecules formed parallel molecular rows of the same or different chirality, but along the row the chirality was conserved due to a preferential interaction of like molecules. The ”intra-row” configuration, however, presented different binding than bulk simulations. In bulk simulations a molecule interacted electrostatically along the row with a neighbouring molecule on one side through NH_3^+ group and with another one on the other side trough COO^-. In the intra-row dimer structures, one molecule interacted electrostatically through both ammonium and carboxylate with the second molecule.

Cysteine presented one type of structure for both like and unlike dimer. The S-S distances were relatively similar between molecules from the same row, as well as from the opposite rows. However, in the multibody system considered here, a preferential homochiral alignment along the row was seen for cysteine molecules as well (see Figure 8.7). In such multibody systems, a complex interplay of effects governs the self-assembly process. Understanding and prediciting the adsorption behaviour of zwitterionic amino acids on surfaces requires more investigations.

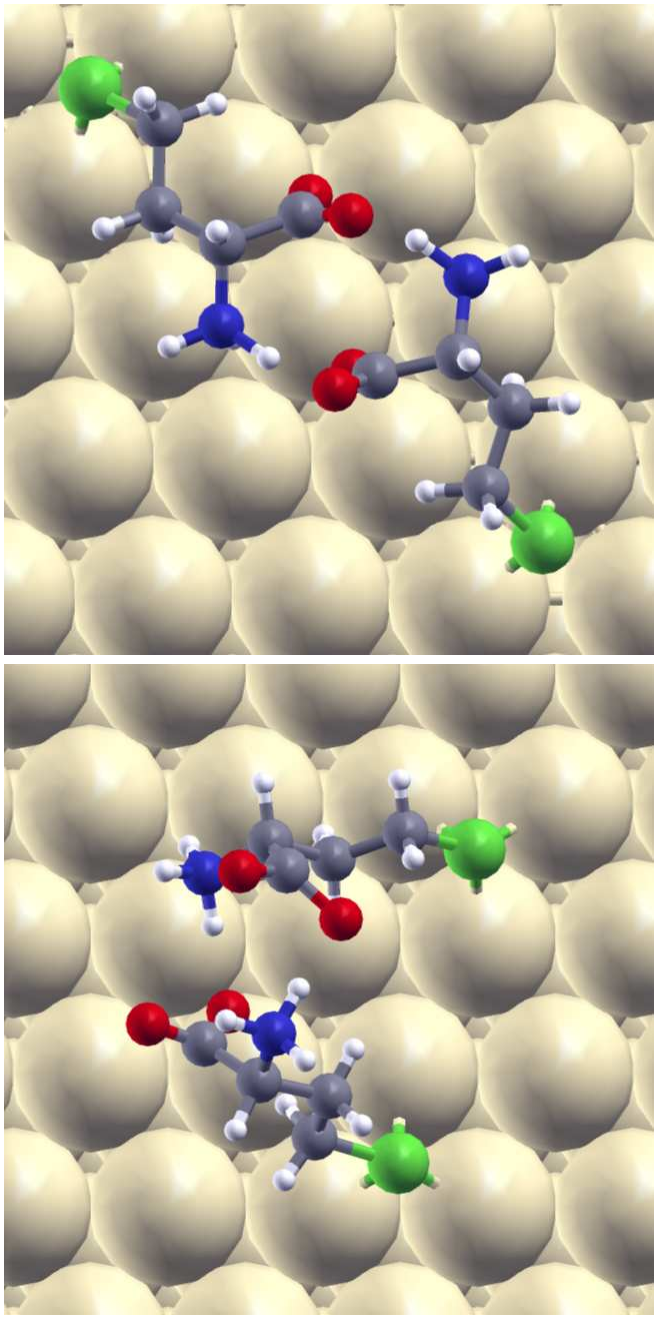

Figure 8.8: PTMC simulation snapshots of zwitterionic like dimer of D-homocysteine adsorbed on Au(111). The two competing configurations are representative for the molecular interaction between (a) and along (b) the molecular rows encountered in bulk simulations.

8.4 Adsorption of zwitterionic cysteine on naturally chiral surfaces

We considered the chemisorption of enantiomerically pure and racemic mixtures of zwitterionic cysteine on chiral Au(643) surface. The chiral surface here was described by force field parameters that are coordination number dependent. The smaller systems showed that molecules, as seen for neutral molecules, adsorbed preferentially to the kink sites and stepped edges. As seen in Figure 8.9 molecular rows were formed upon adsorption of zwitterionic molecules of cysteine on chiral Au(643) surface at room temperatures. Such structures resemble the structures encountered on Au(111) surfaces. Lower temperatures snapshots showed similar trends. At higher temperatures, shorter molecular rows were encountered. Molecular rows were stabilized though electrostatic intermolecular interaction and extended along the edges, where molecules preferred to bind as well as across the edges. The double row structures that were more stable than single rows on Au(111) surface, due to additional electrostatic interaction and H−bonding between single rows, were less encountered on highly attractive chiral Au(643) surfaces.

Racemic mixtures of zwitterionic cysteine were also considered in our study. A simulation snapshot of chemisorbed zwitterionic racemate of cysteine is shown in Figure 8.10. Extended molecular rows were formed by zwitterionic molecules. Generally, the chirality was conserved along the molecular row, as seen previously on Au(111) surfaces. We also investigated the adsorption of enantiopure and racemic systems of cysteine on a $Au(643)^{R\&S}$ surface. Such surfaces presented local homochiral facets, although the entire surface was heterochiral. Simulation snapshots of enantiopure and racemic systems on such heterochiral Au(643) surfaces are shown in Figures 8.11

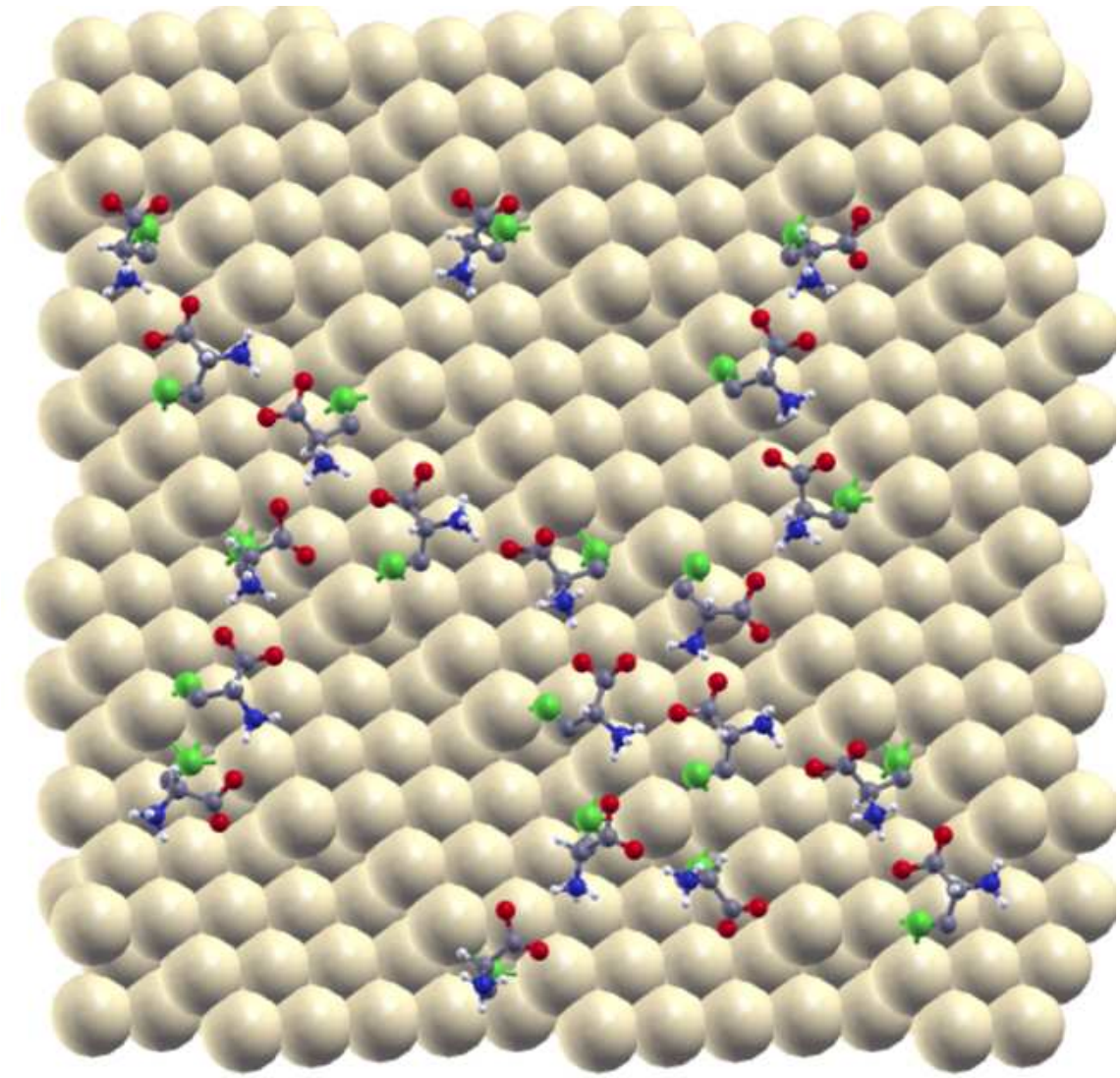

Figure 8.9: A simulation snapshot of a enantiomerically pure system of zwitterionic D-cysteine adsorbed on Au(643) surface at T=296 K.

and 8.12, respectively. The molecules adsorbed similarly on surfaces with different chirality. At low densities considered here, molecular rows and single molecules were encountered on the entire chiral surface, regardless of the local homochiral facet of the surface that participated in binding. The surface did not discriminate between molec-

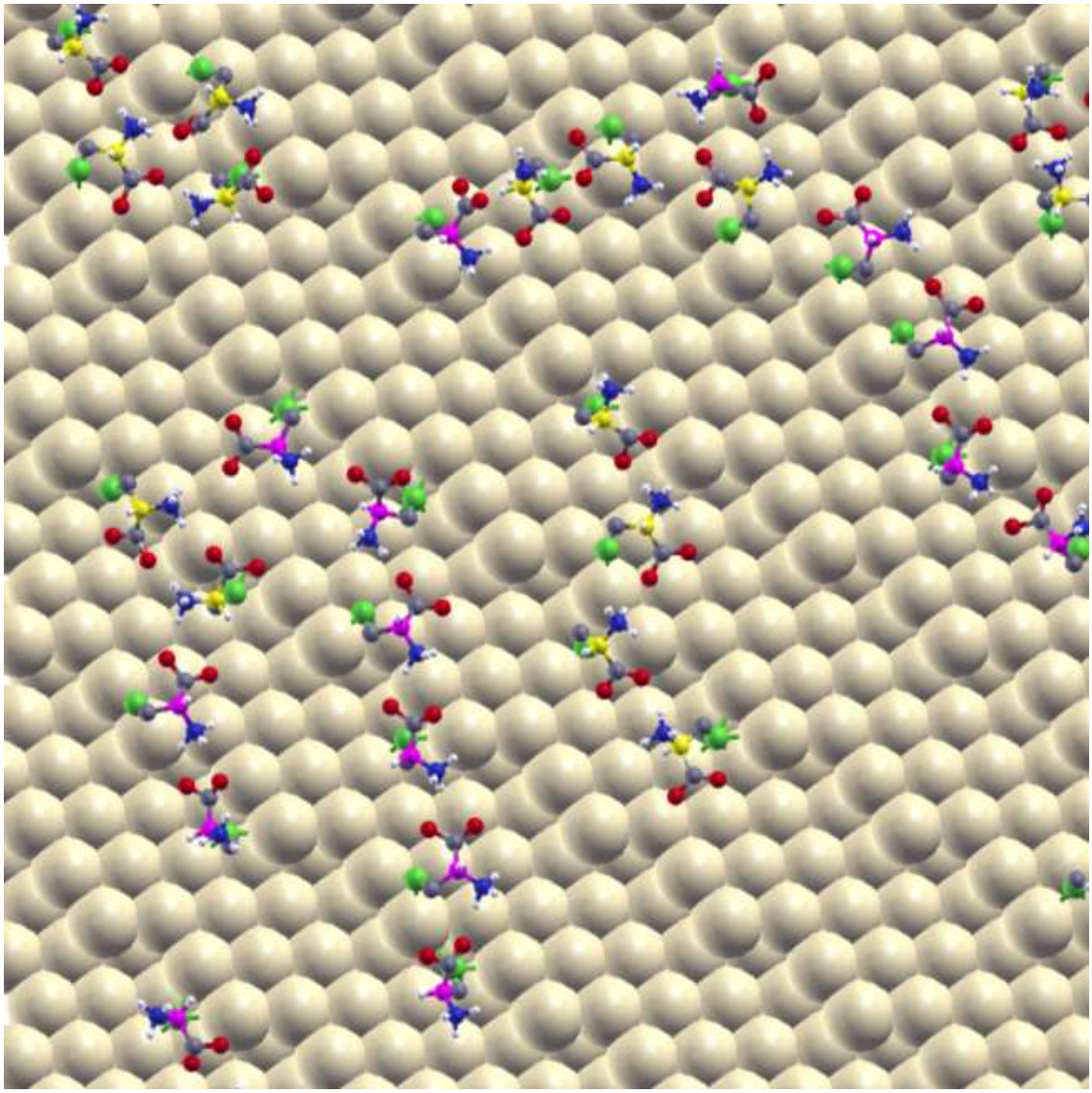

Figure 8.10: A simulation snapshot of racemic systems of zwitterionic D-cysteine adsorbed on Au(643) surface at T=277 K. Although identical, the chiral centers in the two enantiomers are colored in yellow and magenta, respectively.

ular enantiomers. The molecules, however, preferentially interacted along a molecular row with molecules of the same chirality as seen before for adsorbed racemic mixtures on simple chiral gold surfaces mentioned above (surfaces with only R chirality).

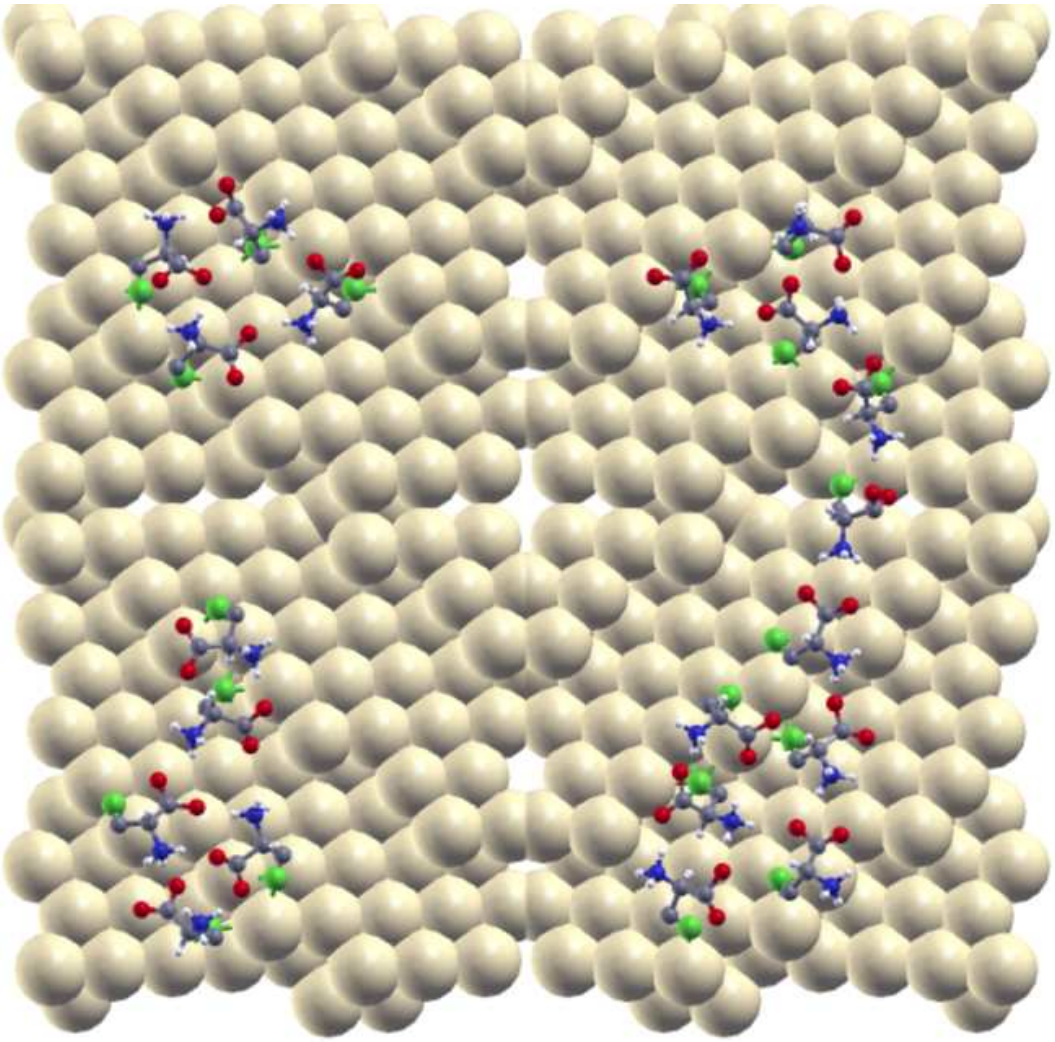

Figure 8.11: A simulation snapshot of a enantiomerically pure system of zwitterionic D-cysteine adsorbed on Au(643)$^{R\&S}$ surface at T=296 K.

Adsorption on chiral surfaces with uniform potential. The adsorption of zwitterionic cysteine onto surfaces with uniform potential was also investigated. Single molecular rows formed upon adsorption of zwitterionic molecules onto (643) surface (see Figure 8.13). Such rows were stabilized through electrostatic interaction between oppositely charged ammonium and carboxylate groups of neighbouring molecules. Zwitterionic adsorption patterns, however, did not present double row

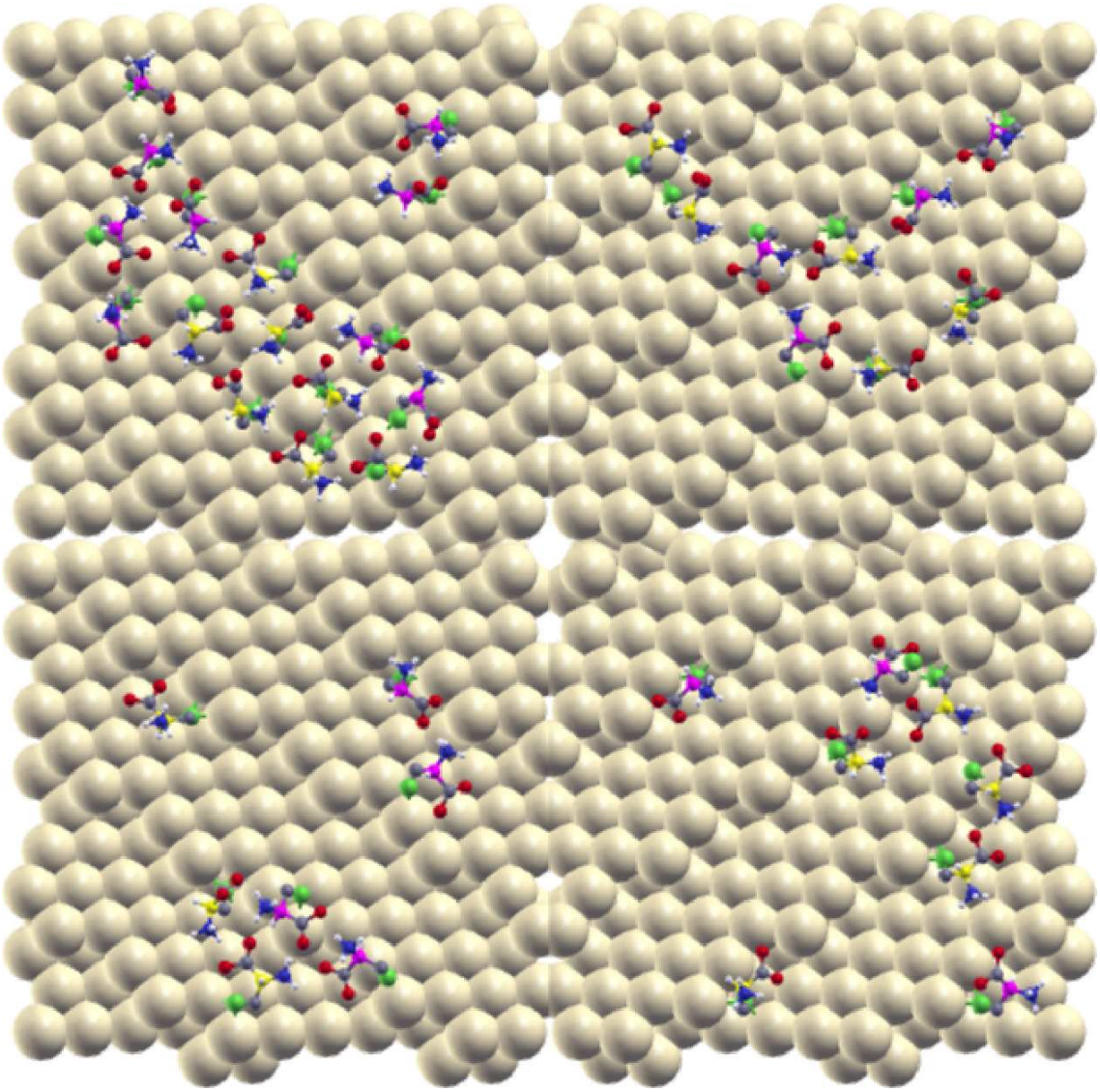

Figure 8.12: A simulation snapshot of racemic systems of zwitterionic cysteine adsorbed on Au(643)$^{R\&S}$ surface at T=296 K. Although identical, the chiral centers in the two enantiomers are colored in yellow and magenta, respectively.

conformations that were encountered on Au(111) surfaces. The molecules here interacted stronger with the stepped edges of surface and formed generally the rows along these edges. As the stepped edges were not close to each other, two molecular rows could not interact efficiently as they did on the flat surface. Cysteine molecules

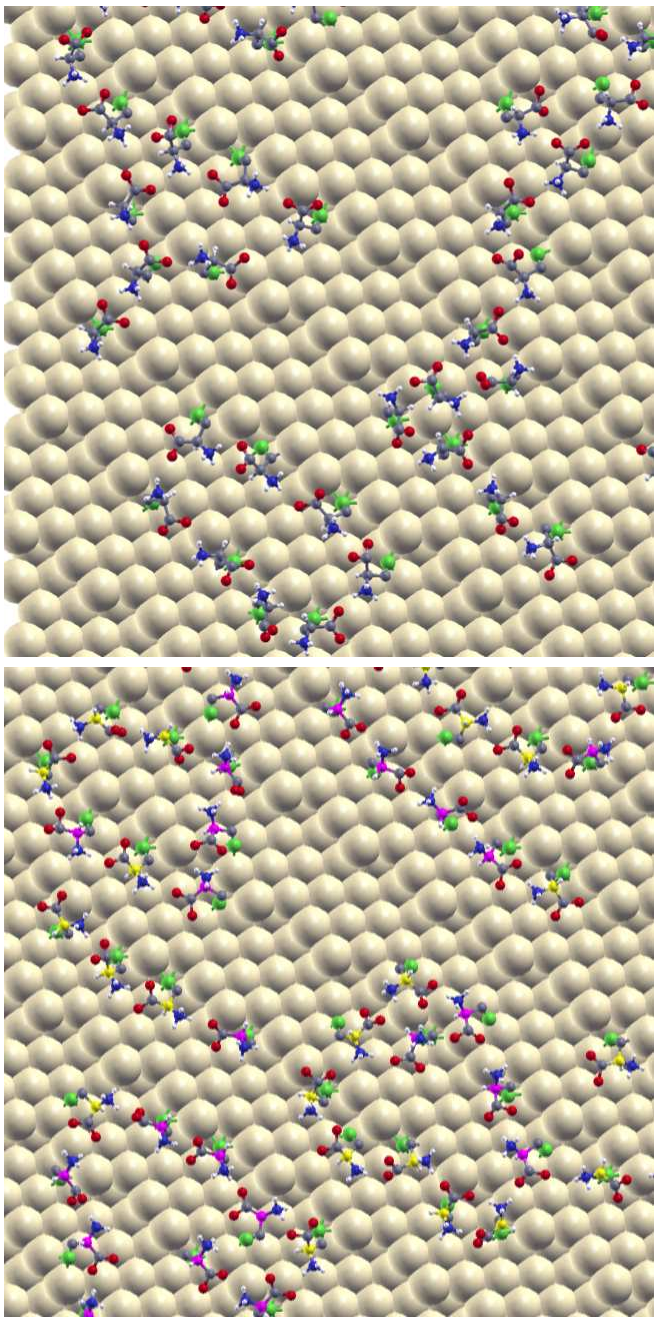

Figure 8.13: Simulation snapshots of enantiopure (a) and racemic (b) zwitterionic cysteine adsorbed onto (643) chiral surface at T=296 K. Although identical, the chiral centers in the two enantiomers are colored in yellow and magenta, respectively. The chiral surface here presents surface atoms that are of similar reactivity regardless of their coordination number.

bound strongly to the surface through sulfur atom. As a result, the binding locations of the sulfur had an impact on the final adsorption structures. On Au(111) surface molecules could relocate their thyil (thiol) group easier to the nearby hollow or bridge site if necessary. In this manner, the molecules and the molecular rows, respectively could easier get closer together and accordingly participate in stabilization of a double row configuration. On chiral (643) surface, however, the preferred adsorption sites were not evenly distributed along the surface. The thyil (thiol) group bound mostly to edge and kink sites (see Figure 8.13). As a result, the molecule adsorbed near the edges were not able to accommodate efficient interaction with both the surface and the molecules from other molecular rows. Single molecular rows that extended across the stepped edges were also encountered on (643) surface. However, such structures were in a relatively small proportion.

Adsorption of the racemic mixtures of cysteine on chiral Au(643) were also considered. Racemic mixtures of zwitterions often conserved their chirality along the molecular row (see Figures 8.13 (b)). Single molecular rows were encountered mainly along, but also across the stepped edges.

8.5 Summary

We studied the chiral behavior of zwitterionic adsorbed states. While zwitterions were unstable in gas phase or as adsorbed monomers, zwitterionic states were stabilized by surface-supported dimer formation. Not only was the second molecule necessary to form stable zwitterions, however, a second condition was also essential: that the dimer formed a strongly constrained configuration close to the surface. Like zwitterionic dimers were able to fulfill this requirement with their charged group in

optimum orientation for dimer stabilization, while unlike dimers were not: steric hindrance from the hydrogen atom on the chiral carbon lifted one of the molecules from the surface, effectively inhibiting the formation of unlike zwitterionic dimers. This combination of effects led to strong chiral discrimination in zwitterionic homocysteine and methionine, which merits further consideration. In larger systems, zwitterionic molecules self-assembled in single and double parallel row type of structures, in which the homochirality was conserved along the extended rows. Zwitterionic double rows encountered on Au(111) surface were less observed on Au(643) surfaces described by a coordination dependent potential. Double rows of zwitterionic cysteine were missing altogether on chiral surfaces with uniform potential. On the latter surfaces, the stronger surface attraction around the kinks and along the stepped edges competed with intermolecular electrostatic interaction resulting in single molecular rows that mostly extended along the edges. There were, thus, differences in the adsorption patterns dependent on the force field parameters that were used in the simulations. It is therefore important to treat chiral surfaces that expose surface atoms with distinct coordination number by using an appropriate force field that takes in account specific interactions between a non-uniform surface and the adsorbate. Our results also showed that dimer structures alone could not always forecast what structures the zwitterionic molecules would form in extended systems. For a better understanding of the mechanism for zwitterion formation on metal surfaces and the chiral self-assembly of such molecules, a larger number of molecular simulations is certainly necessary. The possible roles of residual water in this process could also be considered in further investigations.

Chapter 9

Conclusions

Chirality and chiral recognition have attracted much interest for many years. The emerging observation is that chiral recognition may be facilitated by the presence of an underlying surface. Surface assisted chiral self-assembly is a complex problem, even in cases where small organic molecules are considered. The process is determined by the interplay of an array of variables, starting with the details of the molecular make-up, the prevalent types of intermolecular interactions, as well as surface interactions and surface reorganization. Simple molecular models have the ability to break apart the complexity of this interplay of effects, and allow focused investigations of a few variables at a time.

We investigated the effects of rigid flat surfaces in chiral adsorption of several model molecules. A surface limits the configurational space available to the racemate and consequently may promote chiral separation. The formation of adsorption patterns is known to have a complicated potential energy surface. Parallel Tempering Monte Carlo is a method that was shown to work well for systems that present energy landscapes with many local minima. Our simulations are done in canonical ensem-

ble using tempering over the temperature domain. Replicas of the system evolving at low temperatures that may get trapped in a local minima, are brought out via configurational swaps with high temperature replicas.

Two of our model molecules exhibited distinct chiral self-assembly outcomes in previous surface-free, two dimensional calculations. By considering atomistic apolar rigid surfaces, we found that the adsorbed patterns and geometries were largely unaffected by surface attraction or layout. When the lattice spacing and/or atom size of the substrate were varied, however, several types of commensuration effects were observed, often leading to an enhancement of separation quality from the surface-free case.

Two main types of configurations compete in structure formation upon adsorption on flat achiral surfaces in our racemic mixture of model molecules. Chiral rosette structures of like molecules are seen to coexist with heterochiral double chains, in which molecules with opposite chirality alternate. In rosette clusters the strongly attractive tailgroups of three to ten molecules gathered together in the center of micelle, whereas the less attractive bulky headgroup was expelled toward the exterior of the micelle. This type of structures resemble rosette clusters observed experimentally for adsorption of racemates on solid surfaces.[24, 31, 163] Extended aggregates where locally homochiral structures of opposite chirality alternated within the same aggregate were also encountered. Even though the substrate impacts the chiral self-assembly, by constraining the molecules to evolve in two dimensions, intermolecular interaction decided the self-assembled arrangements in our systems. Steric interaction and electrostatic alignment dominated over the surface attraction or layout.

The stability of the chiral separation process to changes in the nature of the substrate is intriguing, given that more significant surface effects have been observed in

experiments involving chiral chemisorption processes. However, the surfaces considered in our study on chiral adsorption of model molecules are simple Lennard−Jones surfaces, suitable for the description of carbon-based or polymeric surfaces, rather than for more pervasive, highly polar metallic substrates. Nevertheless, several types of commensuration effects enhanced chiral resolution when the atom size of the substrate was varied for low-Miller index substrates.

Molecules that have previously shown polymorphic behavior, with the formation of homochiral clusters in metastable states, but not in their equilibrium configurations, were used to show how molecular substitution can be manipulated to induce chiral recognition and homochiral structure formation, in molecules that were previously unable to segregate at surface assembly. Furthermore, the analysis of pair and multibody interactions provided an avenue for in-depth understanding and even prediction of the result of the surface adsorption process.

The adsorption of amino acids at solid surfaces has attracted much interest, because on one hand, amino acids are archetypal chiral molecules and, on the other hand, they provide a first level of understanding for the behavior of biomolecules in general. We used DFT calculations to study the adsorption behavior of cysteine, homocysteine and methionine on ideal Au(111) surface. We examined the binding conditions of monomer, dimer and trimer structures, as precursors of pattern formation in extended systems. The molecules chemisorbed to the surface through thyils located at a bridge site, whereas physisorbed molecules bound through sulfur located at the top of a gold atom. The latter often accommodated the binding through nitrogen as well. Relatively stable COOH−based hydrogen bonding dimer structures were formed upon adsorption of sulfur containing amino acids, which however, became less stable when the third molecule was introduced. Chiral effects were investigated by

considering homo- and heterochiral molecular assemblies. These amino acids did not, however, exhibit intermolecular chiral discrimination upon adsorption on Au(111). Like and unlike conformations presented similar stabilization energies.

We used classical Parallel Tempering Monte Carlo methods to examine self-assembly of extended systems of enantiomerically pure and racemic cysteine, homocysteine and methionine and their binding on flat Au(111) surfaces. Our study showed that upon adsorption of sulfur containing amino acids on Au(111), whether the thiol is preserved or S−H bond is broken, the molecules formed relatively similar self-assembled structures. The assemblies, however, were strongly dependent on molecular state of the adsorbate. Neutral molecules were involved in hydrogen-bound rosette structures and single molecular rows, whereas zwitterionic molecules preferred the double row conformation. Our findings about adsorption of zwitterionic methionine on Au(111) were in good agreement with experimental observations of Naitabdi and Humblot.[36] Such findings supported our force field choice that may help us to predict the surface self-assembly in other relevant experimental systems.

Enantiomerically enriched rosette structures of four and more molecules were obtained when racemic mixtures of neutral state molecules were adsorbed on gold surface. Such clusters may be used as seeds in crystallization of supersaturated racemic solutions or as chiral seeds for separations by entrainment. A preferential orientation of molecules with the same chirality along a chain conformation was achieved via electrostatic alignment in zwitterionic racemates. Such results and the analysis of adsorbed zwitterionic dimer structures suggested significant chiral discrimination in the adsorption process of zwitterionic species on gold surfaces. However, more research is certainly required for a better understanding of the chiral recognition process in these systems.

Even though the adsorption patterns were relatively similar, stronger S−Au covalent bonds were formed between thyil groups of the investigated amino acids and the Au(111) surface. Strong chemisorption of thyils may be used in producing stable materials, whereas a weaker adsorption of methionine offers more flexibility for additional processing or tuning of the self-assembled structure.

The adsorption of cysteine was stronger on Au (643) than on Au(111), because of the presence of highly reactive low coordinated gold atoms on chiral surfaces. We developed and used a coordination dependent force field that was particularly important in describing adsorption on chiral surfaces, that exhibit surface atoms with different coordination number and reactivity. The new force field parameters were found to be quite useful, since adsorption patterns varied with the force field choice. Stable double row structure of zwitterionic cysteine molecules encountered on Au(111) and Au(643) surfaces did not form on chiral Au(643) described by an uniform potential.

Our study of adsorption on naturally chiral surfaces showed that kink sites were more likely to host the molecules and the molecular assemblies. Choosing a naturally chiral surface with a specific distribution of kinks, one may direct and control the location of the adsorbed molecules. Furthermore, the size and shape of the supramolecular adsorption structures could be modified by changing substituents in molecular structure, as well as using surfaces with distinct atomic sizes.

9.1 Future work

The effects of other chiral surfaces in chiral adsorption of enantiopure and racemic cysteine and related amino acids could make the subject of future work. Chiral surfaces with longer or shorter steps, larger or wider terraces that present a distinct concentration of surface atoms with various coordination numbers, and consequently an overall distinct surface attraction and layout, may impact the chiral self-assembly process. Furthermore, by introducing, systematically, into the surface defects such as vacancies or adatoms, or any other changes in surface reactivity one may influence and control the chiral adsorption and consequently chiral segregation. Chiral surfaces of other metals could also be considered.

The gold model surface, as well as any other model surfaces that were used in our simulations presented an ideal structure and were not affected by the presence of the adsorbate or the temperature of adsorption. Surface atoms, however, may change their position upon adsorption of different atoms and molecules and/or by experiencing changes in temperature. Thus, important features that may be taken next in consideration are the surface relaxation and reconstruction, as well as the effect of image charges. A further study about how the density affects chiral resolution in simple models or in systems of small organic molecules should also be examined.

Appendix A

Additional Information

A.0.1 Implementing molecular flexibility

Implementing molecular flexibility in Monte Carlo simulations is not an easy task. Random conformational changes have to be both reasonable for intramolecular effects and not cause overlaps with other molecules, especially in the condensed phases where molecules are generally closely packed. The MC simulation that treats flexiblity therefore must involve besides standard translational and rotational MC moves, random conformational moves.

A Fortran code that describes the random conformational changes in simulations of flexible molecules is presented in Figure A.0.1. Briefly, we designed the conformational moves as follows: The first atom of the molecule is placed randomly in the simulation box through a translational move. The second atom is then moved to a random point of a sphere with radius equal to the bond length between atom 1 and atom 2. The random point on a sphere is given by the random angle within an assigned range and the randomly chosen axis of rotation. The angle range for our simulations was [-5,5] degrees. All remaining atoms are moved in the same manner as the second atom, on

a sphere with radius equal to the bond length between the atom that is moved and the preceding atom that it is bound to. Changes in molecular structure are associated with changes in bending θ and dihedral ϕ angles. As a result, there is an energetic cost that arises from the deviations of the new structure from the equlibrium structure of the molecule. The total energy of the system in the new state includes such energetic costs along with the energy given by the intermolecular interactions. Lastly, the new configurations with the associated new total energy are accepted or rejected based on Metropolis criterion (see equation 2.1).

Bending angle between three atoms is calculated using the "cosine rule" :

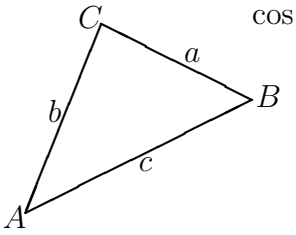

$$\cos C = \frac{a^2 + b^2 - c^2}{2ab}$$

In the triangle the angles A, B, and C are opposite to the sides a, b, and c, respectively.

Since the coordinates of each atom in the molecule are known, the distance between them can be calculated and using the formula above, the cosine of any bending angle may be found.

The torsional angle ϕ_{ijkl} is defined as the angle between ijk and jkl planes. If the equation of plane ijk is :

$$A_1 x + B_1 y + C_1 z + D_1 = 0, \tag{A.1}$$

with the determinants A_1-D_1 calculated using equation 2.10 as described in Chapter 2, and the plane jkl is described by the equation,

$$A_2x + B_2y + C_2z + D_2 = 0, \tag{A.2}$$

then the angle between the two planes is calculated as follows:

$$cos\phi = \frac{A_1A_2 + B_1B_2 + C_1C_2}{\sqrt{A_1^2 + B_1^2 + C_1^2} \cdot \sqrt{A_2^2 + B_2^2 + C_2^2}}, \tag{A.3}$$

A.0.2 Designing chiral surfaces

Naturally chiral surfaces described in Section 2.4 were designed using the Fortran subroutine shown in Figure A.2.

```
            dangle=pi/36.d0
            nangle=100
            do i=0,nangle
             gam=dble(i-(nangle/2))*dangle/dble(nangle/2)
             cosg(i)=cos(gam)
             sing(i)=sin(gam)
             ang(i)=180.0d0*gam/pi
            enddo
c     ** translation
              dxr=ran2(iseed)
              dyr=ran2(iseed)
              dzr=ran2(iseed)
              drxinew=(2.d0*dxr-1.d0)*drmax
              dryinew=(2.d0*dyr-1.d0)*drmax
              drzinew=(2.d0*dzr-1.d0)*drmax

              rxinew(1)=rxiold(1)+drxinew
              ryinew(1)=ryiold(1)+dryinew
              rzinew(1)=rziold(1)+drzinew

                do k=2,natm(ityp)
                  axr=ran2(iseed)
                  iaxis = int ( dble(nax) * axr ) + 1
                 igamma=nint(ran2(iseed)*dble(nangle))
                 cosdg=cosg(igamma)
                 sindg=sing(igamma)

                 ik=indini+k-1
                 ik1=prat(k)+indini-1
                 exiold=(x(itemp,ik)-x(itemp,ik1))
                 eyiold=(y(itemp,ik)-y(itemp,ik1))
                 eziold=(z(itemp,ik)-z(itemp,ik1))
c     ** perform rotations **
                 if ( iaxis .eq. 1 ) then
                  exinew = cosdg * exiold + sindg * eyiold
                  eyinew = cosdg * eyiold - sindg * exiold
                  ezinew = eziold
                 else if ( iaxis .eq. 2 ) then
                  exinew = cosdg * exiold - sindg * eziold
                  eyinew = eyiold
                  ezinew = cosdg * eziold + sindg * exiold
                 else
                  exinew = exiold
                  eyinew = cosdg * eyiold + sindg * eziold
                  ezinew = cosdg * eziold - sindg * eyiold
                 endif
                 rxinew(k)=rxinew(prat(k))+exinew
                 ryinew(k)=ryinew(prat(k))+eyinew
                 rzinew(k)=rzinew(prat(k))+ezinew
                enddo
_
```

Figure A.1: Fortran code that describes the random conformational changes in simulations of flexible molecules

```
      subroutine surface1(boxlx,boxly,boxlz,hboxlx,hboxly,wdt,
     1     sigma,ns,xs,ys,zs,ku,hmm,kmm,lmm,tsurf,zsmax)
      implicit real*8(a-h,o-z)
      logical tsurf,tsphere,trec
      character*3 asurf
      parameter (nmgrid=2000000,nmgrid2=10000000)

      dimension posx(nmgrid),posy(nmgrid),posz(nmgrid)
      dimension    xs(0:nmgrid2),ys(0:nmgrid2),zs(0:nmgrid2)
     1           ,xs1(nmgrid2),ys1(nmgrid2),zs1(nmgrid2)

      write(*,*) 'surface atoms diameter ', sigma
       hboxlx=boxlx/2.0
        write(ku,*) 'Miller indices', int(hmm), kmm, lmm
          if (hmm*kmm+kmm*lmm+hmm*lmm.lt.10d-6) then
              do while (hmm.lt.kmm.or.hmm.lt.lmm)
                  lmmtp=lmm
                  lmm=kmm
                  kmm=hmm
                  hmm=lmmtp
              enddo
              fcct1=2
              fcct2=1
          else
              fcct1=1
              fcct2=0
           do while (lmm.gt.hmm.or.lmm.gt.kmm)
            lmmtp=lmm
            lmm=kmm
            kmm=hmm
            hmm=lmmtp
           enddo
          endif
c  The indices have to be ordered!!!
          write(ku,*) 'ordered Miller indices', int(hmm), kmm, lmm
c  For a chiral surface h, k, l are different!
c  To obtain the mirror image of a chiral surface created here,
c  two of the Miller indices have to be switched in monte.in file
         hboxly=boxly/2.0
         hboxlz=boxlz/2.0
         zsmax=-hboxlz
         intboxlx=(hboxlx)*5*3.0d0*(hmm+kmm+lmm)/(sqrt(3.0d0)*sigma)+1
            a=sigma*(intboxlx-1)*sqrt(3.0d0)/3
         write(*,*)' a', a
             ns1=0
         write(*,*) 'intboxlx', intboxlx

         do i=1,intboxlx
             do j=1,intboxlx
             do k=1,(intboxlx/2)
            ns1=ns1+1
           xs1(ns1)=(i-1)*(2*sigma*sqrt(3.0d0)/6)
```

```
      ys1(ns1)=(j-1)*(2*sigma*sqrt(3.0d0)/6)
      zs1(ns1)=(k-1)*(2*sigma*sqrt(3.0d0)/3)
     1     +(mod(j-1,2)*2*sigma*sqrt(3.0d0)/6)
     1    +(mod(i-1,2))*2*sigma*sqrt(3.0d0)/6
     1      -(2*sigma*sqrt(3.0d0)/3)*mod(j-1,2)*mod(i-1,2)
       sumxyz=hmm*xs1(ns1)+kmm*ys1(ns1)+lmm*zs1(ns1)
      if((sumxyz-a).ge.10d-6) ns1=ns1-1
        enddo
      enddo
        enddo
  i=0
  ind=0
  iat=0
  xmax=-1000
  ymax=-1000
  zmax=-1000
  do i=1,ns1
   yrot=ys1(i)
   zrot=zs1(i)
   xrot=xs1(i)
   xs1(i)=cos(atan(hmm/kmm))*xrot-sin(atan(hmm/kmm))*yrot
   ys1(i)=cos(atan(hmm/(lmm*sin(atan(hmm/kmm)))))
     1         *cos(atan(hmm/kmm))
     1           *yrot+cos(atan(hmm/(lmm*sin(atan(hmm/kmm)))))*
     1            sin(atan(hmm/kmm))*xrot-
     1          sin(atan(hmm/(lmm*sin(atan(hmm/kmm)))))*zrot
   zs1(i)=cos(atan(hmm/(lmm*sin(atan(hmm/kmm)))))*zrot+
     1       sin(atan(hmm/(lmm*sin(atan(hmm/kmm)))))*
     1       cos(atan(hmm/kmm))*yrot+
     1        sin(atan(hmm/(lmm*sin(atan(hmm/kmm)))))*
     1        sin(atan(hmm/kmm))*xrot
    if ((ys1(i)-ymax).gt.10d-6) ymax=ys1(i)
    if ((zs1(i)-zmax).gt.10d-6) zmax=zs1(i)
    if ((xs1(i)-xmax).gt.10d-6) xmax=xs1(i)
    enddo
 zmaxz=zmax-wdt*sigma
 do i=1,ns1
   if ((zs1(i)-zmaxz).gt.10d-6)then
   if ((dabs(xs1(i))-(fcct1*a/(5*(hmm+lmm+kmm)))).le.10d-6)then
   if (((ys1(i)-(ymax-(2*a/(5*(hmm+lmm+kmm)))).ge.10d-6).and.
     1       ((ys1(i)-ymax).le.10d-6))) then
   ns=ns+1
   xs(ns)=xs1(i) +fcct2*a/(5*(hmm+lmm+kmm))
   ys(ns)=ys1(i)-ymax+(a/(5*(hmm+lmm+kmm)))
   zs(ns)=zmax-zs1(i)- hboxlz
    if ((zs(ns)-zsmax).gt.10d-6) zsmax=zs(ns)
   endif
   endif
   endif
  enddo
  return
  end
```

Figure A.2: Fortran code for creating a surface given by h, k, l Miller indices.

Bibliography

[1] Cintas, P. *Angew. Chem. Int. Ed.* **46**, 4016–4024 (2007).

[2] Rouhi, A. M. *Chem. Eng. News.* **81**, 56–61 (2003).

[3] Rouhi, A. M. *Chem. Eng. News.* **81**, 45–55 (2003).

[4] Stinson, S. C. *Chem. Eng. News.* **78**, 55–78 (2000).

[5] Smith, S. W. *Toxicol. Sci.* **110**, 4–30 (2009).

[6] Seri-Levi, A., West, A., and Richards, W. G. *J. Med. Chem.* **37**, 1727–1732 (1994).

[7] Caner, H., Groner, E., Levy, L., and Agranat, I. *DDT* **9**, 105–110 (2004).

[8] Fabro, S., Smith, R. L., and Williams, R. T. *Nature* **19**, 296 (1967).

[9] Agranat, I., Caner, H., and Caldwell, J. *Nat. Rev. Drug. Discov.* **1**, 753–768 (2002).

[10] Davies, N. M. and Teng, X. W. *Adv. Pharm.* **1**, 242–252 (2003).

[11] Friedman, M. *J. Agric. Food Chem.* **47**, 3457–3479 (1999).

[12] Maier, N. M., Franco, P., and Lindner, W. *J. Chromatogr. A* **906**, 3–33 (2001).

[13] Cancelliere, G., D'Acquarica, I., Gasparrini, F., Misiti, D., and Villani, C. *PSTT* **2**, 484–492 (1999).

[14] Wenzel, B., Fischer, S., Brust, P., and Steinbach, J. *J. Chromatogr. A* **1217**, 3855–3862 (2010).

[15] Blaschke, G. *Angew. Chem. Int. Ed. Engl.* **19**, 13–24 (1980).

[16] Hyun, M. H., Ryoo, J. J., and Pirkle, W. H. *J.Chromatogr. A* **886**, 47–53 (2000).

[17] Pirkle, W. H., Gan, K. Z., and Brice, L. J. *Tetrahedron:Asymmetry* **7**, 2814 (1996).

[18] Pirkle, W. H. and Liu, Y. *J.Chromatogr. A* **779**, 19 (1996).

[19] Tissot, O., Gouygou, M., Dallemer, F., Daran, J.-C., and Balavoine, G. G. A. *Angew. Chem. Int. Ed.* **40**, 1076 (2001).

[20] Kostyanovsky, R. G., Torbeev, V. Y., and Lyssenko, K. A. *Tetrahedron: Asymmetry* **12**, 2721 (2001).

[21] Wei, Y., Kannappan, K., Flynn, G. W., and Zimmt, M. B. *J. Am. Chem. Soc.* **126**, 5318–5322 (2004).

[22] France, C. B. and Parkinson, B. A. *J. Am. Chem. Soc.* **125**, 12712–12713 (2003).

[23] Mallat, T., Orglmeister, E., and Baiker, A. *Chem. Rev.* **107**, 4863–4890 (2007).

[24] Bohringer, M., Morgenstern, K., Schneider, W. D., and Berndt, R. *Angew. Chem. Int. Ed.* **38**, 821–823 (1999).

[25] Iski, E. V., Tierney, H. L., Jewell, A. D., and Sykes, E. C. H. *Chem. Eur. J.* **17**, 7205–7212 (2011).

[26] Xu, B., Tao, C., Cullen, W. G., Reutt-Robey, J. E., and Williams, E. D. *Nano Lett.* **5**, 2207–2211 (2005).

[27] Ernst, K.-H. *Top. Curr. Chem.* **265**, 209 –252 (2006).

[28] Barth, J. V., Constantini, G., and Kern, K. *Nature* **437**, 671–679 (2005).

[29] Barlow, S. M. and Raval, R. *Surf. Sci. Rep.* **50**, 201–341 (2003).

[30] Paci, I., Szleifer, I., and Ratner, M. A. *J. Am. Chem. Soc.* **129**, 3545–3555 (2007).

[31] Blum, M.-C., Cavar, E., Pivetta, M., Patthey, F., and Schneider, W.-D. *Angew. Chem. Int.* **44**, 5334–5337 (2005).

[32] Villagomez, C. J., Guillermet, O., Goudeau, S., Ample, F., Xu, H., Coudret, C., Bouju, X., Zambelli, T., and Gauthier, S. *J. Chem. Phys.* **132**, 074705/1–074705/8 (2010).

[33] Yuan, Q.-H., Yan, C.-J., Yan, H.-J., Wan, L.-J., Northrop, B. H., Jude, H., and Stang, P. J. *J. Am. Chem. Soc.* **130**, 8878–8879 (2008).

[34] Bombis, C., Weigelt, S., Knudsen, M. M., Norgaard, M., Busse, C., Lagsgaard, E., Besenbacher, F., Gothelf, K. V., and Linderoth, T. R. *ACS NANO* **4**, 297–311 (2010).

[35] Kuhnle, A., Linderoth, T. R., and Besenbacher, F. *J. Am. Chem. Soc.* **125**, 14680–14681 (2003).

[36] Naitabdi, A. and Humblot, V. *Appl. Phys. Lett.* **97**, 223112/1–223112/3 (2010).

[37] Barlow, S. M. and Raval, R. *Curr. Opin. Colloid Interface Sci.* **13**, 65–73 (2008).

[38] Kuhnle, A., Linderoth, T. R., Hammer, B., and Besenbacher, F. *Nature* **415**, 891–893 (2002).

[39] Fang, H., Giancarlo, L. C., and Flynn, G. W. *J. Phys. Chem* **102**, 7311–7315 (1998).

[40] Yablon, D. G., Wintgens, D., and Flynn, G. W. *J. Phys. Chem. B* **106**, 5470–5475 (2002).

[41] Morf, P., Ballav, N., Putero, M., von Wrochem, F., Wessels, J. M., and Jung, T. A. *J. Phys. Chem. Lett.* **1**, 813–816 (2010).

[42] Laliberte, M.-A., Lavoie, S., Hammer, B., Mahieu, G., and McBreen, P. H. *J. Am. Chem. Soc.* **130**, 5386–5387 (2008).

[43] Kuhnle, A. *Curr. Opin. Colloid Interface Sci.* **14**, 157–168 (2009).

[44] Gellman, A. J. *ACS NANO* **4**, 5–10 (2010).

[45] Raval, R. *J. Mol. Catal. A* **305**, 112–116 (2009).

[46] James, J. N. and Sholl, D. S. *Curr. Opin. Colloid Interface Sci.* **13**, 60–64 (2008).

[47] Sholl, D. S. and Gellman, A. J. *AlChE J.* **55**, 2484–2490 (2009).

[48] Szabelski, P. *J. Comput. Chem.* **29**, 1615–1625 (2008).

[49] Shukla, N., Bartel, M. A., and Gellman, A. J. *J. Am. Chem. Soc.* **132**, 8575–8580 (2010).

[50] Raval, R. *Chem. Soc. Rev.* **38**, 707–721 (2009).

[51] Jonkheijm, P., Miura, A., Zdanowska, M., Hoeben, F. J. M., De Feyter, S., Schenning, A. P. H. J., De Schryver, F. C., and Meijer, E. W. *Angew. Chem. Int. Ed.* **43**, 74–78 (2004).

[52] Gutzler, R., Cardenas, L., and Rosei, F. *Chem. Sci.* **2**, 2290–2300 (2011).

[53] Szabelski, P. and Woszczyk, A. *Langmuir* **28**, 11095–11105 (2012).

[54] Stevens, F., Dyer, D. J., and Walba, D. M. *Angew. Chem. Int. Ed. Engl.* **35**, 900–901 (1996).

[55] Humblot, V., Haq, S., Muryn, C., Hofer, W. A., and Raval, R. *J. Am. Chem. Soc.* **124**, 7991–8000 (2002).

[56] Ernst, K.-H. *Orig. Life Evol. Biosph.* **40**, 41–50 (2010).

[57] Pivetta, M., Blum, M.-C., Patthey, F., and Schneider, W.-D. *J. Phys. Chem. B* **113**, 4578–4581 (2009).

[58] Schiffrin, A., Reichert, J., Pennec, Y., Auwarter, W., Weber-Bargioni, A., Marschall, M., Dell'Angela, M., Cvetko, D., Bavdek, G., Cossaro, A., Morgante, A., and Barth, J. V. *J. Phys. Chem. C* **113**, 12101–12108 (2009).

[59] Elemans, A. A. W., Lei, S., and De Feyter, S. *Angew. Chem. Int. Ed.* **48**, 7298–7332 (2009).

[60] Wang, L., Kong, H., Song, X., Liub, X., and Wanga, H. *Phys. Chem. Chem. Phys.* **12**, 14682–14685 (2010).

[61] Kruchten, F., Knorr, K., Volkmann, U. G., Taub, H., Hansen, F. Y., Matthies, B., and Herwig, K. W. *Langmuir* **21**, 7507–7512 (2005).

[62] Pivetta, M., Blum, M.-C., Patthey, F., and Schneider, W.-D. *Angew. Chem. Int. Ed* **47**, 1076–1079 (2008).

[63] Lehn, J.-M. *Angew. Chem. Int. Ed.* **52**, 2836–2850 (2013).

[64] Palma, C.-A., Cecchini, M., and Samori, P. *Chem. Soc. Rev.* **41**, 3713–3730 (2012).

[65] Zerbetto, F. *Adv. Mat.* **25**, 449–455 (2013).

[66] Gronbeck, H., Curioni, A., and Andreoni, W. *J. Am. Chem. Soc.* **122**, 3839–3842 (2000).

[67] Askerka, M., Pichugina, D., Kuz'menko, N., and Shestakov, A. *J. Phys. Chem. A* **116**, 7686–7693 (2012).

[68] Kuhnle, A., Linderoth, T. R., Schunack, M., and Besenbacher, F. *Langmuir* **22**, 2156–2160 (2006).

[69] Felice, R. D. and Selloni, A. *J. Chem. Phys* **120**, 4906–4914 (2004).

[70] Greber, T., Sljivancanin, Z., Schilinger, R., Wider, J., and Hammer, B. *Phys. Rev. Lett.* **96**, 056103/1–056103/4 (2006).

[71] Kuhnle, A., Linderoth, T. R., and Besenbacher, F. *Top. Catal.* **54**, 1384–1391 (2011).

[72] Kuhnle, A., Linderoth, T. R., and Besenbacher, F. *J. Am. Chem. Soc.* **128**, 1076–1077 (2006).

[73] Carr, J. A., Wang, H., Abraham, A., Gullion, T., and Lewis, J. P. *J. Phys. Chem. C* **116**, 25816–25823 (2012).

[74] Abraham, A., Ilott, A. J., Miller, J., and Gullion, T. *J. Phys. Chem. B* **116**, 7771–7775 (2012).

[75] Thomsen, L., Wharmby, M. T., Riley, D. P., Held, G., and Gladys, M. J. *Surf. Sci.* **603**, 1253–1261 (2009).

[76] Zhang, J., Demetriou, A., Welinder, A. C., Albrecht, T., Nichols, R. J., and Ulstrup, J. *Chem. Phys.* **319**, 210–221 (2005).

[77] Felice, R. D., Selloni, A., and Molinari, E. *J. Phys. Chem. B* **107**, 1151–1156 (2003).

[78] Zhao, Y., Zhou, F., Zhou, H., and Su, H. *Phys. Chem. Chem. Phys.* **15**, 1690–1698 (2013).

[79] Mateo-Marti, E., Rogero, C., Gonzalez, C., Sobrado, J. M., Andres, P. L. D., and Martin-Grego, J. A. *Langmuir* **26**, 4113–4118 (2010).

[80] Fajin, J. L. C., Gomes, J. R. B., and Cordeiro, M. N. D. S. *Langmuir* **29**, 8856–8864 (2013).

[81] Buimaga-Iarinca, L. and Calborean, A. *Phys. Scr.* **86**, 035707/1–035707/6 (2012).

[82] Verde, A. V., Acres, J. M., and Maranas, J. K. *Biomacromolecules* **10**, 2118–2128 (2009).

[83] Wright, L. B., Rodger, P. M., Corni, S., and Walsh, T. R. *J. Chem. Theory Comput.* **9**, 1616–1630 (2013).

[84] Corni, S., Hnilova, M., Tamerler, C., and Sarikaya, M. *J. Phys. Chem. C* **117**, 16990–17003 (2013).

[85] Hazen, R. M. and Sholl, D. S. *Nat. Mater.* **2**, 367–374 (2003).

[86] Held, G. and Gladys, M. *Top. Catal.* **48**, 128–136 (2008).

[87] Baker, L., Holsclaw, B., Baber, A. E., Tierney, H. L., Sykes, E. C. H., and Gellman, A. J. *J. Phys. Chem. C* **114**, 18566–18575 (2010).

[88] Gellman, A. J., Horvath, J. D., and Buelow, M. T. *J. Mol. Catal. A* **167**, 6–11 (2001).

[89] Attard, G. A. *J. Phys. Chem. B* **105**, 3158–3167 (2001).

[90] Horvath, J. D. and Gellman, A. *J. Am. Chem. Soc.* **124**, 2384–2392 (2002).

[91] Horvath, J. D. and Gellman, A. *Top. Catal.* **25**, 9–15 (2003).

[92] Asthagiri, A., Feibelman, P. J., and Sholl, D. *Top. Catal.* **18**, 193–200 (2002).

[93] Baber, A. E., Gellman, A. J., Sholl, D. S., and Sykes, E. C. H. *J. Phys. Chem. C* **112**, 11086–11089 (2008).

[94] Sholl, D., Asthagiri, A., and Power, T. D. *J. Phys. Chem. B.* **105**, 4771–4782 (2001).

[95] Power, T. D., Asthagiri, A., and Sholl, D. *Langmuir* **18**, 3737–3748 (2002).

[96] Zhao, X. *J. Am. Chem. Soc* **122**, 12584–12585 (2000).

[97] Horvath, J. D., Koritnik, A., Kamakoti, P., Sholl, D., and Gellman, A. *J. Am. Chem. Soc.* **126**, 14988–14994 (2004).

[98] Ahmadi, A., Attard, G., Feliu, J., and Rodes, A. *Langmuir* **15**, 2420–2424 (1999).

[99] Sljivancanin, Z., Gothelf, K. V., and Hammer, B. *J. Am. Chem. Soc.* **124**, 14789–14794 (2002).

[100] Huang, Y. and Gellman, A. *Top. Catal.* **54**, 1403–1413 (2011).

[101] Rampulla, D. M., Francis, A. J., Knight, K. S., and Gellman, A. J. *J. Phys. Chem. B.* **110**, 10411–10420 (2006).

[102] Gladys, M. J., Stevens, A. V., Scott, N. R., Jones, G., Batchelor, D., and Held, G. *J. Phys. Chem. C* **111**, 8331–8336 (2007).

[103] Horvath, J. D. and Gellman, A. *J. Am. Chem. Soc.* **123**, 7953–7954 (2001).

[104] Huang, Y. and Gellman, A. *Catal. Lett.* **125**, 177–182 (2008).

[105] Bhatia, B. and Sholl, D. S. *Angew. Chem. Int. Ed.* **44**, 7761–7764 (2005).

[106] Sholl, D. S. *Langmuir* **14**, 862–867 (1998).

[107] McFadden, C., Cremer, P. S., and Gellman, A. J. *Langmuir* **12**, 2483–2487 (1996).

[108] Pascal, T. A., Karasawa, N., and III, W. A. G. *J. Chem. Phys.* **133**, 134114/1–134114/17 (2010).

[109] Jorgensen, W. L., Maxwell, D. S., and Tirado-Rives, J. *J. Am. Chem. Soc.* **118**, 11225–11236 (1996).

[110] Weiner, S. J., Kollman, P. A., Case, D. A., Singh, U. C., Ghio, C., Alagona, G., Profeta, S., and Weiner, P. *J. Am. Chem. Soc.* **106**, 765–784 (1984).

[111] Shinoda, W., Devane, R., and Klein, M. L. *Molecular Simulation* **15**, 27–36 (2007).

[112] Devane, R., Shinoda, W., Moore, P. B., and Klein, M. L. *J. Chem. Theory Comput.* **5**, 2115–2124 (2009).

[113] Devane, R., Klein, M. L., Chiu, C.-C., Nielsen, S. O., Shinoda, W., and Moore, P. B. *J. Phys. Chem.* **114**, 6386–6393 (2010).

[114] Iori, F., Felice, R. D., Molinari, E., and Corni, S. *J. Comput. Chem.* **30**, 1465–1476 (2009).

[115] Duan, Y., Wu, C., Chowdhury, S., Lee, M. C., Xiong, G., Zhang, W., Yang, R., Cieplak, P., Luo, R., Lee, T., Calwell, J., Wang, J., and Kollman, P. *J. Comput. Chem.* **24**, 1999–2012 (2003).

[116] Jorgensen, W. L. and Tirado-Rives, J. *PNAS* **102**, 6665–6670 (2005).

[117] Swendsen, R. H. and Wang, J. S. *Phys. Rev. Lett.* **57**, 2607–2609 (1986).

[118] Marinari, E. and Parisi, G. *Europhys. Lett.* **19**, 451–458 (1992).

[119] Earl, D. J. and Deem, M. W. *Phys. Chem. Chem. Phys.* **7**, 3910–3916 (2005).

[120] Geyer, C. J. and Thompson, E. A. *J. Am. Statist. Assoc.* **90**, 909–920 (1995).

[121] Katzgraber, H. G., Trebst, S., Huse, D. A., and Troyer, M. *J. Stat. Mech.* **P03018**, 1–22 (2006).

[122] Frenkel, D. and Smit, B. *Understanding Molecular Simulation from Algorithms to Applications.* Academic Press, San Diego, California, (2002).

[123] Hukushima, K. and Nemoto, K. *J. Phys. Soc. Jpn.* **65**, 1604–1608 (1996).

[124] Lyubartsev, A. P., Martinovski, A. A., Shevkunov, S. V., and Vorontsov-Velyaminov, P. N. *J. Chem. Phys.* **96**, 1776–1783 (1992).

[125] Hansmann, U. H. E. *Chem. Phys. Lett.* **281**, 140–150 (1997).

[126] Neirotti, J. P., Calvo, F., Freeman, D. L., and Doll, J. D. *J. Chem. Phys.* **112**, 10340–10349 (2000).

[127] Calvo, F., Neirotti, J. P., Freeman, D. L., and Doll, J. D. *J. Chem. Phys.* **112**, 10350–10357 (2000).

[128] Falcioni, M. and Deem, M. W. *J. Chem. Phys.* **110**, 1754–1765 (1999).

[129] Metropolis, N. and Ulam, S. *J. Am. Statist. Assoc.* **44**, 335–341 (1949).

[130] Metropolis, N., Rosenbluth, A. W., Rosenbluth, M. N., and Teller, A. H. *J. Chem Phys.* **21**, 1087–1092 (1953).

[131] Kofke, D. A. *J. Chem. Phys.* **117**, 6911–6914 (2002).

[132] Kone, A. and Kofke, D. A. *J. Chem. Phys.* **122**, 206101/1–206101/2 (2005).

[133] Predescu, C., Predescu, M., and Ciobanu, C. V. *J. Chem. Phys.* **120**, 4119–4128 (2004).

[134] Predescu, C., Predescu, M., and Ciobanu, C. V. *J. Phys. Chem. B* **109**, 4189–4196 (2005).

[135] Rathore, N., Chopra, M., and de Pablo, J. J. *J. Chem. Phys.* **122**, 024111/1–024111/8 (2005).

[136] Jorgensen, W. L. and Tirado-Rives, J. *J. Am. Chem. Soc.* **110**(6), 1657–1666 (1988).

[137] Frisch, M. J., Trucks, G. W., Schlegel, H. B., Scuseria, G. E., Robb, M. A., Cheeseman, J. R., Scalmani, G., Barone, V., Mennucci, B., Petersson, G. A., Nakatsuji, H., Caricato, M., Li, X., Hratchian, H. P., Izmaylov, A. F., Bloino, J., Zheng, G., Sonnenberg, J. L., Hada, M., Ehara, M., Toyota, K., Fukuda, R., Hasegawa, J., Ishida, M., Nakajima, T., Honda, Y., Kitao, O., Nakai, H., Vreven, T., Montgomery, Jr., J. A., Peralta, J. E., Ogliaro, F., Bearpark, M., Heyd, J. J., Brothers, E., Kudin, K. N., Staroverov, V. N., Kobayashi, R., Normand, J., Raghavachari, K., Rendell, A., Burant, J. C., Iyengar, S. S., Tomasi, J., Cossi, M., Rega, N., Millam, J. M., Klene, M., Knox, J. E., Cross, J. B., Bakken, V., Adamo, C., Jaramillo, J., Gomperts, R., Stratmann, R. E., Yazyev, O., Austin, A. J., Cammi, R., Pomelli, C., Ochterski, J. W., Martin, R. L., Morokuma, K., Zakrzewski, V. G., Voth, G. A., Salvador, P., Dannenberg, J. J., Dapprich, S., Daniels, A. D., Farkas, ., Foresman, J. B., Ortiz, J. V., Cioslowski, J., and Fox, D. J. Gaussian Inc. Wallingford CT 2009.

[138] Breneman, C. M. and Wiberg, K. B. *J. Comp. Chem.* **11**, 361–373 (1990).

[139] Chapman, C., Ting, E., Kereszti, A., and Paci, I. *XXX* **xx**, xxx (2013).

[140] Paci, I., Szleifer, I., and Ratner, M. A. *J. Phys. Chem. B* **109**, 12935–12945 (2005).

[141] Ulman, A. *Chem. Rev.* **96**, 1533–1554 (1996).

[142] De Feyter, S. and De Schryver, F. C. *Chem. Soc. Rev.* **32**, 139–150 (2003).

[143] Paci, I., Szleifer, I., and Ratner, M. A. *Chim. Oggi.* **25**, 18–22 (2007).

[144] Popa, T. and Paci, I. *Soft Matter* **9**, 7988–7998 (2013).

[145] Paci, I. and Cann, N. M. *J. Chem. Phys.* **115**, 8489–8505 (2001).

[146] Popa, T. and Paci, I. *Chem. Phys. Lett.* **507**, 128–133 (2011).

[147] Paci, I. *J. Phys. Chem. C* **114**, 19425–19432 (2010).

[148] Calzolari, A. and Felice, R. D. *J. Phys.:Condens. Mat* **52**, 305018/1–305018/11 (2007).

[149] Nazmutdinov, R. R., Zhang, J., Zinkicheva, T. T., Manyurov, I. R., and Ulstrup, J. *Langmuir* **22**, 7556–7567 (2006).

[150] Hoffling, B., Ortmann, F., Hannewald, K., and Bechstedt, F. *Phys. Rev. B* **81**, 045407/1–045407/12 (2010).

[151] Buimaga-Iarinca, L. and Morari, C. *RSC. Adv.* **3**, 5036–5044 (2013).

[152] Zhang, J., Chi, Q., Nazmutdinov, R. R., Zinkicheva, T. T., and Bronshtein, M. D. *Langmuir* **25**, 2232–2240 (2009).

[153] Sanchez-Portal, D., Ordejon, P., Artacho, E., and Soler, J. M. *Int. J. Quantum. Chem.* **65**, 453–461 (1997).

[154] Soler, J. M., Artacho, E., Gale, J. D., Carcia, A., Junquera, J., Ordejon, P., and Sanchez-Portal, D. *J. Phys.: Condens Matter* **14**, 2745–2779 (2002).

[155] Perdew, J. P., Burke, K., and Ernzerhof, M. *Phys. Rev. Lett.* **77**, 3865–3868 (1996).

[156] Troullier, N. and Martins, J. L. *Phys. Rev. B* **43**, 1993–2006 (1991).

[157] Renzi, V. D., Lavagnino, L., Corrandini, V., Biagi, R., and Canepa, M. *J. Phys. Chem. C* **112**, 14439–14445 (2008).

[158] Popa, T., Ting, E. C. M., and Paci, I. , submitted (2013).

[159] Caprile, L., Cossaro, A., Falleta, E., Pina, C. D., Cavalleri, O., Rolandi, R., Terreni, S., Ferrando, R., Rossi, M., Floreano, L., and Canepa, M. *Nanoscale* **4**, 7727–7734 (2012).

[160] Gonella, G., Terreni, S., Cvetko, D., Cossaro, A., Mattera, L., Cavalleri, O., Rolandi, R., Morgante, A., Floreano, L., and Canepa, M. *J. Phys. Chem. B* **109**, 18003–18009 (2005).

[161] Zhang, H.-M., Su, G.-J., Wang, D., Wan, L.-J., Jin, G., Bai, C.-L., and Zhou, X. *Electrochim. Acta* **49**, 1629–1633 (2004).

[162] Schiffrin, A., Riemann, A., Auwarter, W., Pennec, Y., Weber-Bargioni, A., Cvetko, D., Cossaro, A., Morgante, A., and Barth, J. V. *Proc. Natl. Acad. Sci. USA* **104**, 5279–5284 (2007).

[163] Spillman, H., Dmitriev, A., Lin, N., Messina, P., Barth, J. V., and Kern, K. *J. Am. Chem. Soc.* **125**, 10725–10728 (2003).